

Microstructural Evolution in Medium Manganese Steels during Quenching and High-Temperature Partitioning Process

A combined experimental and modelling approach

Ayenampudi, S.

DOI

[10.4233/uuid:917ba84e-a013-4141-a9e4-71494b2c48e8](https://doi.org/10.4233/uuid:917ba84e-a013-4141-a9e4-71494b2c48e8)

Publication date

2021

Document Version

Final published version

Citation (APA)

Ayenampudi, S. (2021). *Microstructural Evolution in Medium Manganese Steels during Quenching and High-Temperature Partitioning Process: A combined experimental and modelling approach*. [Dissertation (TU Delft), Delft University of Technology]. <https://doi.org/10.4233/uuid:917ba84e-a013-4141-a9e4-71494b2c48e8>

Important note

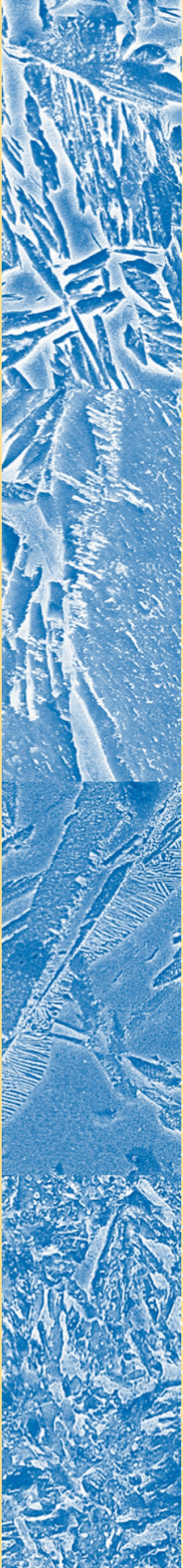
To cite this publication, please use the final published version (if applicable). Please check the document version above.

Copyright

Other than for strictly personal use, it is not permitted to download, forward or distribute the text or part of it, without the consent of the author(s) and/or copyright holder(s), unless the work is under an open content license such as Creative Commons.

Takedown policy

Please contact us and provide details if you believe this document breaches copyrights. We will remove access to the work immediately and investigate your claim.

A vertical strip on the left side of the cover features three distinct microstructural images of steel. The top image shows a complex, interconnected network of light and dark regions, likely representing a bainitic or martensitic structure. The middle image shows a more regular, layered structure with alternating light and dark bands, possibly indicating a lamellar structure. The bottom image shows a dense, fine-grained structure with a high density of small, dark features, likely representing a fine-grained martensite or bainite.

Microstructural Evolution in Medium Manganese Steels during Quenching and High-Temperature Partitioning Process

A combined experimental and modelling approach

Sudhindra Ayenampudi

Microstructural Evolution in Medium Manganese Steels during Quenching and High-Temperature Partitioning Process

A combined experimental and modelling approach

Sudhindra AYENAMPUDI

Microstructural Evolution in Medium Manganese Steels during Quenching and High-Temperature Partitioning Process

A combined experimental and modelling approach

Dissertation

for the purpose of obtaining the degree of doctor
at Delft University of Technology
by the authority of the Rector Magnificus Prof.dr.ir. T.H.J.J. van der Hagen,
chair of the Board for Doctorates,
to be defended publicly on
Wednesday 15 September at 12:30 hours

by

Sudhindra AYENAMPUDI

Master of Science in Metallurgical Engineering, RWTH Aachen University, Germany
born in Visakhapatnam, India.

This dissertation has been approved by the promoters.

Composition of the doctoral committee:

Rector Magnificus,
Prof.dr. M.J. Santofimia Navarro
Prof.dr.ir. J. Sietsma

Chairperson
Delft University of Technology, promoter
Delft University of Technology, promoter

Independent members:

Dr. A. Arlazarov
Dr. M.X. Huang
Prof.dr. H. Goldenstein
Prof.dr.ir. L.A.I. Kestens

ArcelorMittal Global R&D, France
University of Hong Kong, Hong Kong
PSU San Paulo, Brazil
Delft University of Technology

Other members:

Dr. C. Alonso de Celada Casero

TATA Steel Europe, The Netherlands

Reserve member:

Prof.dr. J. Dik

Delft University of Technology

The research described in this dissertation was carried out in the Department of Materials Science and Engineering at Delft University of Technology, The Netherlands.

This research was carried out with the financial support of the Research Fund for Coal and Steel (RFCS) through the RFCS Grant, proposal number 709855.



Printed by: ProefschriftMaken || www.proefschriftmaken.nl

Cover by: Sudhindra Ayenampudi

Copyright © 2021 by Sudhindra AYENAMPUDI

ISBN 978-94-6423-427-5

An electronic version of this dissertation is available at TUDelft repository.

Contents

1	Introduction	1
	1.1. Introduction and Research Objective	2
	1.2. Research Outline	7
	References	8
2	Microstructure Evolution during Quenching and High-Temperature Partitioning processing of a Medium-Mn Steel.....	11
	2.1. Introduction	12
	2.2. Material and Experimental Methods	13
	2.3. Design of Heat Treatments.....	14
	2.4. Results	16
	2.5. Discussion	22
	2.5.1. Carbon Balance at Different Partitioning Temperatures	22
	2.5.2. Length Changes Associated to the Reactions occurring during the Partitioning Stage.....	25
	2.5.3. Analysis of Simultaneous Phenomena occurring during High-Temperature Partitioning Stages.....	28
	2.6. Conclusions	31
	References	32
3	Impact of Si and Ni on Quenching and High-Temperature Partitioning processing in medium-Mn steels.....	35
	3.1. Introduction	36
	3.2. Materials and Experimental Methods.....	37
	3.3. Design of Heat Treatments.....	38
	3.4. Results	40
	3.5. Discussion	47
	3.5.1. Assessment of Carbon Partitioning	47
	3.5.2. Interplay of Alloying Elements at Different Partitioning Temperatures	50
	3.6. Conclusions	55
	References	56
4	3D Atom Probe Tomography and Phase-Field Modelling Investigation of Interface Migration and Elemental Partitioning during Quenching and High-Temperature Partitioning Process	59
	4.1. Introduction	60
	4.2. Experimental Methods	61
	4.2.1. Material and Microstructure Development.....	61
	4.2.2. 3D Atom Probe Tomography	62

4.3. Model	62
4.3.1. Description of Phase-Field Model	62
4.3.2. Simulation Conditions and Microstructure Development	63
4.4. Results	65
4.4.1. 3D Atom Probe Tomography (APT) measurement	65
4.4.2. 2D Phase-Field Simulations	67
4.4.3. 1D Phase-Field Simulations	73
4.5. Discussion	74
4.5.1. Austenite Reversion and Manganese Partitioning at 600 °C	75
4.5.2. Microstructural Mechanisms to Stabilise Austenite in a Wide Range of Partitioning Temperatures	79
4.5.3. Impact of Grain Size on Carbon Partitioning	80
4.6. Conclusions	81
References	82
5 In-situ Magnetometry and Dilatometry Investigation of Austenite Evolution during Quenching and High-Temperature Partitioning Process in a Medium-Mn Steel	87
5.1. Introduction	88
5.2. Material, Heat Treatments and Experimental Methods	89
5.2.1. Magnetic Measurements	90
5.2.2. Dilatometry	92
5.2.3. Microstructural Characterisation	93
5.3. Results	93
5.3.1. Phase Transformation Temperatures	93
5.3.2. Quenching and Partitioning (Q&P) Heat Treatments	96
5.4. Discussion	100
5.5. Conclusions	105
References	106
6 Key Conclusions and Recommendations	111
6.1. Key Conclusions	112
6.2. Recommendations for Future Work	113
Summary	115
Samenvatting	119
Acknowledgements	123
List of Publications	125
List of Conferences	127
About the Author	129

1

Introduction

1.1. Introduction and Research Objective

Since the very beginning, humans have been smart in identifying and using the resources available around them. One such discovery is ‘metals’ and dominant usage of such metals in respective time periods divided mankind’s history into different ages, namely: the Copper Age (3500 to 2300 B.C.), the Bronze Age (3000 – 1200 B.C), and the Iron Age (1200 – 550 B.C). Around 400 B.C., a smelting technique was invented by Indian metal-makers that happened to bond carbon with iron. This led to the production of first ever steel known as Wootz steel. It was only in the late 19th and the 20th century (termed as ‘Age of Steel’) that a huge progress in steelmaking took place to make steel economical and viable for various applications. Also, it was during this period that technological advances in the scientific field led to the development of microscopes (optical microscopes to electron microscopes) which have been helpful for detailed investigation of steel microstructures at different scales.

Over the past few decades steel is considered as a primary choice for various applications starting from household items to space ships. This is not only because of its relatively low production and recycling costs but also because of the wide range of properties that it can offer. These extensive properties attained by the family of steels are mainly achieved by design of microstructures through addition of alloying elements and design of metallurgical processing/thermal routes. Over the past decades the major challenge has been to produce steel grades that have a combination of two largely antagonistic properties, high mechanical strength and high ductility, in an economical way. Figure 1.1 illustrates the ultimate tensile strength (UTS) and total elongation offered by different steel grades based on the data adopted from the worldautosteel group of world steel association [1]. Depending on the strength and ductility they offer, the steel grades are classified into: a) Conventional steels, b) 1st generation, c) 2nd generation, and d) 3rd generation of advanced high strength steels (AHSS) [2-4].

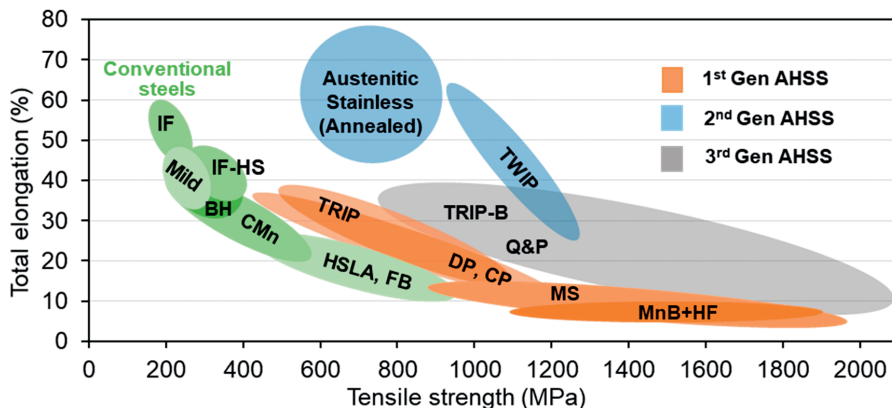


Figure 1.1. Schematic overview of the evolution of advanced high strength steels (AHSS). Data adopted from worldautosteel group of world steel association [1].

Looking into the recent history of steel, prior to the 1980’s all steel grades were either very ductile or strong. These steel grades are termed as conventional steels, Figure 1.1. These steels consist of only a

single phase called ferrite, which is a phase of iron with a body-centred cubic (bcc) structure at room temperature containing a very low concentration of carbon in interstitial solid solution. Although ferrite is a soft phase, addition of alloying elements can alter the final properties of the steel grade. Conventional steel grades such as interstitial free steels (IF) and ultra-low carbon steels (ULC) were developed for applications that require a highly ductile material, while high-strength low-alloy steels (HSLA) and carbon-manganese steels (CM) have higher strength (300-800 MPa) with a compromise in ductility. The use of conventional steel grades to make the body of automobiles served the basic purpose, but the passenger safety and fuel consumption have been put to test. With the increase in new and more demanding requirements, the steelmakers were challenged to produce steels with differently balanced strength and ductility.

Hence, the 1st generation AHSS grades were proposed, as an extension of conventional steels, that can offer both higher strength with only limited reduction in ductility. Introduction of 1st generation AHSS grades in automotive sector, under the ULSAB program, led to a reduction in vehicle weight and production costs of a four-door sedan by 25 % and 10 %, respectively [5]. 1st generation AHSS grades were developed by taking advantage of phase transformations in carbon steels and among them dual-phase steels were the first family of high strength automotive steels. Dual-phase steels majorly consist of ferrite matrix in combination with a stronger phase, martensite, which is formed from quenching of austenite (γ), a face-centred cubic (fcc) structure that is stable at 910 °C for pure iron, to room temperature [6]. Although dual-phase steels can have tensile strengths up to 800 MPa - 1200 MPa, the ductility is simultaneously compromised. In the view of further progress, TRIP (Transformation Induced Plasticity) steels were developed with bainite (a mixture of ferrite and finely dispersed cementite) and retained austenite (soft phase compared to martensite) as additional phases along with the phases in dual-phase steels. The retained austenite present in the TRIP steel microstructure is advantageous in increasing the total elongation of the material, as the retained austenite progressively transforms into martensite with increasing strain. This is called TRIP effect. However, the presence of retained austenite reduces the total strength of the steel relative to dual-phase steels as the fraction of strong phase is less in TRIP steels. Other 1st generation steels such as complex-phase steels (CP) and martensitic steels (MART) offer a strength up to 1800 MPa but this is usually accompanied with a strong decrease in ductility. Based on the application, addition of further alloying elements and/or variation in the thermal processing alters the properties of these 1st generation steels. As shown in Figure 1.1, the positioning of conventional steels and 1st generation AHSS grades based on the range of strength and ductility leads to a 'banana-shaped curve'.

The 2nd generation AHSS grades came into existence for automobile weight reduction with the increase in demand for safety in the transportation sector. Producing steel grades with a better combination of strength and ductility – moving away from the banana-shaped curve – has become the primary goal for steelmakers. Designing of fully austenitic steels seemed to be a feasible option to achieve steel grades

with superior ductility than the 1st generation AHSS grades. To stabilise 100 % austenite in the final microstructure of the steels, austenite stabilizing elements such as carbon (0.6 wt. %), an interstitial alloying element, and manganese (typically higher than 15 wt. %), a substitutional alloying element, are added in high quantities [4]. The presence of austenite enhances the ductility of the steel, as seen in the case of TRIP steels, and activates other deformation mechanisms such as the formation of twins during straining of the steel which contributes to the strengthening of the steel [7 - 8]. Based on the work hardening mechanism, these steels are termed as TWIP (Twinning Induced Plasticity) steels. TWIP steels actually serve the purpose for which they were made - a good combination of high strength (1000 MPa - 1200 MPa) and superior elongation (50 % - 60 %). However, the addition of significant concentrations of alloying elements results in higher production costs and, even more important, compromises the weldability of the steel [9] hindering their application in automotive sector.

Understanding the traits of 2nd generation AHSS grades, since the beginning of 2000's, efforts have been focussed on producing steel grades with lower concentrations of alloying elements yet with a good combination of properties, called 3rd generation AHSS. These steels consist of a multi-phase microstructure with the majority phase being a strong phase (ultra-fine grained ferrite, martensite, or bainite) and a minor phase that could offer ductility (austenite). Until recently, the 3rd generation AHSS grades most commonly used chemical compositions similar to that of the TRIP steels (0.1 – 0.4 wt. % carbon, 1.0 – 2.0 wt. % manganese, 1.5 % silicon) to produce steel grades with superior properties. The primary strategy in developing 3rd generation AHSS grades involves diffusion of carbon from a supersaturated BCC phase (martensite) into austenite during the isothermal holding to enhance the thermal and mechanical stability of austenite. Hence, it is important to have carbon available for diffusion rather than carbon being consumed by reactions such as carbide precipitation, which can be hindered by the addition of high concentrations of silicon (up to 1.5 wt. %). Examples of steel grades using this strategy are Bainitic Transformation Induced Plasticity (TRIP-B) steels with ultrafine bainitic-austenitic microstructures and Quenching & Partitioning (Q&P) steels with martensitic-austenitic microstructures [10]. Considering that TRIP-B steels requires hours-to-days of isothermal holding while for Q&P steels the isothermal holding lasts for seconds-to-minutes, in terms of industrial processing times, Q&P process can be considered as a relatively efficient process.

The main limitation of the previously discussed TRIP steels is the retention of low volume fraction of retained austenite in the final microstructure with limited alloying content. This is partially resolved through the Q&P steels by stabilizing a higher volume fraction of retained austenite with an overall composition similar to that of TRIP steels (0.1 – 0.4 wt. % carbon, 1.0 – 2.0 wt. % manganese, up to 1.5 % silicon) [11-12]. Studies on mechanical properties by Speer *et al.* [13] showed that Q&P processing, with composition similar to TRIP steels, is effective in producing steel grades with a novel combination of properties that would be difficult to achieve with other processing routes. Through the TRIP effect during straining, the ductility of the material is enhanced. Also, increasing the manganese

content in the steel composition increases the retained austenite volume fraction [11, 14-15]. Moreover, as manganese is a very strong austenite stabiliser, increasing the manganese content in the steel composition can also reduce the temperature and time ranges at which Q&P processing is performed when compared to that used for steels with lower alloying content. This also slightly simplifies the Q&P thermal treatment which in turn reduces carbon emission during the production. Keeping this in mind, there has been an increased interest to use medium-manganese steels (5 wt. % - 8 wt. % Mn) for Q&P processing. However, the exploitation of the properties of manganese through Q&P processing, to enhance the properties of the Q&P steels, initially requires an in-depth study about the microstructural mechanisms involved in such a complex heat-treatment that involves multiple heating and cooling cycles along with an isothermal holding stage. A more detailed review into the Q&P process and its evolution over time will help us understand what can be further explored to enhance the properties of the steel produced through the Q&P process.

Quenching and Partitioning (Q&P) process

The Quenching and Partitioning (Q&P) process was proposed by Speer *et al.* [16]. Figure 1.2 shows the schematic representation of the heat treatment in the Q&P process. This process involves heating the steel to partial austenitisation or full austenitisation temperature followed by quenching to a temperature between martensite start temperature (M_s) and room temperature (R.T.). At this point the microstructure consists of martensite and austenite in selected fractions, plus ferrite if partial austenitisation has been applied. The sample is then annealed at a temperature above quenching temperature and below the intercritical temperature range, termed as partitioning stage. In this stage no phase transformations are intended to take place. Stabilizing of austenite in order to retain it at room temperature is an essential aim of the Q&P process. This is achieved through partitioning of carbon from martensite to austenite during the partitioning stage. Partitioning of carbon occurs due to the chemical potential difference of alloying elements between martensite and austenite. The proposed typical partitioning temperatures for Q&P process are around 350 °C – 450 °C, where carbon partitioning is significant and plays a key role in stabilising austenite [17-23]. Depending on the composition and the applied Q&P heat treatment, during the partitioning stage, competitive reactions such as ferrite formation, carbide precipitation, bainite formation, that consume available carbon, can also be encountered [24-27]. These competitive reactions are usually not beneficial in the Q&P process. After the partitioning stage, the sample is quenched to room temperature. During the final quench, if the austenite at the end of partitioning stage is not sufficiently enriched with carbon, it transforms into fresh martensite (M_2). If it is sufficiently enriched, the austenite is retained at room temperature. The final microstructure mainly comprises primary martensite (M_1) and retained austenite (RA). If competitive reactions occurred during the partitioning stage, carbides and fresh martensite may also be present in the final microstructure [24-29].

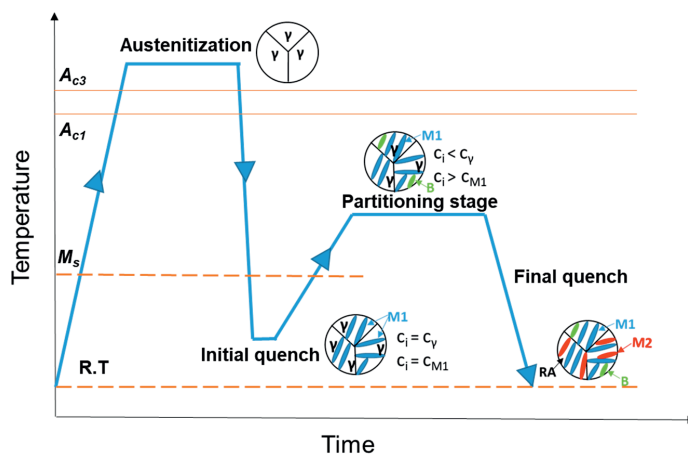


Figure 1.2. Schematic time-temperature diagram of quenching and partitioning (Q&P) process. Here γ represents austenite, M1: primary martensite, M2: secondary/fresh martensite, B: Bainite, RA: retained austenite, C_i : carbon content of steel, C_γ : carbon content of austenite, C_{M1} : carbon content of primary martensite.

The use of medium-manganese steels in the Q&P process has been investigated earlier [24-31]. It was observed that not only the ductility but also the tensile strength of the Q&P steel is increased with increasing manganese content [13]. Although the increase in manganese content enhances the mechanical properties, understanding if this enhancement is a result of the partitioning mechanism is crucial to further optimise the Q&P thermal route. With the advancements in the characterisation techniques, it is possible to detect the manganese concentration in different phases in the final microstructure which can be used to deduce the behaviour of manganese during the Q&P process. Based on the analysis from 3-Dimensional Atom Probe Tomography (3D-APT), Santofimia *et al.* [32] reported partitioning of manganese from martensite to austenite (enriched over 3 nm) after partitioning treatment at 400 °C for 50 s. Recent investigations by other researchers [33-36] show that partitioning at 400 °C and 450 °C for times up to 300 s can lead to austenite grains exhibiting nanoscale manganese enrichment near the martensite/austenite interfaces over a range of less than 5 nm, which is less than the typical thickness (5 – 20 nm) of retained austenite films.

Apart from the partitioning mechanism during the Q&P process, the idea of austenite reverse transformation (ART), formation of austenite from martensitic structure when annealed in the intercritical temperature range, has been effective in retaining high volume fractions of austenite in the final microstructures of Q&P steels [37-39]. Very recently, Ding *et al.* [36] attempted to utilise the concept of partitioning of carbon and manganese, through a Quenching-Austenite Reversion Transformation (Q-ART) process, during which the isothermal holding temperature is in the intercritical range (660 °C for 1 h) of a 0.20C-7.76Mn-1.99Al (wt.%) steel. Based on the microstructural characterisation using nano-auger electron spectroscopy with electron backscatter diffraction (AES-EBSD), a relatively higher enrichment of manganese was observed in the reverted austenite when

compared to the already existing austenite. However, the mechanism related to such higher enrichment in reverted austenite is yet to be understood. The results from Ding's work showed that the strength and ductility of steel partitioned in the intercritical region is higher than that of the steel partitioned at 400 °C for 1 h. These studies explored the Q&P process either at typical partitioning temperatures where the diffusivity of manganese is very low, in the order of 10^{-26} m²/s, when compared to that of carbon (around 10^{-16} m²/s), or at partitioning temperatures in the intercritical range of the respective steels, where manganese partitioning into austenite accompanies the formation of new austenite.

The major objective of this thesis is to investigate the microstructure evolution and to understand the mechanisms involved during the quenching and high-temperature partitioning process of medium manganese steels through experimental and modelling techniques. This Ph.D. thesis studies the Q&P process at partitioning temperatures above the typical partitioning temperatures (350 °C – 450 °C) and below the austenitisation temperature, A_{c1} , of the respective steels (below 650 °C for the medium manganese steels used in the current study), which is important for further optimisation of the Q&P process and controlled addition of alloying elements.

1.2. Research Outline

This Ph.D. thesis consists of an introductory chapter (Chapter 1), four main chapters (Chapters 2 – 5) based on scientific papers that are or will be published in scientific journals. This thesis is concluded by a chapter presenting the main findings of the current work and recommendations for future work (Chapter 6).

Chapter 2 aims to gain insight into the microstructural evolution and competitive reactions occurring in a medium manganese steel during high-temperature partitioning in the Q&P process. Quantitative assessment is performed in order to evaluate the extent in which microstructural processes hinder or inhibit the partitioning of alloying elements during the Q&P heat treatment. The results of this study provide new Q&P microstructural design strategies for medium manganese steels that can minimise or suppress the occurrence of competitive reactions during high-temperature partitioning treatments.

Chapter 3 focuses on understanding the impact of the substitutional alloying elements, nickel and silicon, on the microstructure development of four low-carbon medium-manganese steels during the application of Q&P treatments. New Q&P heat treatments are designed based on previous investigations and results are compared with DICTRA calculations. The insight gained from this study provides an understanding of the interplay between carbon, manganese, silicon and nickel during Q&P processing.

Chapter 4 investigates the interface migration and partitioning kinetics of alloying elements in a medium manganese steel, during partitioning stage of Q&P process, by combining multi-phase field modelling and 3D atom probe tomography experiments. Microstructural mechanisms to promote manganese partitioning and austenite stabilisation are discussed. The influence of austenite and

Chapter 1

martensite grain size, after the initial quench, on carbon partitioning is analysed. The observations from this chapter show that effective stabilisation of austenite in the final Q&P microstructure is possible by applying higher partitioning temperatures at which local partitioning of substitutional elements and interface migration (austenite reversion) are feasible.

Chapter 5 explores the microstructural evolution during Q&P process in medium manganese steels using an in-situ magnetisation technique. This is complemented by dilatometry and X-ray diffraction measurements. The outcome of this chapter shows that the in-situ magnetic measurements allow to decouple the evolution of austenite from the other competitive reactions occurring during the partitioning stage. It is understood that the in-situ magnetisation technique can be a more effective (since it probes the bulk of the sample) and time-saving technique for precise tracking of the evolution of austenite during a heat treatment.

Chapter 6 presents the key conclusions achieved in this thesis and recommendations for future work.

References

1. <https://www.worldautosteel.org/steel-basics/automotive-advanced-high-strength-steel-ahss-definitions/>
2. M.Y. Demeri, **Advanced high-strength steels – Science, technology, and applications**, ASM International, (2013), pp. 59-70.
3. C. Garcia-Mateo, F.G. Caballero, **Comprehensive Materials Processing**, Elsevier Ltd., First Edition, 1 (2014), pp. 165-166.
4. T. Nanda, V. Singh, V. Singh, A. Chakraborty, S. Sharma, **Third generation of advanced high-strength steels: Processing routes and properties**, Journal of Materials: Design & Applications, 223 (2) (2016), pp. 209-238.
5. J. Galan, L. Samek, P. Verleysen, K. Verbeken, Y. Houbaert, **Advanced high strength steels for automotive industry**, Revista De Metalurgica 48 (2012), pp. 118-131.
6. E. Billur and T. Altan, **Three generations of advanced high-strength steels for automotive applications: Part I**, Stamping Journal, (2013), pp. 16-17.
7. N.K. Tewary, S.K. Ghosh, S. Chatterjee, A. Ghosh, **Deformation and annealing behavior of dual phase TWIP steel from the perspective of residual stress, faults, microstructures and mechanical properties**, Materials Science and Engineering A, 733 (2018), pp. 43-58.
8. H. Idrissi, K. Renard, L. Ryelandt, D. Shryvers, P.J. Jacques, **On the mechanism of twin formation in Fe–Mn–C TWIP steels**, Acta Materialia, 58 (2010), pp. 2464-2476.
9. J. K. Larsson, **Avoidance of crack inducement when laser welding hot-formed car body components — a variable analysis**, Physics Procedia, 5 (115) (2010), Laser assisted net shape engineering 6, Proceedings of the LANE 2010, Part 2, pp. 115-124.
10. W. Bleck, F. Bruhl, Y. Ma and C. Sasse, **Materials and Processes for the Third-generation Advanced High-strength Steels**, Berg Huetttenmaenn Monatsh, 164 (11) (2019), pp. 466-474.

11. A.M. Streicher, J.G. Speer, D.K. Matlock and B.C. De Cooman: **Proc. Int. Conf. on Advanced high strength sheet steels for automotive applications**, Warrendale, PA, USA, AIST (2004), pp. 51-62.
12. X.C. Xiong, B. Chen, M.X. Huang, J.F. Wang, L. Wang, **The effect of morphology on the stability of retained austenite in a quenched and partitioned steel**, *Scripta Materialia*, 68 (2013) pp. 321-324.
13. J.G. Speer, E. De Moor A.J. Clarke, **Critical assessment: quenching and partitioning**, *Materials Science and Technology*, 31 (1) (2014), pp. 3-9.
14. M.J. Santofimia, T. Nguyen-Minh, L. Zhao, D.N. Hanlon, T.A. Kop and J. Sietsma: **Proc. Int. Conf. on New developments in advanced high-strength sheet steels**, (ed. Speer J.G. *et al.*), Warrendale, PA, AIST (2008), pp. 191-198.
15. D. De Knijf, R. Petrov, C. Föjer, L.A.I. Kestens: **Proc. Int. Symp. on New developments in advanced high-strength sheet steels**, (ed. De Moor *et al. et al.*), Warrendale, PA, AIST (2013), pp. 185-195.
16. R. Rana, **Special issue on 'Medium manganese steels'**, *Materials Science and Technology*, 35(17) (2019), pp. 2039-2044.
17. J.G. Speer, A.M. Streicher, D. Matlock, F. Rizzo, G. Krauss, **Quenching and partitioning: A fundamentally new process to create high strength trip sheet microstructures**. *Materials Science and Technology Meeting*, 2003: Chicago, IL; United States.
18. J.G. Speer, F. Rizzo, D. Matlock, D.V. Edmonds, **The "quenching and partitioning" process: background and recent progress**. *Materials Research*, 8(4) (2005), pp. 417-423.
19. J.G. Speer, D.K. Matlock, B.C. De Cooman, J.G. Schroth, **Carbon partitioning into austenite after martensite transformation**. *Acta Mater.* 51(9) (2003), pp. 2611-2622.
20. M.J. Santofimia, L. Zhao, J. Sietsma, **Microstructural Evolution of a Low-Carbon Steel during Application of Quenching and Partitioning Heat Treatments after Partial Austenitisation**. *Metallurgical and Materials Transactions A*, 40(1) (2008), pp. 46-57.
21. Thomas, G.A. Speer, J.G., Matlock, D.K. **Quenched and partitioned microstructures produced via Gleeble simulations of hot-strip mill cooling practices**. *Metall. Mater. Trans. A Phys. Metall. Mater. Sci.*, 42, (2011), pp. 3652–3659.
22. A. Arlazarov, M. Ollat, J.P. Masse, M. Bouzat, **Influence of partitioning on mechanical behaviour of Q&P steels**. *Mater. Sci. Eng. A*, 661, (2016), pp. 79–86.
23. A.S. Nishikawa, G. Miyamoto, T. Furuhashi, A.P. Tschiptschin, H. Goldenstein, **Phase transformation mechanisms during Quenching and Partitioning of a ductile cast iron**, *Acta Materialia*, 179 (2019), pp. 1-16.
24. J. Hidalgo, C. Celada-Casero, and M.J. Santofimia, **Fracture mechanisms and microstructure in a medium Mn quenching and partitioning steel exhibiting macro-segregation**, *Materials Science and Engineering: A*, 754 (2019), pp. 766-777.
25. D.V. Edmonds, K. He, M.K. Miller, F.C. Rizzo, A. Clarke, D.K. Matlock, J.G. Speer, **Microstructural Features of 'Quenching and Partitioning': A New Martensitic Steel Heat Treatment**. *Materials Science Forum*, 539-543 (2007), pp. 4819-4825.

26. D.V. Edmonds, K. He, F.C. Rizzo, B.C. De Cooman, D.K. Matlock, J.G. Speer, **Quenching and partitioning martensite—A novel steel heat treatment**. *Materials Science and Engineering: A*, 438–440 (2006), pp. 25-34.
27. J.G. Speer, D.K. Matlock, B.C. De Cooman, J.G. Schroth, **Carbon partitioning into austenite after martensite transformation**. *Acta Materialia*, 51(9) (2003), pp. 2611-2622.
28. M. Gouné, F. Danoix, S.Y.P. Allain, O. Bouaziz, **Unambiguous carbon partitioning from martensite to austenite in Fe–C–Ni alloys during quenching and partitioning**. *Scripta Materialia*, 68(12) (2013), pp. 1004-1007.
29. F. HajyAkbar, J. Sietsma, G. Miyamoto, T. Furuhashi, M.J. Santofimia, **Interaction of carbon partitioning, carbide precipitation and bainite formation during the Q&P process in a low C steel**. *Acta Materialia*, 104 (2016), pp. 72-83.
30. E. De Moor, J.G. Speer, D.K. Matlock, J.H. Kwak, S.B. Lee, **Quenching and partitioning of CMnSi steels containing elevated manganese levels**, *Steel Research International*, 83 (2012), pp. 322-327.
31. Z.R. Hou, X.M. Zhao, W. Zhang, H.L. Liu, H.L. Yi, **A medium manganese steel designed for water quenching and partitioning**, *Material Science and Technology*, 34 (2018), pp. 1168-1175.
32. M.J. Santofimia, L. Zhao, I. Povstugar, P.P. Choi, D. Raabe, J. Sietsma, **Carbon redistribution in a quenched and partitioned steel analysed by atom probe tomography**, in *Proc 3rd int symp steel sci (ISSS 2012)*, N.H. Furuhashi, T. Ushioda, K. Editor. 2012: Kyoto: The Iron and Steel Institute of Japan. pp. 155.
33. E.J. Seo, L. Cho, B.C. De Cooman, **Kinetics of the partitioning carbon and substitutional alloying elements during quenching and partitioning (Q&P) processing of medium Mn steel**, *Acta Materialia*, 107 (2016), pp. 354-365.
34. Tschiyama, T. Inoue, J. Tobata, D. Akami, and S. Takaki, **Microstructure and mechanical properties of a medium manganese steel treated with interrupted quenching and intercritical annealing**. *Scripta Materialia*, 122 (2016), pp. 36-39.
35. Y. Toji, H. Matsuda, M. Herbig, P.P. Choi, D. Raabe, **Atomic-scale analysis of carbon partitioning between martensite and austenite by atom probe tomography and correlative transmission electron microscopy**, *Acta Materialia*, 65 (2014), pp. 215-228.
36. R. Ding, Z. Dai, M. Huang, Z. Yang, C. Zhang, H. Chen, **Effect of pre-existed austenite on austenite reversion and mechanical behaviour of an Fe-0.2C-8Mn-2Al medium Mn steel**. *Acta Materialia*, 147 (2018), pp. 59-69.
37. P. Gibbs, E. De Moor, M.J. Merwin, B. Clausen, J.G. Speer, D.K. Matlock, **Austenite stability effects of tensile behavior of manganese-enriched -austenite transformation-induced plasticity steel**, *Metallurgical and Materials Transactions A*, 42 (2011), pp. 3691–3702.
38. A. Arlazarov, M. Gouné, O. Bouaziz, A. Hazotte, G. Petitgand, P. Barges, **Evolution of microstructure and mechanical properties of medium Mn steels during double annealing**, *Material Science and Engineering A*, 542 (2012), pp. 31–39.
39. H. Luo, J. Shi, C. Wang, W. Cao, X. Sun, H. Dong, **Experimental and numerical analysis on formation of stable austenite during the intercritical annealing of 5 Mn steel**, *Acta Materialia*, 59 (2011), pp. 4002–4014.

2

Microstructure Evolution during Quenching and High-Temperature Partitioning processing of a Medium-Mn Steel

Medium-Mn Quenching & Partitioning (Q&P) steels have been recently considered as potential candidates for the 3rd generation advanced high-strength steels. The processing of these steels aims to induce the partitioning of substitutional alloying elements from martensite to austenite during an isothermal treatment at high temperature, where the diffusivity of substitutional alloying elements is sufficiently high. In this way, austenite increases its concentration of austenite-stabilising elements and thus its thermal stability. This chapter investigates the microstructural evolution during high temperature partitioning treatments in a medium-Mn steel and the possible occurrence of additional phase transformations that may compete with the process of atomic partitioning between martensite and austenite. Q&P routes in which the partitioning steps take place in the range of 400 °C - 600 °C for times up to 3600 s were investigated. The final microstructures display an increased fraction of retained austenite with increasing holding times during partitioning at 400 °C, while higher partitioning temperatures, 450 °C - 600 °C, lead to cementite precipitation in austenite films and pearlite formation in blocky austenite, resulting in a decrease of the fraction of retained austenite with the holding time. This observation is supported with theoretical calculations of the volume change, suggesting that for maximising the fraction of retained austenite, short holding times are preferred during partitioning at high temperatures. It is concluded that the successful application of high-temperature partitioning treatments in medium-Mn steels requires microstructure design strategies to minimise or suppress competitive reactions.

**This chapter is based on: S. Ayenampudi, C. Celada-Casero, J. Sietsma, and M. J. Santofimia: Microstructure evolution during high-temperature partitioning of a medium-Mn Quenching and Partitioning steel, Materialia 8 (2019) 100492.*

2.1. Introduction

The quenching and partitioning (Q&P) process, proposed by Speer and co-workers has been considered as one of the most promising heat treatments for the production of third generation advanced high strength steels (AHSSs) with exceptional combination of strength and ductility [1]. Speer *et al.* [2] proposed the constrained carbon equilibrium (CCE) model to describe the thermodynamics of the carbon partitioning process. The CCE model is characterised by two assumptions: a) the carbon partitioning from martensite to austenite is finalised when the chemical potential of carbon in both phases is equal and b) the martensite/austenite interface is immobile during the partitioning step as the number of iron atoms in each phase are conserved. Typical partitioning temperatures in the Q&P process (350 °C – 450 °C) are relatively low and the diffusivities of substitutional alloying elements during the partitioning step can be ignored at the time ranges that are normally considered. Therefore, most studies are concentrated on studying the stabilisation of austenite by carbon [2-5].

Recently, the idea of stabilizing the austenite through Q&P heat treatments in which the partitioning stage takes place at temperatures high enough to stimulate the partitioning of substitutional alloying elements has been proposed by some authors [6-10]. This possibility stems from the observation of an apparent partitioning of substitutional alloying elements at relatively low temperatures. For example, Santofimia *et al.* [6] reported the partitioning of manganese at typical partitioning conditions (400 °C for 50 s) at some martensite/austenite interfaces. Later, several authors [8-10] observed that the range of manganese partitioning is increased with the increase in partitioning temperature from 400 °C to 450 °C. Some of the recent works [9-12] also aimed at investigating austenite stability in the intercritical range of temperatures by promoting austenite reverse transformation. However, manganese tends to partition into austenite only a few nanometres (typically less than 10 nm) after isothermal holding times of up to 1 hour at these temperatures. Therefore, the partitioning ranges of manganese reported earlier may not be sufficient to stabilise the entire films of retained austenite, which typically have a thickness 5 - 20 nm.

The diffusivity of manganese in austenite, at typical Q&P temperatures (400 °C - 450 °C), is in the order of magnitude of 10^{-26} m²/s [13], which is very low compared to that of carbon, which is around 10^{-16} m²/s [14]. In order to promote manganese partitioning from martensite into austenite it is important to apply higher partitioning temperatures. However, higher isothermal holding temperatures may increase the probability of occurrence of competitive reactions like austenite decomposition into bainite or pearlite (P), or carbide formation [15]. Most of the earlier works reported the occurrence of bainite formation [16] and carbide precipitation inside primary martensite [4, 6] during isothermal holding at lower partitioning temperatures (400 °C - 450 °C). However, there are no research works focused on the microstructural development that takes place during partitioning steps at higher temperatures (500 °C - 600 °C) below the intercritical region.

This chapter aims to gain insight into the microstructural evolution and competitive reactions occurring in a medium-Mn steel during partitioning process, over a temperature and time range, of Q&P heat treatment. For this purpose, a combination of characterisation techniques such as dilatometry, scanning electron microscopy (SEM), X-Ray diffractometry (XRD) and room-temperature magnetometry (VSM) are used.

2.2. Material and Experimental Methods

The chemical composition of the medium-Mn steel used in this study is shown in Table 2.1. The content of manganese is expected to contribute to the stabilisation of the austenite and to delay significantly the formation of structures such as ferrite, and bainite during cooling to the quenching temperature. Silicon is normally used to delay any cementite precipitation during the partitioning step.

Table 2.1. Chemical composition (wt. %) of the steel investigated.

C	Mn	Si	Mo	Al	Cr	Fe
0.31	4.58	1.52	<0.005	0.01	0.02	Balance

The steel was produced in the form of a forged billet. Cylindrical specimens of 10 mm in length and 4 mm in diameter were machined from the forged billet. These specimens were heat treated in a Bähr 805 DIL A/D dilatometer. A type S thermocouple spot-welded on the surface was used to monitor and control temperature. Low pressure on the order of 10^{-4} mbar was used during heating or isothermal segments, and helium was used as the coolant. The error in change in length from dilatometry experiments was estimated as ± 0.01 %.

After the application of the heat treatments, the specimens were cut into half and the surface was prepared by grinding with P800, P1000, and P1200 abrasive papers and polishing with 6, 3 and 1 μm diamond paste. The polished samples were characterised using a Bruker type D8-Advance diffractometer to measure the volume fraction (f_{RA}) and lattice parameter (a_γ) of retained austenite at room temperature. The diffraction angles covered during the measurements are in the range $40^\circ < 2\theta < 130^\circ$, with Co K α radiation (wavelength 0.179026 nm), where the (110) α , (200) α , (211) α , (220) α and the (111) γ , (200) γ , (220) γ , (311) γ peaks are covered. A 0.042° 2θ step size with a counting time per step of 3 s was used. Following the direct comparison method of austenite and martensite peaks suggested by Jatzcak [17], the retained austenite volume fractions and the corresponding uncertainties were calculated. To determine the carbon concentration of retained austenite from its lattice parameter, the equations proposed by Dyson and Holmes [18] and van Dijk *et al.* [19] are combined and adjusted to suit the steel compositions in the current work:

$$a_\gamma = 3.556 \text{ \AA} + \left(0.0453 \frac{\text{\AA}}{\text{wt.}\%}\right) \cdot x_C + \left(0.00095 \frac{\text{\AA}}{\text{wt.}\%}\right) \cdot x_{Mn} + \left(0.00157 \frac{\text{\AA}}{\text{wt.}\%}\right) \cdot x_{Si} + \left(0.0006 \frac{\text{\AA}}{\text{wt.}\%}\right) \cdot x_{Cr} - \left(0.0002 \frac{\text{\AA}}{\text{wt.}\%}\right) \cdot x_{Ni} \quad (2.1)$$

where x_i represents the concentration of the alloying element i in wt.%. The detection limit of the retained austenite fraction by X-ray diffraction is 0.01. If any partitioning of substitutional alloying elements from martensite into austenite has occurred, it is very local and its influence on the average chemical composition of austenite and thus on the austenite lattice parameter will be negligible. Hence, the nominal composition of the alloy and lattice parameter of retained austenite is used to calculate the carbon content of retained austenite from the lattice parameter.

Room temperature microstructural analysis of the samples was carried out using a JEOL JSM-6500F field emission gun scanning electron microscope (FEG-SEM) operating at 15 kV. As a pre-requisite for the microstructural analysis, the specimens are prepared following the same procedure as for X-ray diffraction measurements. The polished specimens are then etched with a 2 % Nital solution. For all steel samples the surface perpendicular to the rolling direction is analysed.

Room temperature magnetic measurements were performed on cubic specimens with an edge dimension of 2.0 mm using a 7307 vibrating sample magnetometer. A standard National Institute of Standards and Technology nickel specimen was used for the calibration. Magnetisation curves at room temperature were measured by a stepwise change in the applied magnetic field from +1.6 to -1.6 T. According to the method indicated by Zhao *et.al* [20] the volume fraction of martensite (f_m) in the quenched specimen is determined by comparing the saturation magnetisation values both on the pure Fe BCC specimen, which is 215 Am²/kg at room temperature [21] and on the specimen with martensite that wants to be measured. The uncertainty in the measurement of the magnetisation/volume fraction during the ex-situ experiments is around ± 0.6 A/m, or which results in an uncertainty in the austenite volume fraction of ± 0.3 %.

2.3. Design of Heat Treatments

To identify the Q&P process parameters, like austenitisation temperature and quenching temperature (T_Q), the starting and finishing austenitisation temperatures under heating, A_{c1} and A_{c3} , were measured. A specimen of the alloy was subjected to full austenitisation, by heating to a temperature of 950 °C at 10 °C/s. After 120 s of isothermal holding, the sample was directly quenched to room temperature at a cooling rate of 30 °C/s. As explained in the work of [22], the A_{c1} and A_{c3} temperatures of the studied alloy was determined from the first derivative of the dilatometry curve with respect to time, leading to 780 \pm 5 °C and 840 \pm 5 °C, respectively. After the identification of A_{c1} and A_{c3} temperatures, a new set of as-quench heat-treatment with austenitisation temperature of $A_{c3} + 50$ °C and cooling rate of 30 °C/s was performed to identify the martensite start temperature (M_s) and the martensite formation kinetics during quenching to room temperature.

Figure 2.1a shows the relative change in length with temperature during the cooling stage of the as-quenched specimen. A quenching followed by reheating heat treatment was performed to characterise the expansion behaviour of the quenched microstructure of the alloy. The change in length behaviour during the reheating cycle gives information on the thermal expansion of the as-quenched specimen

consisting of a mixture of FCC and BCC phases. As shown in Figure 2.1a, the volume fraction of martensite (f_M) at room temperature and its evolution with temperature (Figure 2.1b) was obtained considering the linear expansion of the FCC and BCC lattice and applying lever rule on the respective dilatometry curves. According to the room temperature magnetometer measurements, the as-quenched sample of the alloy comprise about 0.940 ± 0.003 volume fraction of martensite. This martensite fraction corresponds to the final change in length observed at room temperature, as indicated in Figure 2.1a.

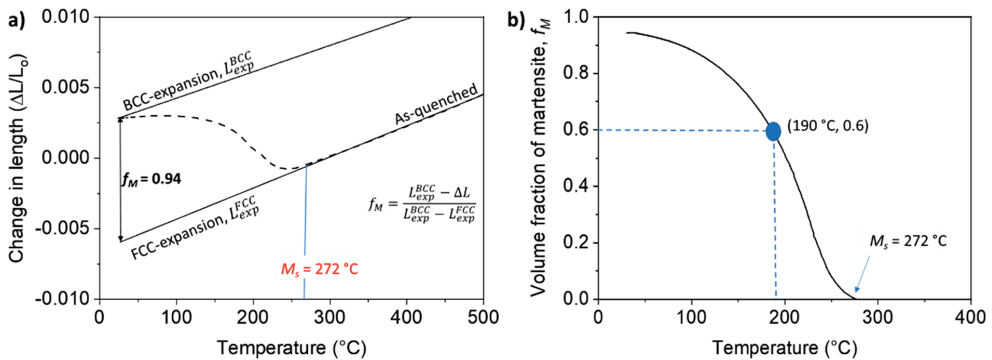


Figure 2.1. (a) Change in length versus temperature curve during quenching of the alloy (dashed line). f_M is the volume fraction of martensite formed after an as-quench heat treatment. (b) Volume fraction of martensite as a function of temperature obtained from the as-quench dilatation curve in Fig 2.1a.

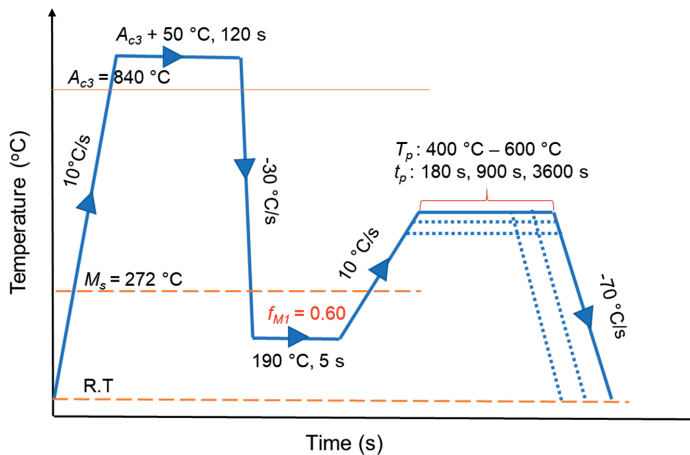


Figure 2.2. Schematic drawing of the Quenching and Partitioning heat treatments applied in the present work.

A set of Q&P heat treatments were designed based on the information deduced so far. The applied thermal routes are shown in Figure 2.2. These thermal routes include a full austenitisation at 890°C for 120 s, quenching at 30°C/s to 190°C . From Figure 2.1b, the selected quenching temperature (T_Q) of 190°C corresponds to the formation of a volume fraction of primary martensite (M_1) equal to 0.60, leaving a volume fraction of untransformed austenite of 0.40. These volume fractions of primary martensite and, consequently, austenite were chosen with the aim to stabilise a significant volume

fraction of austenite in the final microstructures, as the steel has relatively high carbon and manganese content. The partitioning temperatures range from typical values aiming only the austenite stabilisation through carbon partitioning (400 °C) to a temperature of 600 °C (below A_{c1}), which can promote austenite stabilisation through partitioning of substitutional alloying elements. In the following sections and chapters, conditions will be indicated as QP $T_p - t_p$ for concise identification of specimens.

2.4. Results

In this section, the microstructural evolution during the different applied Q&P heat treatments is evaluated based on the dilatometry measurements, X-ray diffraction analysis, magnetisation measurements and microstructural observations.

Figure 2.3 shows the relative change in length with temperature during the cooling stage of the as-quenched specimen, as in Figure 2.1a, and dilatation curve of QP400-3600 (dashed line) specimens, as an example. This dilatometry curve of QP400-3600 specimen is used to explain the microstructural development during the Q&P processing routes.

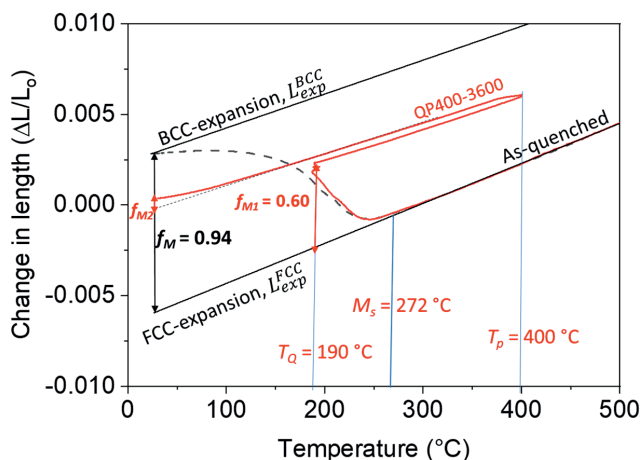


Figure 2.3. Representation of relative change in length versus temperature for an as-quench heat treatment (dashed line) and QP400-3600 heat treatment (solid line) of the studied alloy. f_M is the fraction of martensite formed after an as-quench heat treatment; f_{M1} and f_{M2} are the fractions of primary and fresh martensite formed during QP400-3600 heat treatment, respectively. T_Q and T_P are the initial quench and partitioning temperatures, respectively.

Initially, a linear contraction is detected corresponding to the cooling from the austenitisation temperature. When the temperature decreases below the M_s and until the quench temperature (T_Q), a dilatation corresponding to the formation of 0.60 volume fraction of athermal martensite is observed. Then, the specimen is reheated to 400 °C, during which a continuous expansion is observed, indicating no phase transformations. The small positive change in length observed during the isothermal holding at 400 °C is related to carbon partitioning from martensite to austenite, and it will be discussed in detail in the following sections. During the partitioning step, part of the remaining austenite enriches sufficiently in carbon to be thermally stabilised at room temperature. A small deviation from linearity

of the dilatometry curves during the final quench to room temperature indicates the formation of a small volume fraction of fresh martensite (M2) from the less stable austenite. The volume fractions of fresh martensite (f_{M2}) were determined by comparing the measured change in length with the change in length observed in the directly-quenched specimen. Since, fresh martensite formation occurs from a carbon enriched austenite, an average error of up to ± 0.01 , in the evaluation of volume fraction of fresh martensite, is estimated based on Ref [23]. The retained austenite volume fractions (f_{RA}) in the final Q&P microstructures were measured using X-ray diffractometry as explained in the experimental procedure. The remaining constituents in the final microstructures will be carbides and/or pearlite. The total volume fraction of these constituents, f_{c+p} , was calculated by balance of the phase fractions:

$$f_{M1} + f_{M2} + f_{RA} + f_{c+p} = 1 \quad (2.2)$$

The same method was applied to determine the volume fraction of phases present in all final Q&P microstructures. In the following, this information will be employed together with the microstructural observations in order to understand the microstructural evolution taking place during the partitioning step at the different studied temperatures.

Partitioning at 400 °C

Figure 2.4a shows the change in length observed in the dilatometry specimens during the isothermal holding at 400 °C for 3600 s. The dilatometry curve shows two stages. The first stage is an expansion, which is observed during approximately the first 1800 s. This expansion is related to the process of carbon partitioning from the carbon-supersaturated martensite (M1) into the austenite [24]. The second stage is a plateau followed by a slight contraction, which is likely due to the precipitation of carbides in primary martensite, as previously observed by Toji *et al.* [11].

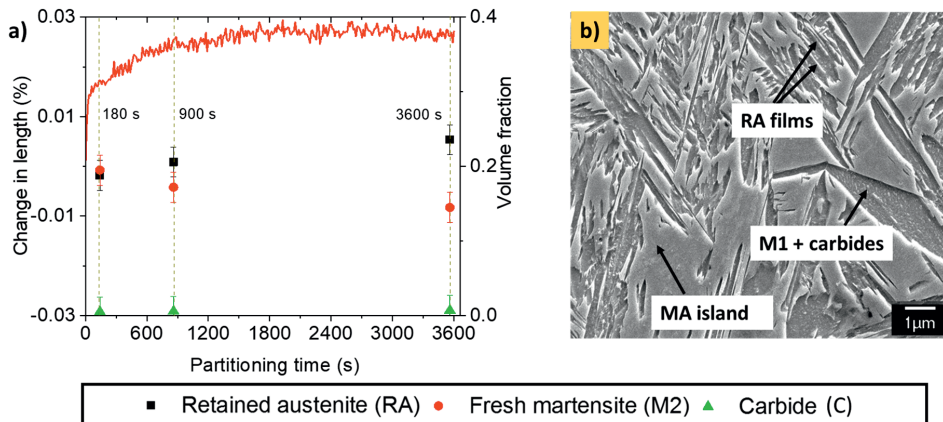


Figure 2.4. (a) Change in length and volume fraction of phases present at the end of the QP400 heat treatments as a function of the partitioning time. (b) Microstructure observed by SEM of the specimen partitioned for 3600 s at 400 °C.

The final microstructures show an increase in the volume fraction of retained austenite and a decrease in the volume fraction of fresh martensite with increasing holding times. This evolution results from the process of carbon partitioning from martensite to austenite, which progressively stabilises the austenite during the partitioning step.

Figure 2.4b shows the microstructure of the specimen after partitioning at 400 °C for 3600 s. The primary martensite, which is carbon-depleted and partially tempered, is characterised by the presence of carbides. The microstructure also show blocky islands of fresh martensite/retained austenite (MA islands) with a thickness of few micrometres. Nanometric retained austenite films are also observed in between the martensite laths.

Partitioning at 450 °C

The dilatometry curve during the partitioning step at 450 °C for 3600 s is shown in Figure 2.5a. A small expansion is observed within the first 40 s (zoomed-in in the inset), which is related to carbon partitioning. After 40 s a continuous decrease in length is observed, which may be related with a more pronounced precipitation process than that observed during partitioning at 400 °C. Kannan *et al.* [25] and Onink *et al.* [26] observed that austenite films saturated with carbon tend to decompose into carbon-depleted austenite and cementite and this phenomenon is accompanied by contraction. The volume fractions of retained austenite and fresh martensite present after partitioning at 450 °C for different times show exactly the opposite trend as that observed after partitioning at 400 °C. That is, an increase in the volume fraction of fresh martensite and a decrease in the volume fraction of retained austenite. After partitioning for 3600 s, the volume fraction of retained austenite is essentially the same as that present in the as-quenched state.

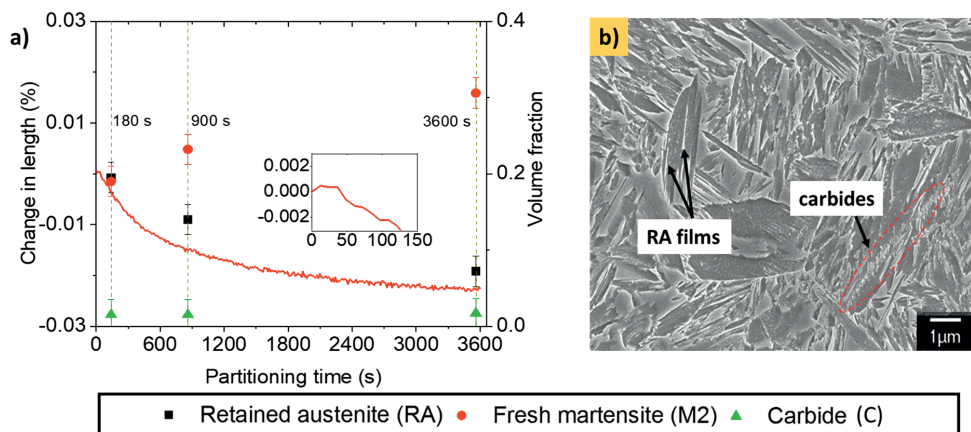


Figure 2.5. (a) Change in length and volume fraction of phases present at the end of the QP450 heat treatments as a function of the partitioning time. (b) Microstructures of the specimens observed under the SEM after partitioning for 3600 s at 450 °C.

Figure 2.5b shows a SEM micrograph of the specimen partitioned at 450 °C for 3600 s. In this case, the precipitation of carbides inside primary martensite is not as evident as in the case of partitioning at 400 °C. Arrays of parallel carbides aligned in the direction of the martensite laths can be clearly observed in the primary martensite, as indicated in Figure 2.5b with dashed lines. These arrays of carbides appear to occupy the locations where austenite films were observed at shorter partitioning times.

Partitioning at 500 °C

The dilatometry curve corresponding to partitioning at 500 °C shows a decrease in change in length for the first 600 s (Figure 2.6a). This contraction is of the same order of magnitude as the one observed during partitioning at 450 °C (Figure 2.5a) although in the present case it occurs in a shorter time. This contraction is followed by a continuous dilatation until the end of the partitioning stage.

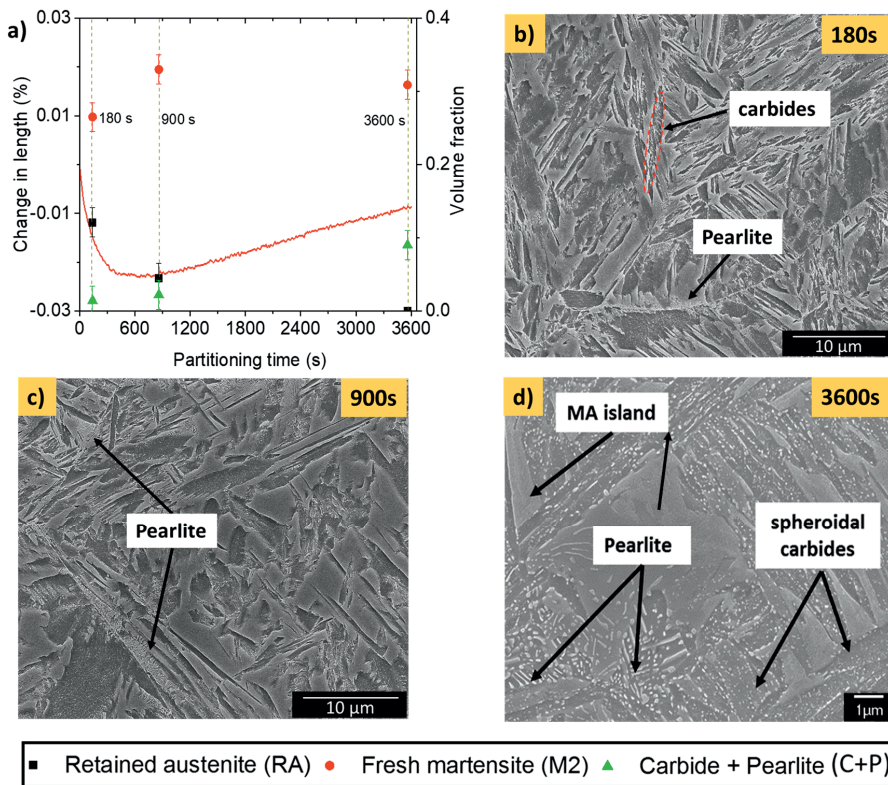


Figure 2.6. (a) Change in length and volume fraction of phases present at the end of the QP500 heat treatments as a function of the partitioning time; Microstructures of the specimens observed under the SEM after partitioning at 500 °C for a) 180s, b) 900s and c) 3600 s.

Figure 2.6a shows that, with the increase in holding time, the volume fraction of retained austenite decreases continuously until it is not detected by X-ray diffraction after partitioning for 3600 s. This decrease in the retained austenite volume fraction coincides with the increase in the volume fraction of fresh martensite, carbides and pearlite.

Chapter 2

The microstructure of the specimen after partitioning at 500 °C for 180 s, 900 s and 3600 s are shown in Figure 2.6b, 2.6c, and 2.6d, respectively. Pearlite is identified in all the final microstructures and the pearlite presence is also observed to increase with partitioning time. This suggests that the increase in length observed in the dilatometry curve is related to pearlite formation, which becomes the dominant process after 900 s of isothermal holding, as can be seen from the SEM micrographs. Precipitation of carbides is observed at the phase boundaries of fresh martensite/retained austenite islands with the surrounding primary martensite.

Partitioning at 550 °C

The dilatometry curve during partitioning at 550 °C (Figure 2.7a) shows a very similar behaviour as the one at 500 °C. However, in the present case, the transition from contraction to expansion occurs at a shorter holding time (200 s) and the magnitude of the contraction is smaller. Moreover, the final expansion observed in the dilatometry curve is higher than in the case of partitioning at 500 °C, which indicates that a larger volume fraction of pearlite forms during partitioning at 550 °C.

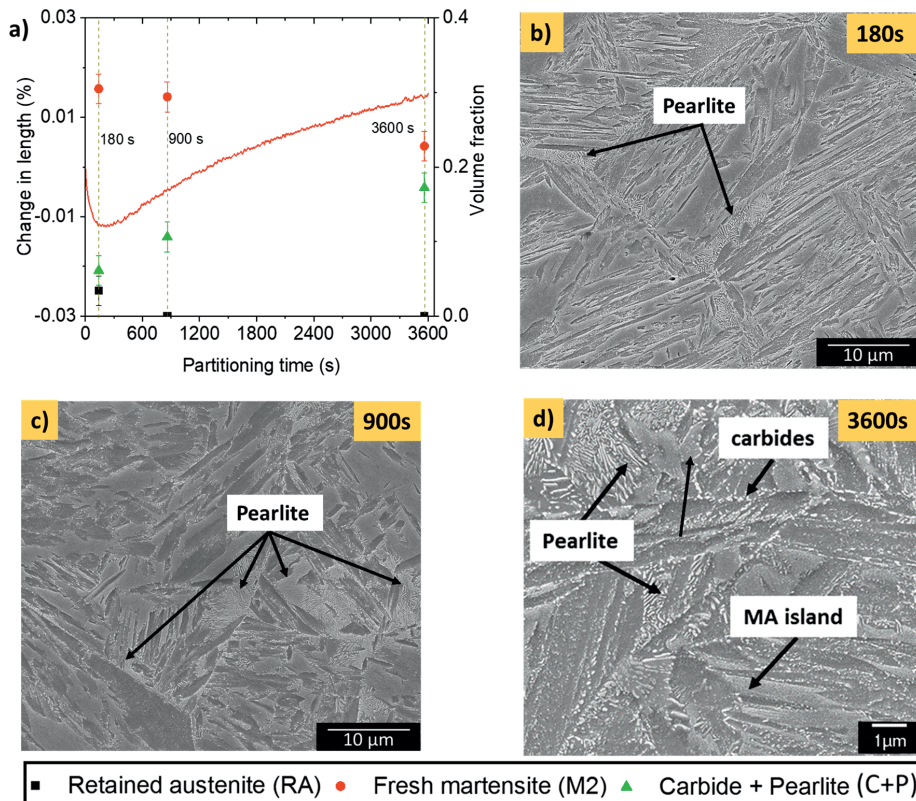


Figure 2.7. (a) Change in length and volume fraction of phases present at the end of the QP550 heat treatments as a function of the partitioning time; Microstructures of the specimens observed under the SEM after partitioning at 550 °C for b) 180s, c) 900s and d) 3600 s. Here, MA island represents Martensite/Retained Austenite island.

The evolution of phase fractions in the final microstructure presented in Figure 2.7a shows that no retained austenite is detected by XRD after 900 s of partitioning, while the volume fraction of carbides and pearlite significantly increases with increasing the holding time.

Figure 2.7b, 2.7c, and 2.7d show the microstructure of the specimens after partitioning at 550 °C for 180 s, 900 s and 3600 s, respectively. The SEM micrograph of the specimen partitioned for 550 °C for 3600 s shows a dense distribution of pearlite in the final microstructure when compared to the lower partitioning times. The fresh martensite/retained austenite islands (MA islands) are less evident in the present case than after partitioning at 500 °C.

Partitioning at 600 °C

The dilatometry curve registered during partitioning at 600 °C for 3600 s is shown in Figure 2.8a. The trends observed in the curve are very similar to the ones observed during partitioning at 550 °C, including the time at which the transition from contraction to expansion occurs. However, the specimen partitioned at 600 °C experiences a smaller expansion than in the case of partitioning at 550 °C, indicating the formation of a lower volume fraction of pearlite.

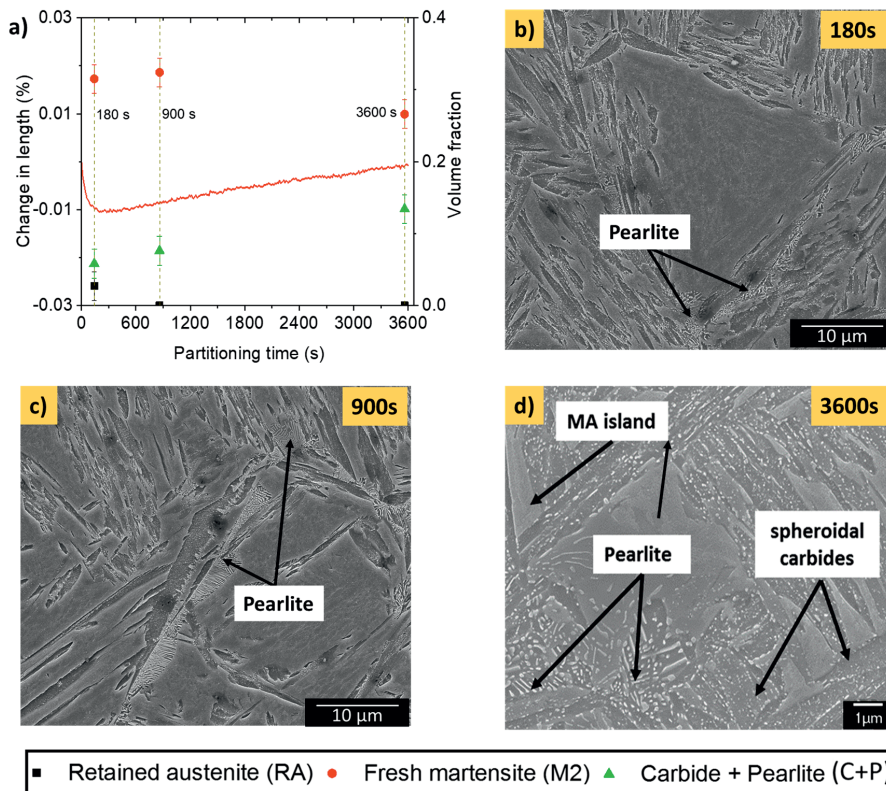


Figure 2.8. (a) Change in length and volume fraction of phases present at the end of the QP600 heat treatments as a function of the partitioning time; Microstructures of the specimens observed under the SEM after partitioning at 600 °C for b) 180s, c) 900s and d) 3600 s. Here, MA island represents Martensite/Retained Austenite island.

The final volume fractions also show similar trends with the partitioning time as the ones observed during partitioning at 550 °C. That is, a low volume fraction of retained austenite that becomes undetectable by XRD after partitioning for 900 s and a simultaneous increase of the volume fraction of carbides and pearlite with partitioning time.

Pearlite is also observed in the SEM micrograph of the specimens partitioned at 600 °C for 180 s, 900s and 3600 s (Figure 2.8b, 2.8c and 2.8d). SEM micrographs indicate that pearlite formation during partitioning stage is more significant at 550 °C than at 600 °C which is also evident from Figure 2.8a. Moreover, carbides in primary martensite observed at 600 °C seem to be coarser than after partitioning at 550 °C. Besides pearlite, lamellar carbides are observed in the fresh martensite/retained austenite islands after partitioning at 600 °C.

2.5. Discussion

The previous section has presented a qualitative description of the microstructural evolution taking place during the partitioning step at the different studied temperatures. In this section, a quantitative assessment is performed in order to evaluate the extent to which microstructural processes hinder or inhibit the partitioning of carbon and substitutional alloying elements from the martensite into the austenite and, therefore, promote an adequate stabilisation of the austenite to room temperature. For this purpose, firstly, the redistribution of carbon among phases and due to phase transformations during the partitioning stage is analysed based on the carbon balance at different partitioning temperatures. Then, the sequence of microstructural mechanisms occurring at different partitioning temperatures is validated through theoretical calculations of the length change. Finally, it is discussed how simultaneous microstructural phenomena during partitioning influence the stabilisation of the austenite at different temperatures and the most promising routes are identified.

2.5.1. Carbon Balance at Different Partitioning Temperatures

It is crucial to assess how carbon redistributes in the microstructure during the partitioning stage to understand the stabilisation process of the austenite. Therefore, in this section, the carbon distribution is quantified by the analysis of the carbon content of all microstructural constituents present in the microstructures after Q&P heat treatments in which the partitioning time lasted for 3600 s. This evaluation provides information on the effectiveness of the carbon partitioning from martensite to austenite in order to stabilise austenite at room temperature.

The carbon content in the phases at the very beginning of partitioning stage ($t_p = 0$ s) can be represented by:

$$\bar{x}(t_p = 0 \text{ s}) = f_\gamma \cdot x_\gamma + f_{M1} \cdot x_{M1} \quad (2.3)$$

where \bar{x} is the total carbon content present in the alloy (0.31 wt. %), f_γ and f_{M1} are the volume fractions of austenite and martensite present at the beginning of the partitioning stage (0.40 and 0.60 respectively),

and x_γ and x_{M1} are the carbon concentrations present in austenite and martensite at the beginning of the partitioning stage. Since the martensitic transformation is diffusionless and considering that there is no change in carbon concentration during the reheating stage, martensite and austenite are assumed to have the same carbon content (0.31 wt.%) at the onset of the partitioning stage. These initial conditions at the beginning of the partitioning stage are considered equal for all studied Q&P heat treatments.

Section 3 has shown that, during the partitioning step, several competitive phenomena occur at different stages of the isothermal holding depending on the partitioning temperature. These phenomena are carbide precipitation in martensite, pearlite formation, carbide precipitation in austenite and carbon enrichment of the austenite. All these phenomena compete for the carbon available in the microstructure. Therefore, after 3600 s of partitioning, the following carbon balance can be applied:

$$\bar{x}(t_p = 3600s) = f_\gamma \cdot x_c^Y(t_p = 3600s) + f_{M1} \cdot x_c^{M1}(t_p = 3600s) + f_p \cdot x_c^P(t_p = 3600s) + X_c(t_p = 3600s) \quad (2.4)$$

where \bar{x} is the total fraction of carbon present in the alloy (0.31 wt. %), f_i and x_c^i represent the volume fraction and carbon content of phase i ($i = \gamma, M1$ and P) after 3600 s of isothermal holding and before the final quench to room temperature and X_c is the total fraction of carbon that is precipitated in carbides, in wt. %.

The volume fraction of austenite at the end of the partitioning step and before the final quench, f_γ , can be calculated as the sum of volume fractions of retained austenite and fresh martensite observed in the final microstructures. The corresponding carbon content (x_c^Y) is calculated considering the carbon content in retained austenite (x_c^{RA}) measured by X-ray diffractometer and the carbon content in fresh martensite (x_c^{M2}). This balance can be formulated as:

$$f_\gamma \cdot x_c^Y(t_p = 3600s) = f_{RA} \cdot x_c^{RA}(t_p = 3600s) + f_{M2} \cdot x_c^{M2}(t_p = 3600s) \quad (2.5)$$

where f_{RA} and f_{M2} are the volume fractions of retained austenite and fresh martensite, respectively.

The carbon content in fresh martensite (x_c^{M2}) is determined based on the martensite start temperature during the final quench and applying the Rowland and Lyle equation [27] that relates the martensite start temperature (in °C) with the chemical composition of the alloy. In the present study the equation has been adapted to the chemical composition of the steel as

$$M_s = 499 \text{ }^\circ\text{C} - (324 \frac{^\circ\text{C}}{\text{wt.}\%}) \cdot x_c^{M2} - (32.4 \frac{^\circ\text{C}}{\text{wt.}\%}) \cdot x_{Mn} - (16.2 \frac{^\circ\text{C}}{\text{wt.}\%}) \cdot x_{Ni} - (27 \frac{^\circ\text{C}}{\text{wt.}\%}) \cdot x_{Cr} - (10.8 \frac{^\circ\text{C}}{\text{wt.}\%}) \cdot x_{Si} - (10.8 \frac{^\circ\text{C}}{\text{wt.}\%}) \cdot x_{Mo} \quad (2.6)$$

where x_i represents the concentration of element i ($i = C, Mn, Ni, Cr, Si$ and Mo) in the alloy in wt. %.

The carbon content in solid solution in primary martensite, x_c^{M1} , is assumed to be zero after 3600 s of partitioning time at all studied partitioning temperatures due to the formation of carbides in the matrix

Chapter 2

and the carbon partitioning to austenite. The carbon content in pearlite is assumed to be the eutectoid carbon content.

Under these assumptions, the combination of Equations 2.4-2.6 provides information regarding the carbon present in every microstructural constituent and in carbides after 3600 s of partitioning at all studied temperatures. The results and details of the numerical values used in the calculations are presented in Table 2.2 and are explained by partitioning temperature hereafter.

Table 2.2. Volume fraction and carbon content of microstructural constituents present at the end of the partitioning step for different partitioning temperatures. These phases are carbon enriched austenite (γ), primary martensite (M1), pearlite (p) and carbides (X_c). The Table also shows the volume fractions and carbon contents of fresh martensite (M2) and retained austenite (RA) used for the estimation of the volume fraction (f_i) and carbon content (x_c^i) of carbon enriched austenite (γ) present after 3600 s of partitioning time.

T_p (°C)	C enriched austenite					C depleted martensite		Pearlite		Carbides
	f_γ	x_c^γ (wt. %)				f_{M1}	x_c^{M1} (wt. %)	f_p	x_c^p (wt. %)	X_c (wt. % C)
		M2		RA						
x_c^{M2}	f_{M2}	x_c^{RA}	f_{RA}							
400	0.39	0.68	0.16	0.23	0.80	0.6	0	0	0	0.01
450	0.39	0.58	0.32	0.07	0.60			0	0	0.08
500	0.31	0.45	0.31	-	-			0.08	0.73	0.11
550	0.22	0.32	0.22	-	-			0.17	0.73	0.11
600	0.27	0.35	0.27	-	-			0.12	0.73	0.12

Partitioning at 400 °C

During the isothermal holding at 400 °C for 3600 s, carbon partitioning from martensite to austenite and carbide precipitation in primary martensite occur in the microstructure. Pearlite formation is not observed. With this information, the application of Equation 2.3 reveals that the fraction of carbon that precipitates in the form of carbides (X_c) in primary martensite is around 0.01 wt. % C.

Partitioning at 450 °C

During partitioning at 450 °C, carbide precipitation in austenite films takes place along with carbon partitioning from martensite to austenite and carbide precipitation in primary martensite. In this case, the balance of carbon shows that the fraction of carbon that precipitates in carbides, X_c , is around 0.08 wt. % C, which is higher than that observed in the case of partitioning at 400 °C and coincides with the microstructural observations.

Partitioning at 500 °C, 550 °C and 600 °C

Partitioning at 500 °C, 550 °C and 600 °C promotes pearlite formation along with carbon partitioning from martensite to austenite, carbide precipitation in primary martensite and carbide precipitation in

austenite. The carbon balance shows that the fraction of carbon that precipitates in the form of carbides, X_C , is around 0.11 wt. % in the case of partitioning at 500 °C and 550 °C, and of 0.12 wt. % in the case of partitioning at 600 °C.

The maximum volume fraction of pearlite is observed after partitioning at 550 °C (Figure 2.7a). This coincides with the nose of the pearlite formation in the theoretically calculated Temperature-Time-Transformation diagram, using the free program MUCG83 [28].

2.5.2. Length Changes Associated to the Reactions occurring during the Partitioning Stage

The focus of this section is on the evaluation and validation of the influence of each microstructural mechanism on the overall change in length observed at the end of the partitioning process. This provides insight into the sequence of the microstructural processes occurring at different partitioning temperatures. According to the mechanisms proposed in the previous section based on the dilatometry results and microstructural observations and using the phase volume fractions and carbon contents calculated in Table 2.2, the theoretical change in length associated to each microstructural process during the partitioning stage is calculated and compared with the experimental values.

The relation between the relative change in length recorded during a dilatometry experiment and the actual change in volume that develops in the material can be expressed as:

$$\frac{\Delta L}{L_i} = \frac{1}{3} \cdot \frac{V^f - V^i}{V^i} \quad (2.7)$$

where $\Delta L = L_f - L_i$ is the difference between the final (L_f) and initial (L_i) length of the material after and before the partitioning stage, respectively. V^f and V^i are the total specific volumes of the material after and before the partitioning stage, respectively. In the present analysis, the initial state, i , represents the starting point of the partitioning step ($t_p = 0$ s) and the final stage, f , represents the end of the partitioning stage after 3600 s ($t_p = 3600$ s).

The total specific volume, V , of the material at any stage of the isothermal holding can be expressed as:

$$V = \sum_j v_j \cdot f_j \quad (2.8)$$

where v_j and f_j are the specific volume and volume fraction of every microstructural constituent, j . In this context, the phases present in the microstructure at the beginning of partitioning stage ($t_p = 0$ s) are primary martensite and untransformed austenite, whereas the microstructural constituents that are present at the end of the partitioning step ($t_p = 3600$ s) depend on the partitioning temperature (see Table 2.2).

Equation 2.7 can be rewritten including the specific volumes, as expressed in Equation 2.8, of all possible individual phases at the beginning and at the end of the partitioning step as:

$$\frac{\Delta L}{L_0} = \frac{1}{3} \cdot \frac{\{(\vartheta_{\gamma}^f \cdot f_{\gamma}^f + \vartheta_{M1}^f \cdot f_{M1}^f + \vartheta_p^f \cdot f_p^f + \vartheta_{carbides}^f \cdot f_{carbides}^f) - (\vartheta_{\gamma}^i \cdot f_{\gamma}^i + \vartheta_{M1}^i \cdot f_{M1}^i)\}}{(\vartheta_{\gamma}^i \cdot f_{\gamma}^i + \vartheta_{M1}^i \cdot f_{M1}^i)} \quad (2.9)$$

where $\vartheta_{\gamma}^i, \vartheta_{M1}^i$ and f_{γ}^i, f_{M1}^i are the specific volumes and volume fractions of austenite and martensite before partitioning stage. $\vartheta_{\gamma}^f, \vartheta_{M1}^f, \vartheta_p^f, \vartheta_{carbides}^f$ and $f_{\gamma}^f, f_{M1}^f, f_p^f, f_{carbides}^f$ stands for the specific volume and volume fraction of carbon enriched austenite, primary martensite, pearlite and carbides at the end of partitioning stage, respectively.

The specific volumes of the crystal structures are calculated from the corresponding lattice parameters and thermal expansion coefficients according to the formulae presented in Table 2.3. The lattice parameters of a particular crystal structure at a given partitioning temperature T can be calculated using the following equation:

$$a_{lattice,T} = a_{lattice,RT} \cdot (1 + \beta \cdot (T - 300 \text{ K})) \quad (2.10)$$

where β is the thermal expansion coefficient, $a_{lattice,T}$ and $a_{lattice,RT}$ are the lattice parameters at the partitioning temperature and room temperature (300 K), respectively. Lattice parameters at room temperature $a_{lattice,RT}$ for austenite (γ), martensite (α') and cementite (θ) are calculated as a function of chemical composition (in at. %) and are shown in Table 2.3.

Depending on the phenomena observed at each partitioning temperature, Equation 2.9 is modified accordingly to calculate theoretical changes in length.

Table 2.3. Equations used to calculate the specific volume and lattice parameter of martensite (α'), austenite (γ) and cementite (θ). Carbon concentrations are in at. % and temperatures are in Kelvin.

	Specific Volume	Lattice parameter (Å)	Ref.	Linear thermal expansion coefficient (β , K ⁻¹)	Ref.
γ	$v_{\gamma} = 1/4 \cdot a_{\gamma}^3$	$a_{\gamma} = 3.556 \text{ \AA} + 0.0453 \text{ \AA} / \text{at}\% \cdot x_c + 0.00095 \text{ \AA} / \text{at}\% \cdot x_{Mn}$	[29]	$1.244 \cdot 10^{-5}$	[30]
α'	$v_{\alpha'} = 1/2 \cdot c_{\alpha'} \cdot a_{\alpha'}^2$	$a_{\alpha'} = 2.8664 - 0.0028 \cdot x_c$ $c_{\alpha'} = 2.8664 + 0.0256 \cdot x_c$	[29]	$2.065 \cdot 10^{-5}$	[30]
θ	$v_{\theta} = 1/12 \cdot a_{\theta} \cdot b_{\theta} \cdot c_{\theta}$	$a_{\theta} = 5.0895, b_{\theta} = 6.7449, c_{\theta} = 4.5250$	[31]	$5.586 \cdot 10^{-6}$	[31]

For the theoretical calculations of change in length, carbide precipitation in primary martensite is neglected at all partitioning temperatures, as the volume fraction of carbides formed at 400 °C is lower than 0.01 and even lower at higher partitioning temperatures (450 °C – 600 °C).

During partitioning at high temperatures (450 °C – 600 °C), precipitation of carbides inside austenite is observed. Through EBSD phase maps, Kannan *et al.* [25], observed that the nature of carbide

precipitated inside austenite during isothermal holding at 500 °C is cementite (6.67 wt. %). By means of ThermoCalc calculations and DICTRA simulations of the carbon redistribution between martensite and austenite during partitioning at 500 °C, it has been recently shown that the carbon content of austenite films in between martensite laths can reach values above 1.50 wt. % C in less than 1 s [32]. This carbon content in austenite is well above the eutectoid composition of the alloy at 500 °C (0.48 wt. % C). This means that, within the range of temperatures of 450 °C – 600 °C, the austenite might be supersaturated in carbon so that cementite can form, causing carbon impoverishment in the surrounded austenite. It was also observed that, at 450 °C, cementite formation from the carbon supersaturated austenite, causes a continuous contraction over 1 h of partitioning time, whereas, at 500 °C, a similar contraction in magnitude occurs predominantly during the first 600 s. Therefore, under the assumption that the nature of carbides precipitated is cementite, change in length calculations show that the volume fraction of cementite precipitated in austenite at all partitioning temperatures is around 0.01. For the theoretical change in length calculations at partitioning temperatures of 500 °C – 600 °C, pearlite ($\gamma \rightarrow \alpha + \theta$) is also included as it was also observed during the partitioning stage.

Table 2.4. Experimental and calculated changes in length at the different partitioning temperatures (T_p) after 3600 s of partitioning time (t_p) in relation with the dominant phenomena occurring during the partitioning stage.

T_p , °C	Major phenomena	Experimental change in length (%), ± 0.010 %	Theoretical change in length (%) at $t_p = 3600$ s
400	C-partitioning	0.029	0.032
450	C-partitioning; Carbide precipitation in γ	- 0.023	- 0.020
500	C-partitioning; Carbide precipitation in γ ; Pearlite formation	- 0.008	- 0.017
550	C-partitioning; Carbide precipitation in γ ; Pearlite formation	0.015	0.010
600	C-partitioning; Carbide precipitation in γ ; Pearlite formation	- 0.001	- 0.002

Table 2.4 summarises the major phenomena occurring at each partitioning temperature as well as the experimental and theoretical changes in length at the end of the partitioning step ($t_p = 3600$ s). The theoretical changes in length are calculated using 2.7 – 2.10 depending on the phases present at the respective partitioning temperature and using the data from Table 2.2. There exists a good agreement between the experimental and theoretical change in lengths, which indicates that the above-mentioned considerations, *i.e.* cementite as the carbide that precipitates inside primary martensite and from austenite, and complete carbon-depletion in primary martensite, are adequate.

2.5.3. Analysis of Simultaneous Phenomena occurring during High-Temperature Partitioning Stages

It is well known that Q&P heat treatments aim to produce steels with good combinations of ductility and strength, which is achieved mainly from retained austenite and primary martensite, respectively [33-35]. In order to stabilise a significant fraction of retained austenite in the final microstructure it is important to avoid other reactions during the partitioning stage that might compete for the available carbon.

The microstructural evolution observed during partitioning at 400 °C confirms that the major phenomena occurring is the carbon partitioning from martensite to austenite, responsible for the retention of a volume fraction of austenite between 0.19 and 0.24 at room temperature after partitioning for 180 s and 3600 s, respectively. On the contrary, at 450 °C, an increase in partitioning time leads to a reduction in the volume fraction of retained austenite, while the fraction of fresh martensite, consequently, increases. This might be attributed to the precipitation of carbides in austenite during the partitioning stage, which reduces the total fraction of carbon available to stabilise the austenite at room temperature [32]. Considering the partitioning temperature of 500 °C, the maximum volume fraction of retained austenite is observed after partitioning for 180 s and the formation of pearlite is observed after 900 s. At higher partitioning temperatures, 550 °C and 600 °C, pearlite is observed after 180 s of isothermal treatment and the volume fraction of retained austenite is lower than 0.05. The further increase in the isothermal holding time does not rise the volume fraction of retained austenite; however, the pearlite volume fraction is observed to increase. It is evident that the microstructures show a tendency to form pearlite at high partitioning temperatures (500 °C - 600 °C). The formation of pearlite from the austenite grains during partitioning consumes part of the volume fraction of austenite and part of the carbon available for austenite stabilisation. Thus, the retained austenite fraction in the final Q&P microstructure is reduced.

As discussed earlier, the dilatometry analysis at the partitioning temperatures of 500 °C to 600 °C indicate that carbide precipitation inside austenite and pearlite formation occur simultaneously. The change in slopes of dilatometry curves during isothermal holding indicate a transition from a dominant process of carbide precipitation inside austenite (causing contraction) to a dominant process of pearlite formation (causing expansion). Figure 2.9a, 2.9b and 2.9c show the dilatometry curve (red line), extrapolation of contraction (blue line) and expansion (green line) behaviour of the actual dilatometry curve at 500 °C, 550 °C and 600 °C, respectively. By relating the final volume fraction of pearlite and the extrapolation of the dilatometry curve corresponding to pearlite formation (Figure 2.9), the evolution of the volume fraction of pearlite with isothermal holding time at partitioning temperatures of 500 °C, 550 °C and 600 °C is calculated and shown in Figure 2.10a. From Figure 2.9 and Figure 2.10a, the transition in the pre-dominant behaviour of carbide precipitation in austenite to pearlite formation during

the partitioning stage is identified to be when the volume fraction of pearlite is in the range of 0.01 – 0.03.

For the investigated steel, the precipitation of carbides inside austenite seems to be unavoidable, as it occurs at the very early stage of the partitioning step and as a result of the rapid carbon enrichment in austenite prompted at high partitioning temperatures. However, pearlite formation can be minimised to 0.01 volume fraction by restricting the isothermal holding to short times. Using information from Figure 2.10a, the TTT diagram shown in Figure 2.10b is constructed, where the partitioning times corresponding to pearlite volume fractions of 0.01 and 0.05 are indicated. It can be seen from Figure 2.10b that, similar to what is predicted from the theoretical calculations using the MUCG83 program, the kinetics of pearlite formation is faster at partitioning temperatures around 550 °C (close to the nose of pearlite formation) than above or below.

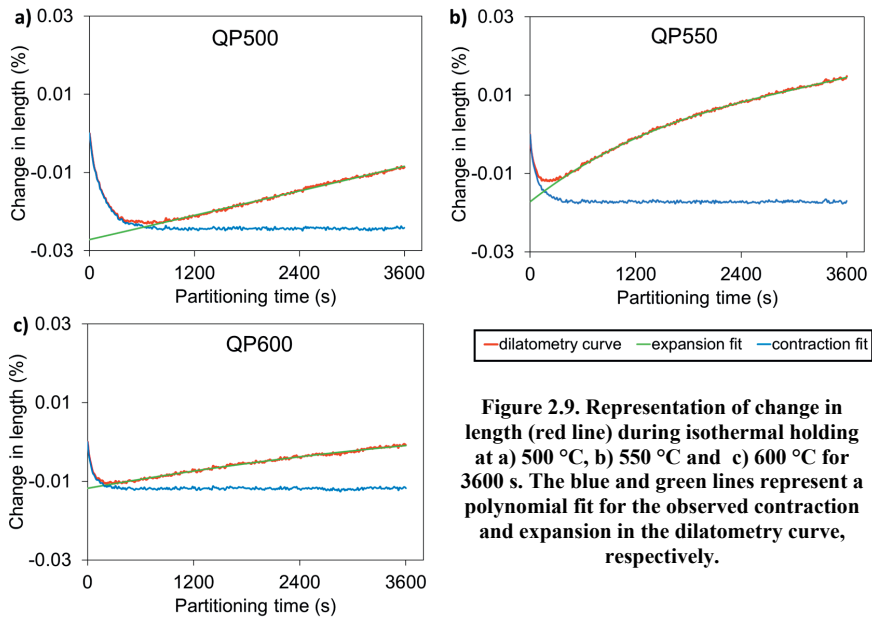


Figure 2.9. Representation of change in length (red line) during isothermal holding at a) 500 °C, b) 550 °C and c) 600 °C for 3600 s. The blue and green lines represent a polynomial fit for the observed contraction and expansion in the dilatometry curve, respectively.

The morphology and location of the austenite after the initial quench seems to play a role in the degree of carbon enrichment during the partitioning step and, thus, in the precipitation of carbides or formation of pearlite within austenite. Based on the SEM observations from Figure 2.5b, it is roughly estimated that around a 0.20 volume fraction of the austenite films are occupied with cementite. Based on the carbon balance calculations, during the partitioning stage, if an austenite film is enriched with about 1.88 wt.% carbon then it is possible for 0.20 volume fraction of cementite precipitation in this austenite film. Here, it is assumed that the austenite surrounding the cementite particles is retained at room temperature and this austenite has at least the minimum carbon content required for austenite stabilisation at room temperature (0.68 wt. % C as measured by XRD). This carbon content is in good

agreement with the carbon-redistribution simulation results performed by DICTRA at 500 °C, on the same alloy as studied in the current work, by Hidalgo *et al.* [32].

In the case of pearlite formation, it is observed to nucleate along the prior austenite grain boundaries, where the diffusion of carbon is enhanced compared to that in bulk and, thus, a rapid carbon enrichment of the austenite is expected at these locations. Yang *et al.* [16] reported that bigger austenite grains are highly favourable regions to form pearlite. Hidalgo *et al.* [32] showed by DICTRA simulations that, at a partitioning temperature of 500 °C, austenite blocks of 0.3-0.5 μm in thickness can reach homogeneous carbon concentrations close to the eutectoid composition (0.80 wt. % C) after 50 s of isothermal holding, which makes the transformation of such austenite into pearlite thermodynamically possible. At higher partitioning temperatures (550 °C and 600 °C), carbon diffuses even faster and tends to homogenise across the austenite grain in a shorter time which would allow an earlier pearlite formation. Due to pearlite formation the volume fraction of austenite available for stabilisation through manganese partitioning is consumed.

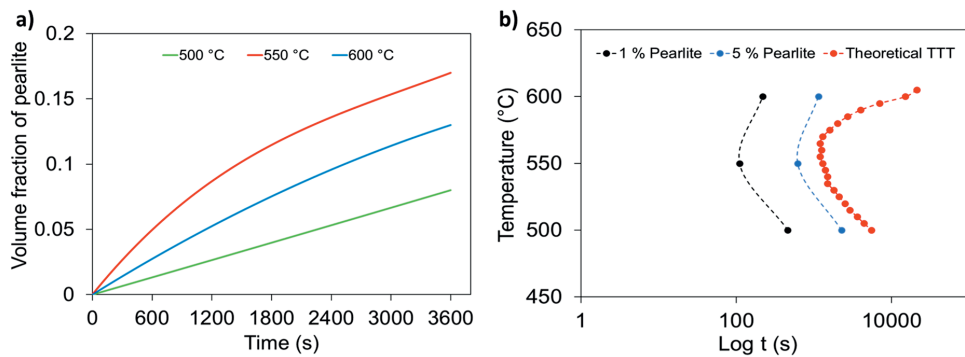


Figure 2.10. a) Volume fraction of pearlite formed during the isothermal holding at partitioning temperatures of 500 °C, 550 °C and 600 °C. b) TTT diagram showing partitioning times corresponding to 0.01 and 0.05 volume fraction of pearlite formation during partitioning at 500 °C, 550 °C and 600 °C. Figure b also shows theoretical TTT diagram calculated using MUCG83 program [28].

Based on the aforementioned analysis, the austenite stabilisation process might be enhanced during high-temperature partitioning provided the minimisation/suppression of competitive reactions. The formation of pearlite is pointed as the main process competing for the carbon available in the microstructure during the partitioning stage due to the large carbon contents and volume fractions of austenite that it consumes. To increase the fraction of retained austenite after the final quench, it is recommended to select relatively low quenching temperatures to create microstructures with a low volume fraction of untransformed austenite and small grain size which can 1) stabilise a high volume fraction of austenite during the final quench due to sufficient carbon enrichment [36], 2) avoid pearlite formation when isothermal holding is restricted to short times. Carbide precipitation inside austenite is occurring in the initial stage of partitioning and seems to be unavoidable. However, an alloy with low carbon content (lower than that

in the current work) might aid in delaying or suppressing carbide precipitation inside austenite by avoiding carbon super-saturation in austenite films.

2.6. Conclusions

This chapter investigates the evolution of the microstructure during Quenching & Partitioning processing in a medium manganese steel at partitioning temperatures between 400 °C – 600 °C and partitioning times up to 3600 s. The main conclusions extracted are:

- The major microstructural processes as result of carbon partitioning are that, partitioning of carbon at 400 °C leads to austenite stabilisation during the final quench, while carbon partitioning at 450 °C leads to carbide precipitation inside austenite grains. At even higher partitioning temperatures (500 °C – 600 °C) carbon partitioning also stimulates pearlite formation.
- Competitive phenomena such as carbide precipitation in austenite and pearlite formation negatively influence the austenite stability as they reduce the carbon available for partitioning during the partitioning stage.
- Carbon balancing at partitioning temperatures of 400 °C – 600 °C shows that almost no carbon is available in the primary martensite by the end of 3600 s of isothermal holding, indicating that neighbouring austenite grains are highly enriched in carbon. This enrichment results in carbide precipitation in austenite and pearlite formation depending on the morphology of the grain and partitioning conditions.
- For the current medium Mn steel, carbide precipitation in austenite and pearlite formation observed during the partitioning stage are occurring simultaneously. From the dilatometry curves, it can be deduced that carbide precipitation in austenite and pearlite formation are dominant in the early and later stages of the partitioning stage, respectively. The rate at which these phenomena occur is dependent on the partitioning temperature.
- In the present conditions, during isothermal holding at partitioning temperatures of 500 °C – 600 °C, volume fraction of pearlite can be restricted to 0.01 by employing holding times less than 100 s.

The scientific results of this chapter provide a better understanding of the microstructural changes occurring during high partitioning temperatures (450 °C - 600 °C) in medium Mn Q&P steels. It is understood that the suppression of the competitive reactions at high partitioning temperatures will help in optimising the austenite stabilising effect of carbon and manganese.

References

- [1]. D.V. Edmonds, K. He, M.K. Miller, F.C. Rizzo, A. Clarke, D.K. Matlock, J.G. Speer, **Microstructural Features of 'Quenching and Partitioning': A New Martensitic Steel Heat Treatment**. Materials Science Forum, 539-543 (2007), pp. 4819-4825.
- [2]. M. Gouné, F. Danoix, S.Y.P. Allain, O. Bouaziz, **Unambiguous carbon partitioning from martensite to austenite in Fe-C-Ni alloys during quenching and partitioning**. Scripta Materialia, 68(12) (2013), pp. 1004-1007.
- [3]. F. HajyAkbar, J. Sietsma, G. Miyamoto, T. Furuhashi, M.J. Santofimia, **Interaction of carbon partitioning, carbide precipitation and bainite formation during the Q&P process in a low C steel**. Acta Materialia, 104 (2016), pp. 72-83.
- [4]. D. Raabe, S. Sandlöbes, J. Millán, D. Ponge, H. Assadi, M. Herbig, P.P. Choi, **Segregation engineering enables nanoscale martensite to austenite phase transformation at grain boundaries: A pathway to ductile martensite**. Acta Materialia, 61(16) (2013), pp. 6132-6152.
- [5]. M.J. Santofimia, L. Zhao, J. Sietsma, **Microstructural Evolution of a Low-Carbon Steel during Application of Quenching and Partitioning Heat Treatments after Partial Austenitisation**. Metallurgical and Materials Transactions A, 40(1) (2008), pp. 46-57.
- [6]. M.J. Santofimia, L. Zhao, I. Povstugar, P.P. Choi, D. Raabe, J. Sietsma, **Carbon redistribution in a quenched and partitioned steel analysed by atom probe tomography**, in Proc 3rd int symp steel sci (ISSS 2012), N.H. Furuhashi T, Ushioda K, Editor. 2012: Kyoto: The Iron and Steel Institute of Japan, pp. 155.
- [7]. D. De Knijf, M.J. Santofimia, H. Shi, V. Bliznuk, C. Föjer, R. Petrov, W. Xu, **In situ austenite-martensite interface mobility study during annealing**. Acta Materialia, 90 (2015), pp. 161-168.
- [8]. M. Gouné, S. Aoued, F. Danoix, G. Geandier, A.Q. Poulon, J.C. Hell, M. Soler, S.Y.P. Allain, **Alloying-element interactions with martensite/austenite interface during quenching and partitioning of a model Fe-C-Mn-Si alloy**, Scripta Materialia, 162 (2019), pp. 181-184.
- [9]. E.J. Seo, L. Cho, B.C. De Cooman, **Kinetics of the partitioning carbon and substitutional alloying elements during quenching and partitioning (Q&P) processing of medium Mn steel**, Acta Materialia, 107 (2016), pp. 354-365.
- [10]. Tschiyama, T. Inoue, J. Tobata, D. Akami, S. Takaki, **Microstructure and mechanical properties of a medium manganese steel treated with interrupted quenching and intercritical annealing**. Scripta Materialia, 122 (2016), pp. 36-39.
- [11]. Y. Toji, H. Matsuda, M. Herbig, P.P. Choi, D. Raabe, **Atomic-scale analysis of carbon partitioning between martensite and austenite by atom probe tomography and correlative transmission electron microscopy**, Acta Materialia, 65 (2014), pp. 215-228.
- [12]. R. Ding, Z. Dai, M. Huang, Z. Yang, C. Zhang, H. Chen, **Effect of pre-existed austenite on austenite reversion and mechanical behaviour of an Fe-0.2C-8Mn-2Al medium Mn steel**. Acta Materialia, 147 (2018), pp. 59-69.
- [13]. J. Ågren, **A revised expression for the diffusivity of carbon in binary Fe-C austenite**. Scripta Metallurgica, 20(11) (1986), pp. 1507-1510.
- [14]. H. Oikawa, **Review on lattice diffusion of substitutional impurities in iron. A summary report**. Technol. Rep. Tohoku Univ., 47(2) (1982), pp. 215-224.

- [15]. J.R. Yang, H.K.D.H. Bhadeshia, **Continuous Heating Transformation of Bainite to Austenite**, *Materials Science and Engineering*, A131 (1991), pp. 99- 113.
- [16]. D.V. Edmonds, K. He, F.C. Rizzo, B.C. De Cooman, D.K. Matlock, J.G. Speer, **Quenching and partitioning martensite—A novel steel heat treatment**. *Materials Science and Engineering: A*, 438–440 (2006), pp. 25-34.
- [17]. C.F. Jaczak, **Retained Austenite and Its Measurement by X-Ray Diffraction**, SAE International, 1980.
- [18]. D.J. Dyson, B. Holmes, **Effect of alloying additions on the lattice parameter of austenite**. *J. Iron Steel Inst.*, 208 (1970), pp. 469-474.
- [19]. N. van Dijk, A. Butt, L. Zhao, J. Sietsma, S. Offerman, J. Wright, S. van der Zwaag, **Thermal stability of retained austenite in TRIP steels studied by synchrotron X-ray diffraction during cooling**, *Acta Materialia*, 53(20) (2005), pp. 5439-5447.
- [20]. L. Zhao, N.H. Van Dijk, E. Brück, J. Sietsma, S. Van der Zwaag, **Magnetic and X-ray diffraction measurements for the determination of retained austenite in TRIP steels**, *Materials Science and Engineering: A*, 313(1) (2001), pp. 145-152.
- [21]. B.D. Cullity, C.D. Graham, **Introduction to Magnetic Materials**, 2nd edition, IEEE/Wiley, Hoboken, New Jersey (2009).
- [22]. A.W. El-Morsy, A. I. Z. Farahat, **Effect of Cr and Thermomechanical Processing on the Microstructure and Mechanical Properties of Advanced High Strength Steel**, *Journal of Engineering Materials and Technology*, 140 (2) (2017), pp. 021005.
- [23]. S. Yang, H.K.D.H. Bhadeshia, **Uncertainties in dilatometric determination of martensite start temperature**, *Materials Science and Technology*, 23 (2007), pp. 556-560.
- [24]. M.J. Santofimia, L. Zhao, J. Sietsma, **Volume Change Associated to Carbon Partitioning from Martensite to Austenite**, *Materials Science Forum*, 706-709 (2012), pp. 2290-2295.
- [25]. R. Kannan, Y. Wang, L. Li, **Identification of Inverse Bainite in Fe-0.84C-1Cr-1Mn Hypereutectoid Low Alloy Steel**, *Metallurgical and Materials Transactions A*, 48A (2017), pp. 948-952.
- [26]. M. Onink, C.M. Brakrnan, F.D. Tichelaar, E.J. Mittemeijer, S. van der Zwaag, **The lattice parameters of austenite and ferrite in Fe-C alloys as functions of carbon concentration and temperature**, *Scripta Metall. Mater*, 29 (1993), pp. 1011-1016.
- [27]. E.S. Rowland, S.R. Lyle, **The application of Ms points to case depth measurement**, *Trans. ASM*, 37 (1946), pp. 27-47.
- [28]. H.K.D.H. Bhadeshia, **A thermodynamic analysis of isothermal transformation diagrams**, *Metal Science*, 16 (1982), pp. 159-165.
- [29]. L. Cheng, A. Böttger, T.H. de Keijser, E.J. Mittemeijer, **The tempering of iron carbon martensite dilatometric and calorimetric analysis**, *Metallurgical Transactions A*, 19(10) (1988), pp. 2415-2426.
- [30]. C. Garcia de Andres, F.G. Caballero, C. Capdevila, L.F. Alvarez, **Application of dilatometric analysis to the study of solid–solid phase transformations in steels**, *Materials Characterization*, 48(1) (2002), pp. 101-111.

- [31]. S. Hartmann, H. Ruppertsberg, **Thermal expansion of cementite and thermoelastic stresses in white cast iron**, *Materials Science and Engineering: A*, 190(1) (1995), pp. 231-239.
- [32]. J. Hidalgo, C. Celada-Casero, M.J. Santofimia, **Fracture mechanisms and microstructure in a medium Mn quenching and partitioning steel exhibiting macrosegregation**. *Materials Science and Engineering: A*, 754 (2019), pp. 766-777.
- [33]. Sung-Joon Kim, Chang Gil Lee, Tae-Ho Lee, Chang-Seok Oh, **Effect of Cu, Cr and Ni on mechanical properties of 0.15 wt.% C TRIP-aided cold rolled steels**. *Scripta Materialia*, 48 (2003), pp. 539-544.
- [34]. Jirková, H., L. Kučerová, B. Mašek, **Effect of Quenching and Partitioning Temperatures in the Q-P Process on the Properties of AHSS with Various Amounts of Manganese and Silicon**. *Materials Science Forum*, 706-709 (2012), pp. 2734-2739.
- [35]. N. Zhu, Q. Wu, Y. He, X. Lu, L. Li, P. Hu, **Effect of Ni on the Stability of Retained Austenite and Mechanical Properties for TRIP Steels Containing Vanadium**. *Steel research international*, 85(2) (2014), pp. 143-154.
- [36]. C. Celada-Casero, J. Sietsma, M.J. Santofimia, **The role of the austenite grain size in the martensitic transformation in low carbon steels**. *Materials and Design*, (167) (2019), pp. 107625.

3

Impact of Si and Ni on Quenching and High-Temperature Partitioning processing in medium-Mn steels

Austenite stabilisation through carbon partitioning from martensite into austenite is an essential aspect of the quenching and partitioning (Q&P) process. Substitutional alloying elements are often included in the chemical composition of Q&P steels to control the microstructure development by inhibiting carbide precipitation (silicon) and to further stabilise austenite (manganese and nickel). However, these elements can interfere in the microstructure development, especially when high partitioning temperatures are considered. In this chapter, the microstructure development during the Q&P process of four low carbon medium manganese steels with varying contents of silicon and nickel are investigated. During partitioning at 400 °C, silicon hinders cementite precipitation in primary martensite thereby assisting carbon partitioning from martensite to austenite. During partitioning at temperatures of 500 °C and 600 °C, presence of nickel inhibits pearlite formation and promotes austenite reversion. It is observed that the stabilisation of austenite is significantly enhanced through the addition of nickel by slowing down the kinetics of competitive reactions during the partitioning stage. These results provide an understanding on the interplay between carbon, silicon and nickel during Q&P processing that will allow the development of new design strategies to tailor the microstructure of this family of alloys.

**This chapter is based on: S. Ayenampudi, C. Celada-Casero, Z. Arechabaleta, M. Arribas, A. Arlazarov, J. Sietsma, and M.J. Santofimia: Microstructural impact of Si and Ni during high temperature quenching and partitioning process in medium-Mn steels, accepted for publication in Metallurgical and Materials Transactions A.*

3.1. Introduction

Based on the microstructural evolution discussed in Chapter 2, it is observed that competitive reactions occurring during the partitioning stage of the Q&P process cannot be completely suppressed but can be minimised by controlling the partitioning temperature and time. It was both qualitatively and quantitatively observed that such competitive reactions hinder the partitioning of carbon from martensite to austenite. Moreover, the impact of manganese on austenite stability could not be exclusively studied due to such competitive reactions.

The literature review presented in Chapter 1 reports the significance of substitutional alloying elements, such as manganese, on the austenite stabilisation in the Q&P microstructures. Along with manganese, nickel is also observed to be a strong austenite stabiliser. In a recent study of Kim *et al.* [1], three medium carbon low manganese steels with different nickel contents (0 – 2 wt. %) were studied. It was reported that, with an increase in nickel content, the volume fraction and stability of retained austenite were enhanced. An enhancement in mechanical properties with increasing partitioning temperature was also reported. In their work, Rizzo *et al.* [2] studied four different steels with different carbon and nickel content, after partitioning at 400 °C for times up to 300 s. Resulting Q&P microstructures showed an increase in retained austenite fractions and an improvement in strength and ductility was reported with an increase in nickel content. Recent investigations [1-7] show that the composition of the steel, mainly substitutional alloying elements, plays a crucial role in the control of the microstructure and mechanical properties of Q&P steels.

Recently, Pierce *et al.* [8] studied the Q&P process in two 0.2C-1.5Mn-1.3Si steels with 1.5 wt. % chromium and nickel, respectively. It was observed that at short isothermal holding times, with increase in partitioning temperature from 350 °C to 500 °C, an increase in the fraction of retained austenite occurred. Moreover, it was also observed that a higher fraction austenite was stabilised in the alloy with chromium than in the alloy with nickel. Ding *et al.* [9], showed that, for the alloy 0.2C-7.8Mn-2.0Al (wt.%), partitioning at temperatures above A_{c1} (660 °C) can lead to austenite reverse transformation (ART) promoting manganese partitioning into the newly formed austenite. The above studies emphasise the advantages of employing high temperature partitioning cycles and the quantitative impact of substitutional alloying elements on retaining austenite in Q&P microstructures. However, the interactions of these alloying elements with respect to austenite stabilisation and their effects on the microstructure development during the Q&P process were seldom addressed in the previous works.

The goal of this chapter is to study the microstructure development of four low-carbon medium-manganese steels during the application of high-temperature Q&P treatments. The four alloys have different nickel and silicon contents in order to explore the individual and mutual impact of the substitutional alloying elements on the microstructure evolution during Q&P process. For this purpose, based on the observations from Chapter 2, a new set of Q&P heat treatments which can hinder/suppress the competitive reactions are designed.

3.2. Materials and Experimental Methods

Four low-carbon medium-manganese steels with varying nickel and silicon contents were investigated. Manganese and nickel were added to the composition to delay ferrite and bainite formation, during the partitioning stage, while silicon was added to suppress carbide formation. Moreover, the addition of substitutional alloying elements like manganese and nickel aid in increasing the thermal stability of austenite facilitating high temperature Q&P cycles. The compositions of the alloys are listed in Table 3.1 and are named as *Mn*, *MnSi*, *MnNi* and *MnSiNi*.

Table 3.1. Chemical composition (wt. %) of Q&P steels investigated in the current work.

Alloy	C	Mn	Si	Ni	Fe
<i>Mn</i>	0.19	6.0	-	-	Bal.
<i>MnSi</i>	0.19	5.8	1.4	-	Bal.
<i>MnNi</i>	0.19	6.0	-	2.1	Bal.
<i>MnSiNi</i>	0.19	5.7	1.4	1.6	Bal.

Initially, steel ingots weighing 15 kg were produced using vacuum induction melting furnace. The ingots were reheated to ~ 1250 °C and subsequently hot-rolled down to a final thickness of 4 mm. Specimens with dimensions $10 \times 4 \times 4$ mm³ were machined with the longer dimension parallel to the rolling direction and used for performing Q&P heat treatments in a Bähr 805 DIL A/D dilatometer. A type S thermocouple spot welded on the surface was used to monitor and control the temperature. A vacuum on the order of 10^{-4} mbar was used during heating and during isothermal segments, whereas helium was used as the coolant. The error in change in lengths from dilatometry was assumed as ± 0.01 %.

After the application of the heat treatments, the specimens were cut into half and the surface was prepared by grinding with P800, P1000, and P1200 abrasive papers and polishing with 6, 3 and 1 μ m diamond paste. The polished samples were characterised using a Bruker type D8-Advance diffractometer to measure the volume fraction (f_{RA}) and lattice parameter (a_γ) of retained austenite at room temperature. The diffraction angles covered during the measurements are in the range $40^\circ < 2\theta < 130^\circ$, with Co K α radiation (wavelength 0.179026 nm), where the (110) α , (200) α , (211) α , (220) α and the (111) γ , (200) γ , (220) γ , (311) γ peaks are covered. A 0.042° 2θ step size with a counting time per step of 3 s was used. Following the direct comparison method of austenite and martensite peaks suggested by Jatzcak [10], the retained austenite volume fractions and the corresponding uncertainties were calculated. To determine the carbon concentration of retained austenite from its lattice parameter, the equations proposed by Dyson and Holmes [11] and van Dijk *et al.* [12] are combined and adjusted to suit the steel compositions in the current work:

$$a_\gamma = 3.556 \text{ \AA} + (0.0453 \frac{\text{\AA}}{\text{wt.\%}}) \cdot x_C + (0.00095 \frac{\text{\AA}}{\text{wt.\%}}) \cdot x_{Mn} + (0.00157 \frac{\text{\AA}}{\text{wt.\%}}) \cdot x_{Si} + (0.0006 \frac{\text{\AA}}{\text{wt.\%}}) \cdot x_{Cr} - (0.0002 \frac{\text{\AA}}{\text{wt.\%}}) \cdot x_{Ni} \quad (3.1)$$

where x_i represents the concentration of the alloying element i in wt.%. The detection limit of the retained austenite fraction by X-ray diffraction is 0.01. If any partitioning of substitutional alloying elements from martensite into austenite has occurred, it is very local and its influence on the average chemical composition of austenite and, thus, on the austenite lattice parameter will be negligible. Hence, the nominal composition of the alloy and lattice parameter of retained austenite is used to calculate the carbon content of retained austenite from the lattice parameter.

Room temperature microstructural analysis of the samples was carried out using a JEOL JSM-6500F field emission gun scanning electron microscope (FEG-SEM) operating at 15 kV. As a pre-requisite for the microstructural analysis, the specimens are prepared following the same procedure as for X-ray diffraction measurements. The polished specimens are then etched with a 2 % Nital solution. For all steel samples the surface perpendicular to the rolling direction is analysed.

Room temperature magnetic measurements were performed on cubic specimens with an edge dimension of 2.0 mm using a 7307 vibrating sample magnetometer. A standard National Institute of Standards and Technology nickel specimen was used for the calibration. Magnetisation curves at room temperature were measured by a stepwise change in the applied magnetic field from +1.6 to -1.6 T. According to the method indicated by Zhao *et al.* [13] the volume fraction of martensite (f_m) in the quenched specimen is determined by comparing the saturation magnetisation values both on the pure Fe BCC specimen, which is 215 Am²/kg at room temperature [14], and on the specimen containing martensite that is to be measured. The uncertainty in the measurement of the magnetisation/volume fraction during the ex-situ experiments is around ± 0.6 A/m, or which results in an uncertainty in the austenite volume fraction of ± 0.003 .

3.3. Design of Heat Treatments

To design the Q&P heat treatments, initially, the Q&P process parameters such as austenitisation temperature and quenching temperature (T_Q), the A_{c1} and A_{c3} temperatures as well as the martensite formation kinetics during quenching to room temperature were measured. A specimen of each alloy was subjected to full austenitisation by heating to a temperature of 950 °C at 10 °C/s. After 120 s of isothermal holding, the sample was directly quenched to room temperature at a cooling rate of 30 °C/s. After the identification of A_{c1} and A_{c3} temperatures, new set of heat-treatments on all alloys with austenitisation temperatures of $A_{c3} + 50$ °C were performed to identify the martensite start temperature and the martensite formation kinetics during quenching to room temperature. Table 3.2 gives information about the transformation temperatures of all four alloys.

Figure 3.1a shows the relative change in length with temperature during the cooling stage of the as-quenched specimens of the four alloys. A quenching followed by reheating heat treatment was performed to characterise the expansion behaviour of the quenched microstructure of the alloys. As shown in Figure 3.1a, the volume fraction of martensite at room temperature and its evolution with

temperature (Figure 3.1b) was obtained considering the linear expansion of the FCC and BCC phases and applying lever rule on the respective dilatometry curves. According to the room temperature magnetometer measurements, the as-quenched samples of alloys *Mn*, *MnSi*, *MnNi* and *MnSiNi* comprise about 0.940, 0.930, 0.920 and 0.930 (± 0.003) fractions of martensite, respectively. These martensite fractions correspond to the final change in length observed at room temperature, as indicated for alloy *MnNi* in Figure 1a. Based on the data from Figure 3.1b, formation of a 0.75 volume fraction of martensite is selected as the quenching temperature (T_Q) in all the Q&P heat treatments performed in the current work. Selected quenching temperatures (T_Q) for all four alloys are presented in Table 3.2.

Table 3.2. Phase transformation temperatures and selected quenching temperatures leading to 0.75 volume fraction of martensite of all four alloys investigated in the current work.

Alloy	A_{c1} (± 5 °C)	A_{c3} (± 5 °C)	M_s (± 5 °C)	T_Q (± 5 °C)
<i>Mn</i>	700	780	285	150
<i>MnSi</i>	716	812	260	140
<i>MnNi</i>	680	745	262	110
<i>MnSiNi</i>	710	790	266	120

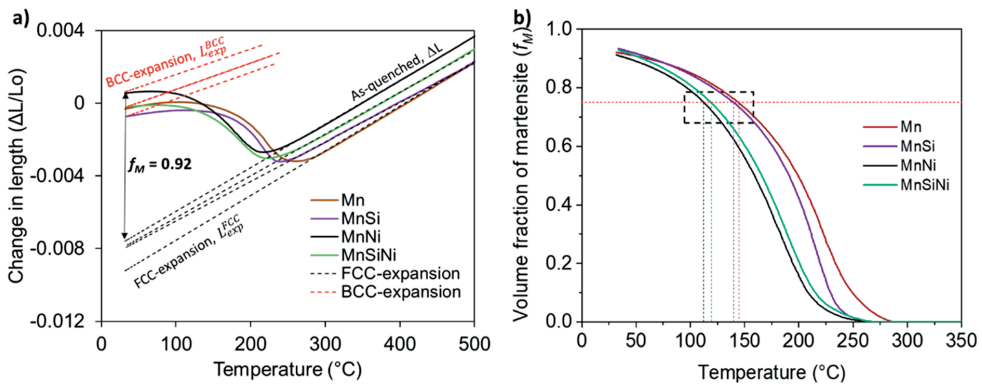


Figure 3.1. (a) Change in length versus temperature curve during quenching for alloys *Mn*, *MnSi*, *MnNi* and *MnSiNi*. In the same figure the fraction of martensite (f_M) formed in alloy *MnNi* at the end of as-quench heat treatment is shown. (b) Volume fraction of martensite as a function of temperature from the as-quench dilatation curve for alloys *Mn*, *MnSi*, *MnNi* and *MnSiNi* with indication of selected quench temperatures.

The four steels were Q&P processed as indicated in Figure 3.2. The specimens were heated to a temperature of $A_{c3} + 50$ °C and cooled down to a quenching temperature (T_Q) after 120 s of isothermal holding. At the T_Q the martensite/austenite microstructures are in the ratio 0.25/0.75. The theoretical optimum quenching temperature, calculated using constrained carbon equilibrium (CCE) model [15], for the four alloys corresponds to 0.70 - 0.80 volume fraction of primary martensite. However, for the comparison of different alloys it is important to have a similar volume fraction of primary martensite/austenite at the beginning of the partitioning stage. Hence, 0.75 volume fraction of primary martensite was selected. The initial quenching temperatures (T_Q) are different for all the four steel

compositions and are shown in Figure 3.1b and Table 3.2. Thereafter, the specimens were subjected to a partitioning stage, where partitioning temperature (T_p) of 400 °C, 500 °C and 600 °C were applied for partitioning times (t_p) up to 3600 s, 900 s and 300 s, respectively. The partitioning temperatures range from typical values aiming only for the austenite stabilisation through carbon partitioning (400 °C) to a temperature of 600 °C, which can promote austenite stabilisation through partitioning of substitutional alloying elements. In Chapter 2, the microstructure development in a Fe-0.31C-4.5Mn-1.5Si steel during Q&P processing in which the partitioning temperatures and times were in a range of 400 °C - 600 °C and 60 s - 3600 s, respectively was studied. It was observed that, during the partitioning at higher temperatures (500 °C – 600 °C), minimisation of competitive reactions like precipitation of carbides in austenite and formation of pearlite, is effective when the partitioning times are kept to less than 300 s. Hence, the heat treatments designed for these four alloys involve shorter partitioning times at higher partitioning temperatures. As a last step in the heat-treatment, the specimens were cooled down to room temperature at a cooling rate of 70 °C/s.

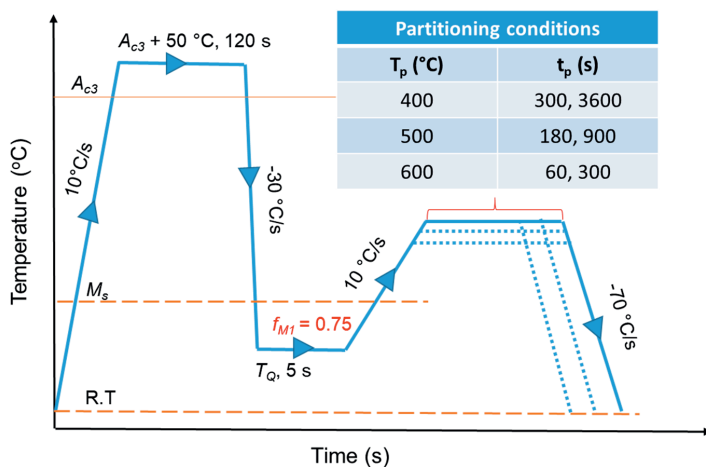


Figure 3.2. Schematic representation of Q&P thermal cycles applied on alloys *Mn*, *MnSi*, *MnNi* and *MnSiNi* in the present work.

3.4. Results

Phase Fractions and Carbon Content of Retained Austenite

Figure 3.3 shows the dilatation curve of the as-quenched specimen (black dashed line) and quenching and partitioning cycle of QP400-3600 condition (solid line) of alloy *MnNi*. The black solid lines indicate the FCC and BCC linear expansion lines obtained from the quenching + reheating heat treatment. The red dashed line indicates the BCC linear expansion line that is shifted to match the final quench in order to calculate volume fraction of fresh martensite. This figure is used to explain the manner in which the microstructural development is studied by dilatometry during Q&P processing routes. Evaluation of the QP400-3600 dilatometry curve in Figure 3.3 shows that the only phases forming during cooling from austenitisation are primary martensite (f_{M1}) during the initial quench and fresh martensite (f_{M2}) during

the final quench. Phenomena occurred during the partitioning stage are discussed in detail in the following sections.

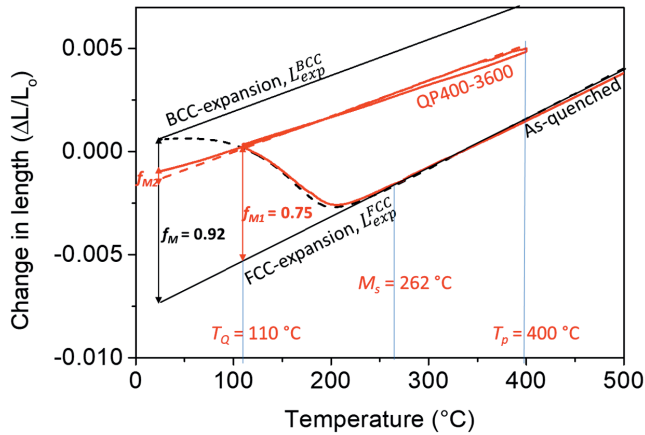


Figure 3.3. Representation of relative change in length versus temperature for an as-quench heat treatment (dashed line) and QP400-3600 heat treatment (solid line) of alloy *MnNi*. f_M is the fraction of martensite formed after an as-quench heat treatment; f_{M1} and f_{M2} are the fractions of primary and fresh martensite formed during QP400-3600 heat treatment respectively.

In all Q&P heat treatments, the volume fraction of primary martensite (f_{M1}) is kept the same, i.e. 0.75 ± 0.01 . Comparison of change in length measured during the final quench with that of the directly quenched specimen allows us to calculate the volume fraction of fresh martensite (f_{M2}). Since, fresh martensite formation occurs from a carbon enriched austenite, an average error of up to ± 0.01 in the evaluation of volume fraction of fresh martensite is estimated based on Ref [16]. X-ray diffractometer technique, was used to measure the volume fraction of retained austenite (f_{RA}) in the final microstructures. The volume fraction of rest of the final microstructural constituents, such as pearlite (f_p), was calculated by balancing phase fractions: $f_{M1} + f_{M2} + f_{RA} + f_p = 1$

The application of the above described method led to the results displayed in Figure 3.4, which shows the volume fraction of phases in the final Q&P microstructures of all the four alloys. In some cases, the total volume fraction of retained austenite and fresh martensite, in the end microstructure, has a deviation of up to ± 0.01 . This deviation is observed to be within the error of measurements and calculations. Hence, the effect is considered to be negligible.

Figure 3.4a shows the volume fractions of retained austenite (RA), fresh martensite (M2) and pearlite (P) in the final microstructure and carbon content in the retained austenite of all the four alloys after partitioning at 400 °C for 300 s and 3600 s. A slight increase in the volume fraction of retained austenite with partitioning time is observed in all the alloys except for alloy *Mn*. Alloys with nickel (*MnNi* and *MnSiNi*) show the highest fractions of retained austenite and lowest fractions of fresh martensite. Alloys with silicon show higher carbon content (wt. %) in retained austenite compared to that of alloys without silicon.

Figure 3.4b displays the volume fractions of the phases in the final Q&P microstructure of the four alloys after partitioning at 500 °C for 180 s and 900 s. With an increase in partitioning time, the volume fraction of fresh martensite increases. After 900 s of isothermal holding almost similar volume fraction of pearlite is observed in alloys *Mn*, *MnSi* and *MnSiNi*. With the increase in the volume fraction of pearlite, the carbon content and volume fraction of retained austenite decrease. The lowest and highest fraction of retained austenite is respectively detected in alloy *Mn*, after partitioning for 900 s, and in alloy *MnNi*, after partitioning for 180 s.

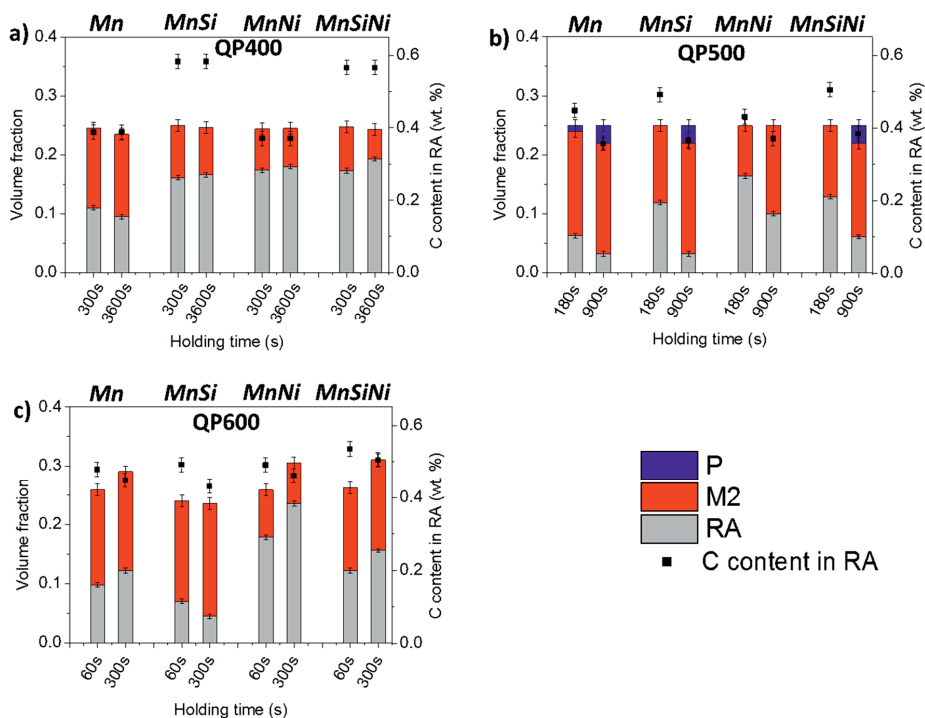


Figure 3.4. Representation of volume fraction of phases present at the end of a) QP400, b) QP500 and c) QP600 heat treatments as a function of the partitioning time for alloys *Mn*, *MnSi*, *MnNi* and *MnSiNi*. Carbon content of retained austenite after respective Q&P heat treatments is also represented in the same figure. P: Pearlite; M2: Fresh martensite; RA: Retained austenite.

Figure 3.4c shows the volume fractions of final microstructural constituents of all alloys after partitioning at 600 °C for 60 s and 300 s. Except for alloy *MnSi*, a clear increase of volume fraction of retained austenite with the partitioning time is observed. After 300 s of partitioning time at 600 °C, a volume fraction of retained austenite of around 0.24 was measured in the alloy *MnNi*. The total volume fraction of retained austenite, fresh martensite and pearlite exceeds the initial volume fraction of austenite at the beginning of the partitioning stage, which was 0.25. This indicates a reduction in the volume fraction of primary martensite during the partitioning step, which could be due to an austenite reverse transformation. In all the alloys, a decrease in carbon content (wt. %) in retained austenite is observed with partitioning time.

Microstructural Characterisation

The final microstructures of alloys *Mn*, *MnSi*, *MnNi* and *MnSiNi* after heat treatment QP400-3600 are shown in Figure 3.5a – 3.5d. Retained austenite films and fresh martensite/retained austenite islands (MA islands) are observed as the common microstructural features in all the four alloys. In alloys without silicon (alloys *Mn* and *MnNi*) a higher degree of carbide precipitation within primary martensite is observed. In addition, in alloy *Mn*, precipitation of carbides along the grain boundaries of prior austenite is observed. In alloys with silicon (*MnSi* and *MnSiNi*), primary martensite islands devoid of carbides are observed.

SEM micrographs (Figure 3.5e - 3.5h), of all the four alloys after partitioning at 500 °C for 900 s show the presence of MA islands and primary martensite with carbides as a common feature. The SEM micrograph of alloy *Mn* confirms the presence of pearlite along the grain boundaries of prior martensite/austenite, which is also observed in alloy *MnSi* and *MnSiNi*. A parallel array of carbides (indicated by dashed lines) aligned in certain directions is observed as a common microstructural feature in alloys with silicon (*MnSi* and *MnSiNi*). These arrays of precipitates are observed to be located in between primary martensite laths, which suggests that they form inside austenite films. In alloy *MnNi*, primary martensite is clearly enriched with carbides while retained austenite films present in between the martensite laths are observed.

The SEM micrographs of alloys *Mn*, *MnNi* and *MnSiNi*, Figure 3.5i, 3.5k, and 3.5l respectively, after QP600-300 heat treatments, show retained austenite films in-between the martensite laths. Moreover, retained austenite islands are observed in alloy *MnNi*. In alloy *MnSiNi*, carbide precipitation along grain boundaries of prior austenite is observed. Interestingly, SEM micrograph of alloy *MnSi* (Figure 3.5j), does not display evidence of significant amount of carbides inside primary martensite. However, precipitation of carbides inside austenite films is observed. Also, the micrograph of alloy *MnSi* suggest that prior austenite grains are much smaller than in the rest of the alloys. Since silicon increases the A_{c3} temperature but barely affects the A_{c1} temperature, the austenitisation range is much wider in alloys with silicon [17]. Hence, the treatment $A_{c3} + 50$ °C leads to a microstructure with a smaller prior austenite grain size in alloy *MnSi* when compared to the other alloys. Celada-Casero *et al.* [18] showed that the refined microstructure after the initial quench enhances the partitioning of carbon into austenite from martensite during partitioning stage. This can also explain the reason for sparse distribution of carbides in primary martensite in alloys with silicon.

Dilatometry

During the partitioning stage of QP400-3600 heat treatment an expansion in the initial 100 s of partitioning is observed (Figure 3.6a), which is an effect of carbon partitioning from primary martensite (M1) into austenite [19]. This expansion is followed by a contraction in the case of alloys without silicon (*Mn* and *MnNi*), which is attributed to carbide precipitation in primary martensite [20]. In the alloys with silicon (*MnSi* and *MnSiNi*) expansion is followed by a plateau indicating almost no carbide precipitation which is consistent with SEM observations (Figure 3.5b and 3.5d).

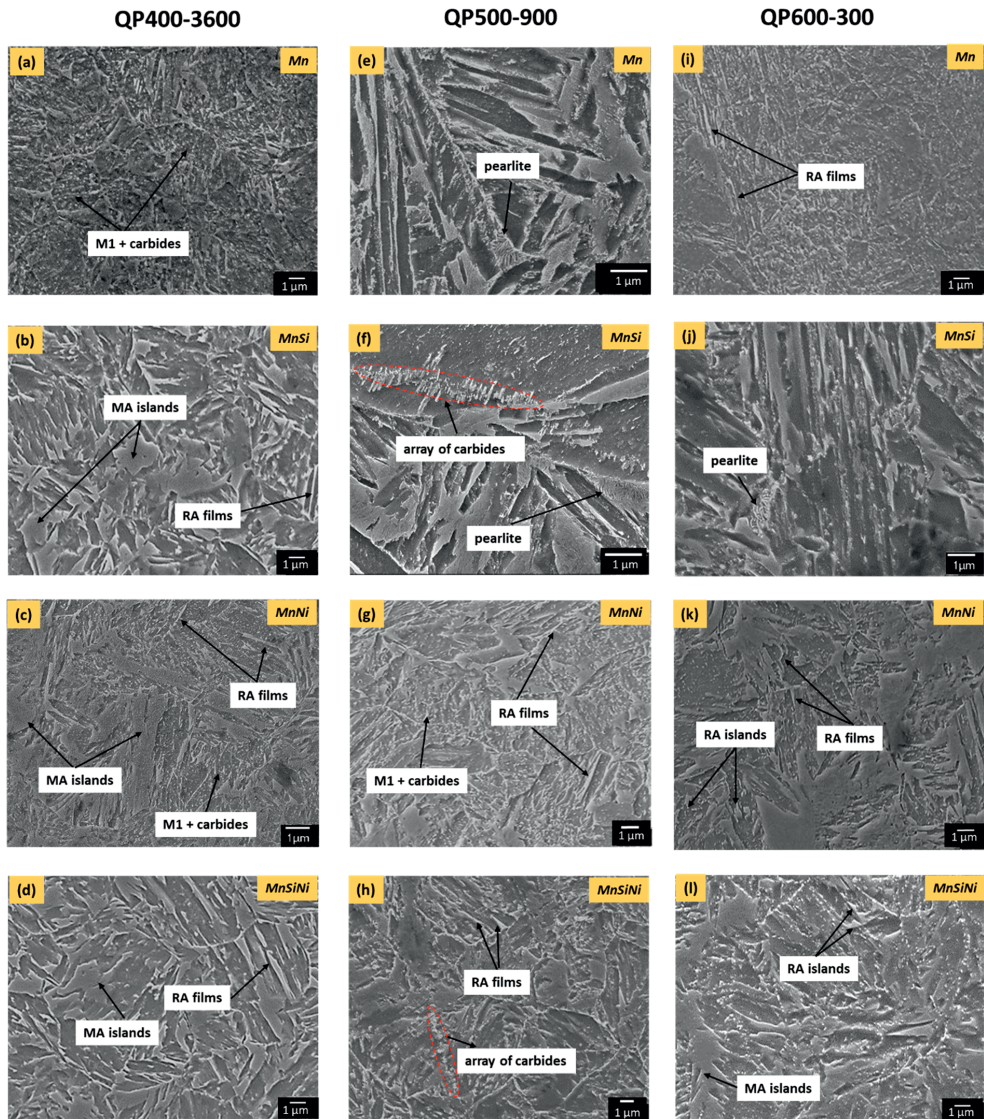


Figure 3.5. Figures from left to right show SEM micrographs of alloys *Mn*, *MnSi*, *MnNi* and *MnSiNi* after QP400-3600 (a-d), QP500-900 (e-h) and QP600-300 (i-l) heat treatments. M1: Primary martensite; MA: Martensite/Austenite islands; RA: retained austenite.

Figure 3.6b shows the change in length with time detected during partitioning at 500 °C for 900 s. The dilatometry curves of alloys without silicon (*Mn* and *MnNi*) show a small expansion for the first 50 s, indicating carbon partitioning. In the later part of the curve, alloy *Mn* shows a slight expansion, whereas alloy *MnNi* displays a slight contraction. Observations from the SEM micrographs (Figure 3.5e and 3.5g) suggest that the gradual expansion is related to pearlite formation and a slight contraction is related to carbide precipitation in primary martensite. Both alloys with silicon (*MnSi* and *MnSiNi*) exhibit a similar decrease in length followed by a plateau. Looking together with the SEM micrographs (Figure

3.5f and 3.5h) it is considered that this decrease can be a reaction to the formation of fine and parallel array of carbides. Based on experimental observations and the theoretical calculations of the change in length from Chapter 2 and Ref. [21], it can be said that cementite precipitation occurs in the carbon-supersaturated austenite and, consequently, the surrounding austenite is carbon-depleted. This process is accompanied with a contraction in length.

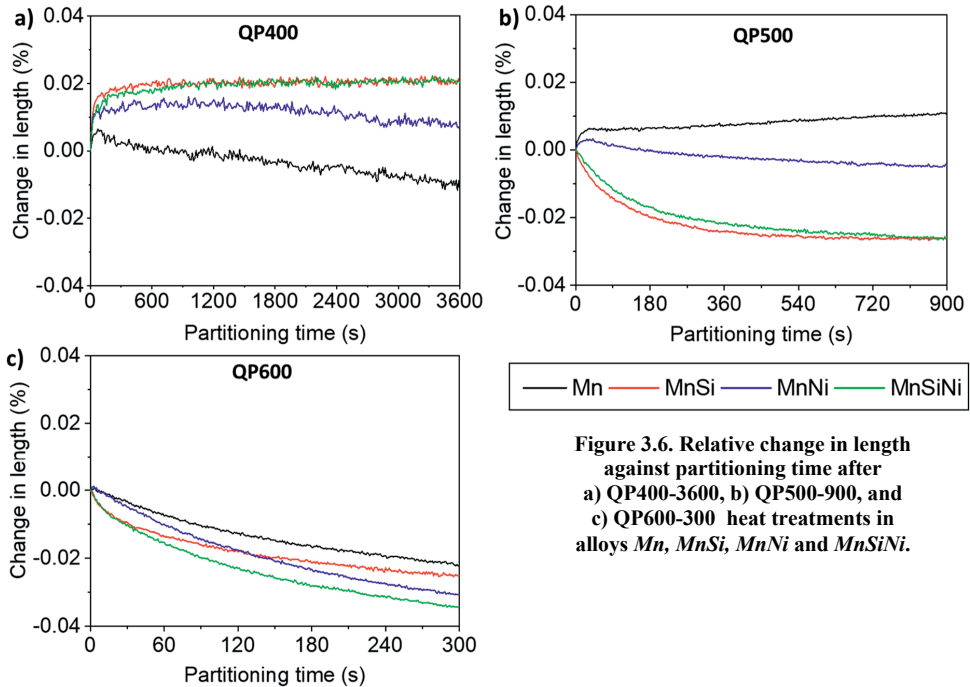


Figure 3.6. Relative change in length against partitioning time after a) QP400-3600, b) QP500-900, and c) QP600-300 heat treatments in alloys *Mn*, *MnSi*, *MnNi* and *MnSiNi*.

Dilatometry curves corresponding to the four alloys during partitioning at 600 °C for 300 s are shown in Figure 3.6c. All alloys show a continuous and strong contraction during partitioning. Usually, carbide precipitation or formation of austenite are related to a decrease in length of dilatometry samples. SEM micrographs of alloys *Mn*, *MnNi* and *MnSiNi* indicate no strong carbide precipitation but a dense distribution of retained austenite films/islands. Based on the observations of phase fractions and SEM micrographs, the contraction observed during partitioning at 600 °C can be related to austenite formation by austenite reverse transformation. In the case of alloy *MnSi*, the contraction rate slows down after 50 s and it is followed by a plateau indicating that the alloy *MnSi* exhibits the same behaviour as at 500 °C. It can be interpreted that this dilation behaviour is related to precipitation of carbides in austenite. The SEM micrograph also shows pearlite formation.

Estimation of austenite reversion

Analysis of phase fractions, SEM micrographs and dilatometry curves indicate austenite reversion in alloys *Mn*, *MnNi*, and *MnSiNi* during partitioning at 600 °C. In order to estimate the fraction of reverted austenite at 600 °C, a set of re-heating experiments were designed as shown in Figure 3.7. First,

microstructures consisting of 0.75/0.25 martensite/austenite fractions were created by full austenitisation and quenching to the initial quench temperature (T_Q), as in the earlier Q&P thermal routes shown in Figure 3.2. Thereafter, specimens were reheated to the respective austenitisation temperatures (heating 2) and quenched down to room temperature after isothermal holding for 120 s. The methodology to determine the austenite formation temperature during reheating and the estimation of austenite volume fraction formed during isothermal holding at 600 °C is explained below for alloy *Mn*.

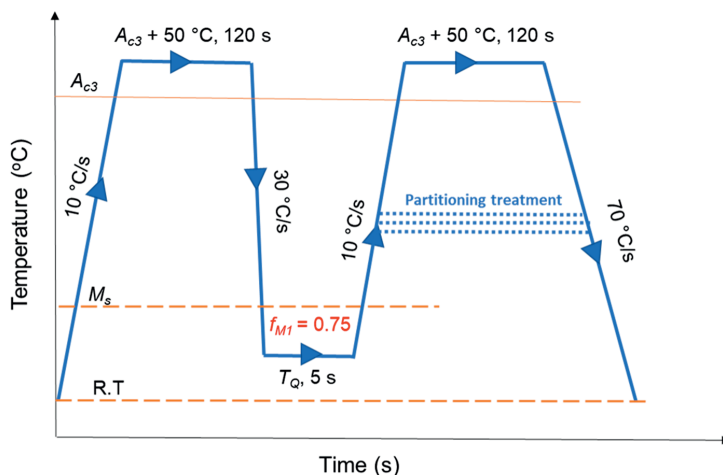


Figure 3.7. Quenching and re-heating cycles applied on all four alloys to determine austenite formation temperatures during reheating.

The relative change in length (solid line) and the first derivative of change in length with respect to temperature (dashed lines) during the quenching and re-heating heat treatment of all four alloys are shown in Figure 3.8a – 3.8d. The initiation of austenite formation during heating is indicated by a drop in the respective derivative curves (dashed lines). In all the alloys, austenite formation temperature during reheating is lower than the measured A_{c1} temperature. The reason for the onset of austenite reverse transformation at temperatures lower than A_{c1} is the presence of pre-existing austenite before the reheating. This can influence the subsequent austenite formation during the partitioning stage since it can grow more easily because no new nucleation is needed [22-23]. As seen from Figure 3.8, the austenite formation temperature during reheating cycle in all four alloys is around 605 °C, 650 °C, 580 °C, 610 °C \pm 5 °C, in alloys *Mn*, *MnSi*, *MnNi* and *MnSiNi*, respectively. Except for alloy *MnSi*, the rest of the alloys indicate austenite formation at temperatures very close to 600 °C. This also confirms that the behaviour of the dilatometry curves during partitioning at 600 °C (Figure 3.6c) in alloys *Mn*, *MnNi* and *MnSiNi* is related to austenite formation.

The volume fraction of austenite formed during the partitioning stage of QP600-300 heat treatment is calculated by comparing the change in length associated to its formation observed at 600 °C and the one derived from the complete BCC-to-FCC transformation. The relative change in length corresponding to complete austenite formation at 600 °C is extracted from the re-heating curve. It is to be noted that the

re-heating curve displays the transformation of only 0.75 volume fraction of BCC into FCC. From the comparison, the volume fraction of austenite formed after 300 s of partitioning at 600 °C is calculated to be around 0.04, 0.06 and 0.06 in alloys *Mn*, *MnNi* and *MnSiNi*, respectively. A discrepancy of 1-2 % can be expected due to the assumption that the kinetics of austenite formation during partitioning at 600 °C and reheating are considered to be the equivalent.

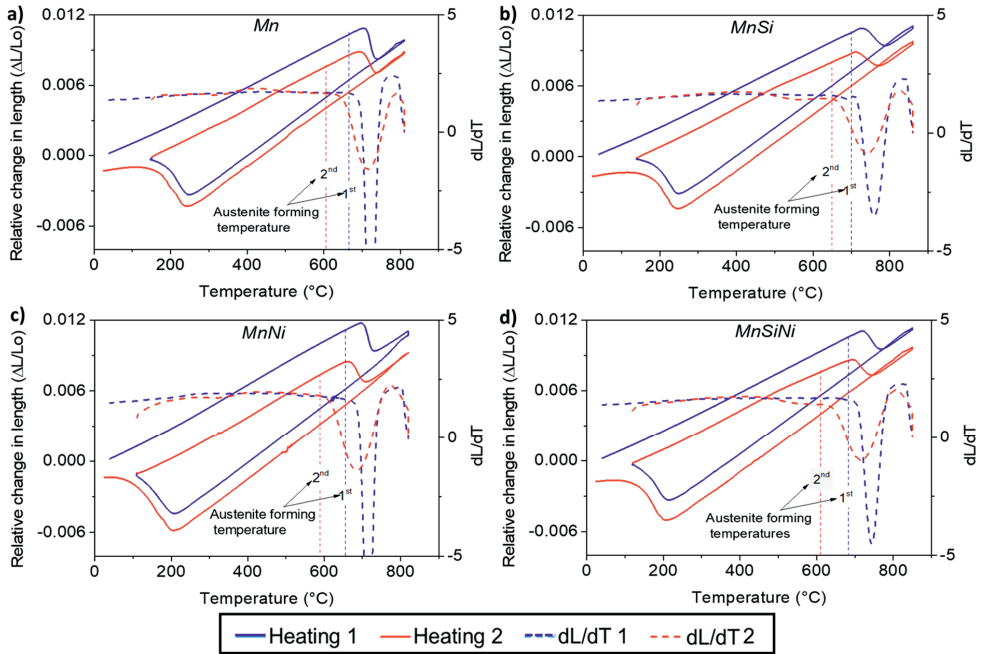


Figure 3.8. Change in length during quenching and reheating heat treatment (solid line) and respective derivative curves (dashed lines) showing temperatures of austenite formation during 1st and 2nd heating cycles in alloy a) *Mn* b) *MnSi* c) *MnNi* and d) *MnSiNi*.

3.5. Discussion

Table 3.3 shows the summary of the various phenomena observed during the partitioning stage of the respective Q&P treatments in all the four alloys. It is observed that with a change in the steel's composition, the microstructural events are either hindered or promoted. Hence, this section deals with understanding the influence of the alloying elements on the microstructural events during partitioning stage and on austenite stability.

3.5.1. Assessment of Carbon Partitioning

Carbon is a key alloying element in the stabilisation austenite at room temperature in the Q&P process. For this reason, in order to maximise the amount of carbon partitioned from martensite into austenite, it is of prime importance to inhibit the carbon consuming phenomena, like precipitation of carbides in primary martensite and austenite and pearlite formation during the partitioning stage.

Table 3.3. Summary of phenomena occurring during partitioning stage of QP400-3600, QP500-900 and QP600-300 heat treatments in the four alloys.

Heat treatment	Alloy	Phenomenon			
		Carbide precipitation in primary martensite	Carbide precipitation in austenite	Pearlite	Austenite reverse transformation
QP400-3600	Mn	✓	-	-	-
	MnSi	✓	-	-	-
	MnNi	✓	-	-	-
	MnSiNi	✓	-	-	-
QP500-900	Mn	✓	-	✓	-
	MnSi	✓	✓	✓	-
	MnNi	✓	-	-	-
	MnSiNi	✓	✓	✓	-
QP600-300	Mn	✓	-	-	✓
	MnSi	✓	✓	✓	-
	MnNi	✓	-	-	✓
	MnSiNi	✓	-	-	✓

In order to assess the fraction of carbon partitioned from martensite to austenite during the partitioning stage of Q&P heat treatments the following carbon balance is considered:

$$f_Y \cdot x_C^Y(t_p) = f_{RA} \cdot x_C^{RA}(t_p) + f_{M2} \cdot x_C^{M2}(t_p) \quad (3.2)$$

where f_Y, f_{M2}, f_{RA} and $x_C^Y, x_C^{M2}, x_C^{RA}$ are the volume fractions and carbon contents of austenite at the end of partitioning stage, fresh martensite and retained austenite, respectively, and t_p is the partitioning time. It implies that the carbon content present in the austenite at the end of the partitioning process is a summation of the carbon content of retained austenite and the secondary martensite at the end of the heat treatment. f_{RA} and f_{M2} are measured by X-ray diffraction and dilatometry, respectively, and x_C^{RA} is measured from the lattice parameter as explained in Chapter 2. The carbon content in austenite (x_C^Y), by the end of partitioning stage, is calculated by assuming two extreme cases. That is, assuming that the carbon content of fresh martensite (x_C^{M2}) is: 1) similar to that of retained austenite – upper limit, and 2) similar to that of nominal composition (0.19 wt.%) of the material, which implies absence of carbon partitioning in the austenite regions that became M2 on quenching - lower limit. The precise amount of carbon in fresh martensite will be in between these upper and lower limits.

Figure 3.9a, 3.9b and 3.9c show the range of total enrichment of carbon in the austenite at the end of partitioning stage of QP400-3600, QP500-900 and QP600-300 heat treatment, respectively. Note that the word “total” in this context indicate the product of the local carbon concentration of austenite and the volume fraction of austenite. In Figure 3.9, the black dashed line, indicates the total carbon in

austenite at the beginning of partitioning step, calculated as the product of nominal carbon content (0.19 wt.%) and the initial fraction of austenite (0.25). The red dashed line indicates the carbon content of austenite at the end of partitioning step assuming complete carbon partitioning from martensite (depleted to an equilibrium carbon composition, 0.013 wt. %) into austenite at the end the partitioning step. As expected, the upper and lower limits for the total carbon in austenite at the end of the partitioning step lie in between the black and red lines.

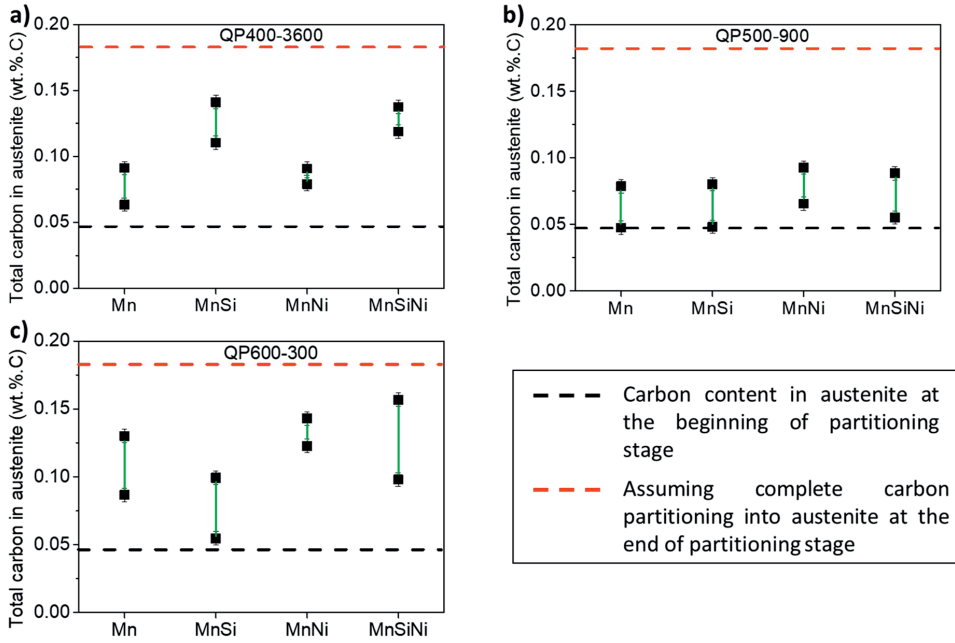


Figure 3.9. Upper and lower limits of total carbon present in austenite phase at the end of the partitioning step (black dots) in the four alloys. Note that these values represent the product of the local carbon concentration in austenite and the volume fraction of austenite. a) QP400-3600 b) QP500-900 and c) QP600-300.

The fraction of carbon remaining in primary martensite either in solid solution and/or carbides is estimated by carbon balancing.

$$\bar{x}(t_p) = f_\gamma \cdot x_c^\gamma(t_p) + f_{M1} \cdot x_c^{M1}(t_p) + f_p \cdot x_c^p(t_p) \quad (3.3)$$

where \bar{x} is the total fraction of carbon present in the alloy (0.19 wt. %), f_i and x_c^i represent the volume fraction and carbon content of phase i , being $i = \text{austenite } (\gamma)$, primary martensite (M1) and pearlite (P), at the end of isothermal holding. It should be noted that the fraction of carbon in M1 is the summation of carbon present in solid solution and the fraction of carbon in the form of carbides. Equation 3.3 is modified accordingly depending on the microstructural constituents present during partitioning at different temperatures, to evaluate the carbon remaining in primary martensite at the end of the isothermal holding at every partitioning temperature.

3.5.2. Interplay of Alloying Elements at Different Partitioning Temperatures

Partitioning at 400 °C

In alloys without silicon (*Mn* and *MnNi*) carbide precipitation is observed to be significant when compared to alloys with silicon (*MnSi* and *MnSiNi*), which can be due to carbide precipitation during the initial quench (auto-tempering) [24] or the partitioning stage [7]. In the work of [25], it is reported that silicon can retard cementite formation kinetics, but transitional carbides can still form in primary martensite. Hence, it is highly probable that the carbides observed in alloys *MnSi* and *MnSiNi* are transitional carbides. The equilibrium phase diagrams, calculated using ThermoCalc, show that, in alloys *Mn* and *MnNi*, cementite, ($M_{23}C_6$) and M_5C_2 type of carbides are expected to form. Since these are equilibrium phases, they do not dissolve with the increase in partitioning time. This is the reason why even after a partitioning time of 3600 s carbides are clearly evident in the respective SEM micrographs.

In alloys without silicon, formation of cementite or stable carbides reduce the fraction of carbon in solid solution in M1. Thus, a lower fraction of carbon is available to partition into the austenite phase during partitioning stage. Eventually, austenite at the end of partitioning stage in alloys *Mn* and *MnNi*, is enriched with lower carbon content (Figure 3.4a).

From Figure 3.9a, it is observed that in none of the alloys complete carbon partitioning from martensite to austenite has occurred (all points are below the red dashed line). This indicates that a significant fraction of carbon remains in the martensite either in solid solution or in the form of carbides, even in alloys with silicon (*MnSi* and *MnSiNi*), which showed negligible carbide precipitation (Figure 3.5b and 3.5d). Assuming full partitioning and using Equation (3.3), the total amount of carbon remaining in primary martensite is calculated to be around 0.05 wt. % C. HajjAkbari *et al.* [25] observed similar carbon contents in primary martensite from 3D-APT measurements in a 0.3C-1.6Si-3.5Mn (wt. %) steel after partitioning at 400 °C for 200 s. A reason for this could be that some of the carbon is trapped in the defects/dislocations of the primary martensite [26]. Moreover, due to their very small size, some transitional carbides formed during the initial quench may not be visible in the SEM micrographs [27]. These factors can be the reason for the presence of 0.05 wt. % carbon in primary martensite. In alloys without silicon, *Mn* and *MnNi*, in which significant carbide precipitation is observed, this fraction is around 0.09 and 0.10 wt.% C, respectively. Hence, it can be interpreted that in alloys *Mn* and *MnNi* at least 0.04 and 0.05 wt. % C of the total carbon is consumed by carbide precipitation in primary martensite during the partitioning stage, respectively. These calculations also suggest that there is more carbide precipitation in alloy *MnNi* than in alloy *Mn*.

Despite the presence of a significant fraction of carbides within primary martensite and less carbon enrichment of the austenite, a high fraction of austenite is retained in the alloy with nickel (*MnNi*). This can be explained by the austenite stabilising ability of nickel [22, 28-30]. Comparison of all four alloys show that the fraction of retained austenite after both 300 s and 3600 s of holding is in the order of $Mn < MnSi < MnNi < MnSiNi$. This also shows that, during the partitioning stage of QP400 heat

treatment, addition of either silicon or nickel helps in austenite stabilisation either by suppressing carbides formation or increasing the thermal stability of austenite, respectively. These mechanisms are kept active with the increase of the isothermal holding time. The combination of suppression of carbide precipitation due to the presence of silicon and the ability of nickel to increase thermal stability of austenite in alloy *MnSiNi* result in the retention of the largest fraction of austenite for the condition QP400.

Partitioning at 500 °C

In contrast to isothermal holding at 400 °C, a decrease in the fraction of retained austenite with an increase in partitioning time is observed in all the four alloys. In their recent work, Hidalgo *et al.* [31] showed carbon redistribution between martensite and austenite in a 0.31C-4.58Mn-1.5Si (wt. %) steel at a partitioning temperature of 500 °C, using DICTRA simulations. It is observed that, in less than 1 s, thin-film like austenite is enriched with 1.50 wt. % carbon. Hence, austenite grains are enriched with high fraction of carbon already at the very beginning of partitioning stage. In the present study, precipitation of carbides and/or the formation of pearlite in the already carbon enriched austenite is observed with the increase of holding time during partitioning 500 °C. These phenomena consume carbon thereby reducing the carbon available to homogenise in the rest of the austenite grains. Hence, during the final quench, the austenite that is deficient in carbon will transform into fresh martensite. This explains the decreasing trend of retained austenite volume fraction with an increase in isothermal holding time observed in all the four alloys.

However, in alloy *MnNi*, pearlite and carbides in austenite films are not observed. This is due to the absence of silicon in the material, which lead to a promotion of carbide precipitation in martensite in comparison with the other alloys. Moreover, the presence of nickel hinders pearlite formation by shifting the nose of pearlite to lower and much longer isothermal holding times [32].

Sections of the TTT diagrams of all the four alloys, Figure 3.10, corresponding to the ferrite/pearlite transformation fronts calculated using MAP_STEEL_MUCG83 [33], show that the partitioning temperature of 500 °C is close to the nose of pearlite in all alloys except for alloy *MnNi*. However, the predicted isothermal holding times are very far from the current experimental times. In order to investigate this a set of experiments were performed by cooling down a completely austenitic samples to 500 °C and isothermally holding for 1800 s. Interestingly, no pearlite formation was observed in neither of the alloys. This suggests that the presence of martensite assisted pearlite formation through rapid carbon enrichment of austenite promoted at this partitioning temperature. This also explains the reason for early pearlite formation than predicted by the model [53] during partitioning at 500 °C in the alloy studied in Chapter 2.

From the SEM micrographs of Q&P treated samples of alloys *Mn*, *MnSi* and *MnSiNi* (Figure 3.5e, 3.5f and 3.5h), it can be observed that pearlite formation is initiated along the grain boundaries of martensite and prior austenite. According to the classical nucleation theory, nucleation rate of carbides is high at

the regions where precipitation driving force is high and activation energy for carbide nucleation is low [34]. Both conditions are fulfilled at the martensite/austenite interfaces right after carbon partitioning. These interfaces are potential nucleation sites for carbide precipitation that initiate pearlite formation. It is calculated that around 0.02 – 0.03 wt.% of the total carbon is consumed by pearlite.

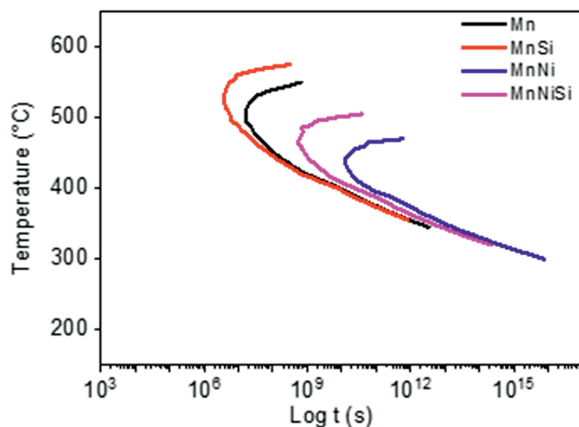


Figure 3.10. Section of the TTT diagram calculated using MAP_STEEL_MUCG83 showing the nose of ferrite/pearlite formation in alloys *Mn*, *MnSi*, *MnNi* and *MnNiSi*.

Figure 3.9b shows the maximum and minimum range of total carbon content partitioned into austenite during the partitioning stage of QP500-900 heat treatment. Based on Figure 3.9b and the above analysis, it can be interpreted that even considering maximum partitioning of carbon, around 0.08 – 0.09 wt.% of total carbon is left out in primary martensite of alloys *Mn*, *MnSi* and *MnSiNi*. Assuming that the 0.75 volume fraction of primary martensite has an equilibrium composition (0.013 wt. %), only 0.01 wt.% of total carbon is in the form of solid solution. The rest of the carbon is in the form of carbides in primary martensite. Hence, the carbon in primary martensite seems to be consumed by the carbides precipitated along the martensite/austenite interfaces that are evident from the SEM micrographs. It can be interpreted that, by the end of partitioning stage at 500 °C, competitive reactions like carbide precipitation in primary martensite and/or pearlite consumed most of the carbon.

Comparison of all four alloys show that the volume fraction of retained austenite at the end of both QP500-180 and QP500-900 heat treatments, follows the order $Mn < MnSi < MnSiNi < MnNi$ indicating that nickel has a positive impact on the thermal stability of retained austenite. Addition of silicon reduces the chances of carbide precipitation in martensite, leading to precipitation of carbides in austenite and pearlite formation during partitioning. These effects reduce the stabilising effect of manganese and nickel. In summary, suppression of silicon (to promote carbide precipitation in primary martensite instead of in austenite) and addition of nickel (to suppress pearlite formation) along with holding times lower than 180 s seems beneficiary to prevent competitive reactions during partitioning treatments at temperatures that are close to the pearlite nose in TTT diagrams.

Partitioning at 600 °C

In alloys *Mn*, *MnSi* and *MnSiNi*, no major competitive phenomenon are observed during the isothermal holding at 600 °C. Instead, an increase in retained austenite fraction with partitioning time is observed, which is due to austenite reverse transformation. From Figure 3.9c, it is observed that, the total amount of carbon accommodated by austenite is higher when compared to that at 400 °C and 500 °C, which is due to austenite reversion during the partitioning stage.

From the analysis in Section 3.4, it is drawn that, irrespectively of the different alloying elements, alloys *MnNi* and *MnSiNi* show similar volume fractions of newly formed austenite after partitioning at 600 °C for 300 s. To understand the influence of alloying elements on the kinetics of austenite reverse transformation at 600 °C, 1D simulations of carbon partitioning from martensite to austenite, in alloys *Mn*, *MnNi* and *MnSiNi* are carried out with DICTRA software [33] using TCFE8 and MobFe3 database. Earlier observations [34-36], showed that the martensitic lath widths are frequently found to be of the order of 0.2 μm . Hence, martensite and austenite lath sizes are defined to be of 200 nm and 66 nm, respectively. This corresponds to 0.75 and 0.25 volume fractions of martensite and austenite, respectively, representing the outset conditions of the partitioning stage of Q&P experiments. Because of the mirror boundary conditions in the calculation domain in DICTRA, only half thickness of the lath width is considered.

Figure 3.11 shows the kinetics of austenite reverse transformation (interface movement towards martensite) in alloys *Mn*, *MnNi* and *MnSiNi* calculated with DICTRA. For all the three alloys, the transformation starts at the very beginning of isothermal holding. In all the three alloys, at around 10^{-4} s, a shift from NPLE (negligible partitioning local equilibrium) to PLE (partitioning local equilibrium) mode of transformation [37] is observed. It can be observed that, the kinetics of austenite transformation is faster in alloys with nickel. Although alloy *MnNi* shows a relatively faster kinetics than alloy *MnSiNi*, after 300 s of partitioning time, the distance moved by the interface is similar in both alloys. Comparison between alloys *Mn* and *MnNi* shows that, while the addition of both manganese and nickel assists austenite growth, the austenite reverse kinetics are faster in the presence of nickel. Comparing alloys *MnNi* and *MnSiNi*, it is drawn that alloys without silicon exhibit a faster kinetics of austenite reversion during the early stages of isothermal holding. As silicon is a strong ferrite stabiliser, it retards austenite formation kinetics, which results in a sluggish austenite reversion at the beginning of isothermal holding in alloy *MnSiNi* [38].

Alloy *MnSiNi* displays a similar fraction of reverted austenite at the end of partitioning stage and a slightly higher carbon content of retained austenite when compared to alloy *MnNi*. Yet, the volume fraction of retained austenite is lower in the final microstructure of alloy *MnSiNi*. From Figure 3.12, it can be observed that the martensite start temperature of alloy *MnSiNi* is higher than that of alloy *MnNi*. This can be due to the fact that alloy *MnNi* contains a 0.5 wt. % Ni higher than alloy *MnSiNi*. Moreover, in the work of Wang *et al.* [39], based on phenomenological results, it was reported that, although silicon and manganese alone decrease the martensite start temperature (M_s), the interaction of silicon-

manganese has an increasing effect on the M_s temperature. However, further research is required to understand the impact of interaction of alloying elements on the M_s temperature.

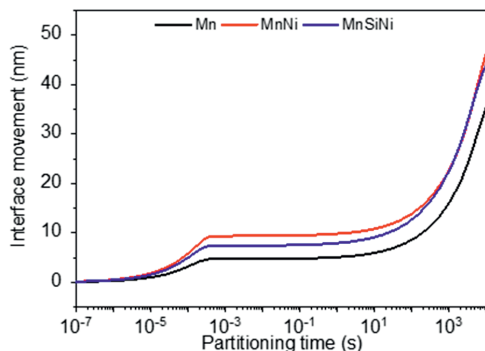


Figure 3.11. Austenite reversion kinetics in alloys *Mn*, *MnNi* and *MnSiNi* represented as interface position versus isothermal holding time at a partitioning temperature of 600 °C, calculated using DICTRA. Position “0” defines the location of the martensite/austenite interface at the beginning of the partitioning step and before austenite reversion starts.

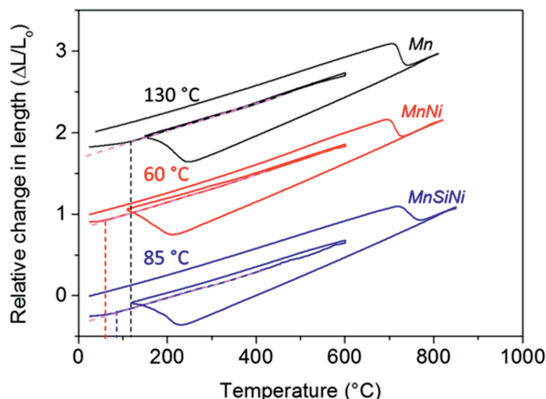


Figure 3.12. Dilatometry curves of alloys *Mn*, *MnNi* and *MnSiNi* indicating martensite start temperature ($M_s \pm 5$ °C) during the final quench of QP600-300 heat treatment.

Observations in alloys *Mn*, *MnNi* and *MnSiNi* show that the fraction of retained austenite rises with partitioning time while that of fresh martensite remains almost the same. This indicates that reverted austenite is more stable during the final quench than the pre-existing austenite. This could be explained considering the formation mechanism of reverted austenite, which involves local enrichment in manganese and nickel, as reported by Ding *et al.* [37]. Therefore, suppression of silicon and addition of nickel (alloy *MnNi*), along with holding times of up to 300 s at 600 °C, seem beneficiary for the stabilisation and maximisation of the retained austenite volume fraction in the final microstructure.

In summary, the interplay between the substitutional alloying elements manganese, silicon and nickel with carbon can influence either positively or negatively the Q&P microstructural development through changes in the carbon partitioning and stabilisation of austenite depending on the partitioning temperature. At conventional partitioning temperature (400 °C), alloys containing silicon promote

austenite stability significantly, which is even enhanced with the addition of nickel. At temperatures close to the nose of pearlite formation (500 °C), alloys with nickel and without silicon partitioned for shorter holding times (less than 180 s) are recommended to retain higher fractions of austenite. It seems that the austenite reverse transformation during the partitioning at 600 °C is beneficial and the reverted austenite can be more stable during the final quench than the sole carbon-enriched austenite. This also shows that partitioning temperatures above and below the nose of pearlite stabilise higher fractions of austenite, whereas the fraction of retained austenite increases with increasing partitioning time. The addition of nickel to a Q&P steel alloy is key in creating a controlled Q&P microstructure as it can assist in controlling major competing reactions, like precipitation of carbides inside austenite and pearlite formation, and in increasing thermal stability of austenite facilitating high temperature Q&P cycles.

3.6. Conclusions

Four different medium manganese steels were investigated to understand the impact of silicon and nickel on carbon partitioning, microstructural evolution and stability of retained austenite during quenching and partitioning processing at 400 °C, 500 °C and 600 °C for different times. The main conclusions drawn from this chapter are:

- After partitioning at 400 °C, 500 °C and 600 °C for up to 3600 s, a significant fraction of carbon does not diffuse into the austenite, but remains in the primary martensite either in solid solution or in the form of carbides.
- Partitioning at 400 °C: the presence of nickel decreases the carbon content required to retain austenite at room temperature, which results in higher fractions of retained austenite compared to alloys without nickel. The addition of silicon prevents cementite precipitation, making more carbon available for partitioning. Thus, in the presence of both nickel and silicon significant fractions of austenite are stabilised at room temperature.
- Partitioning at 500 °C: pearlite formation is prevented as the addition of nickel shifts the nose of pearlite to longer times. Also, the absence of silicon (*Mn* and *MnNi*) promotes carbide precipitation in primary martensite thereby avoiding super saturation of austenite grains during the isothermal holding, and contributing to the control of competitive reactions during the partitioning stage.
- Partitioning at 600 °C: the presence of nickel increases the austenite reversion kinetics, while silicon hinders it. In order to retain higher volume fraction of austenite, austenite reversion during partitioning seems to be beneficial as the reverted austenite during the final quench seems to be more stable than the pre-existing austenite.
- At all partitioning temperatures, except at 500 °C, an increase in partitioning time results in an increase in the volume fraction of retained austenite.

The results of this chapter provide an in-detail analysis of the impact of alloying elements on the microstructure evolution and austenite stability of medium manganese Q&P steels. Addition of nickel and adjustments of the Q&P cycles to promote the formation of reverted austenite are both potential strategies for the design of novel Q&P microstructures.

References

- [1]. K. Kim, and S.J. Lee, **Effect of Ni addition on the mechanical behaviour of quenching and partitioning (Q&P) steel**, *Materials Science and Engineering: A*, 698, (2017), pp. 183-190.
- [2]. F. Rizzo, A.R. Martins, J.G. Speer, D.K. Matlock, A. Clarke, B.C. De Cooman, **Quenching and partitioning of Ni-added high strength steels**, in *Materials Science Forum*, (2007), pp. 4476-4481.
- [3]. M.J. Santofimia, L. Zhao, I. Povstugar, P.P. Choi, D. Raabe, J. Sietsma, **Carbon redistribution in a quenched and partitioned steel analysed by atom probe tomography**, in *Proc. 3rd int. symp. steel sci. (ISSS 2012)*, N.H. Furuhashi T, Ushioda K, Editor : Kyoto: The Iron and Steel Institute of Japan, (2012), pp. 155.
- [4]. D. De Knijf, M.J. Santofimia, H. Shi, V. Bliznuk, C. Föjer, R. Petrov, W. Xu, **In situ austenite-martensite interface mobility study during annealing**, *Acta Materialia*, 90 (2015), pp. 161-168.
- [5]. M. Gouné, S. Aoued, F. Danoix, G. Geandier, A.P. Quintin, J.C. Hell, M. Soler, S.Y.P. Allain, **Alloying-element interactions with martensite/austenite interface during quenching and partitioning of a model Fe-C-Mn-Si alloy**, *Scripta Materialia*, 162, (2019), pp. 181-184.
- [6]. E.J. Seo, L. Cho, B.C. De Cooman, **Kinetics of the partitioning carbon and substitutional alloying elements during quenching and partitioning (Q&P) processing of medium Mn steel**, *Acta Materialia*, 107, (2016), pp. 354-365.
- [7]. Y. Toji, H. Matsuda, M. Herbig, P.P. Choi, D. Raabe, **Atomic-scale analysis of carbon partitioning between martensite and austenite by atom probe tomography and correlative transmission electron microscopy**, *Acta Materialia*, 65 (2014), pp. 215-228.
- [8]. D.T. Pierce, D.R. Coughlin, K.D. Clarke, E. De Moor, J. Poplawsky, D.L. Williamson, B. Mazumder, J.G. Speer, A. Hood, A.J. Clarke, **Microstructural evolution during quenching and partitioning of 0.2C-1.5Mn-1.3Si steels with Cr or Ni additions**, *Acta Materialia*, 151 (2018), pp. 454-469.
- [9]. R. Ding, Z. Dai, M. Huang, Z. Yang, C. Zhang, H. Chen, **Effect of pre-existed austenite on austenite reversion and mechanical behaviour of an Fe-0.2C-8Mn-2Al medium Mn steel**, *Acta Materialia*, 147 (2018), pp. 59-69.
- [10]. C.F. Jaczak, **Retained Austenite and Its Measurement by X-Ray Diffraction**, SAE International (1980).
- [11]. D.J. Dyson, B. Holmes, **Effect of alloying additions on the lattice parameter of austenite**, *J. Iron Steel Inst.*, 208 (1970), pp. 469-474.
- [12]. N. van Dijk, A. Butt, L. Zhao, J. Sietsma, S. Offerman, J. Wright, S. van der Zwaag, **Thermal stability of retained austenite in TRIP steels studied by synchrotron X-ray diffraction during cooling**, *Acta Materialia*, 53(20) (2005), pp. 5439-5447.

- [13]. L. Zhao, N.H. Van Dijk, E. Brück, J. Sietsma, S. Van der Zwaag, **Magnetic and X-ray diffraction measurements for the determination of retained austenite in TRIP steels**, *Materials Science and Engineering: A*, 313(1) (2001), pp. 145-152.
- [14]. B.D. Cullity, C.D. Graham, **Introduction to Magnetic Materials**, 2nd edition, IEEE/Wiley, Hoboken, New Jersey (2009).
- [15]. J.G. Speer, A.M. Streicher, D. Matlock, F. Rizzo, G. Krauss, **Quenching and partitioning: A fundamentally new process to create high strength trip sheet microstructures**, in *Materials Science and Technology Meeting*, Chicago, IL; United States, (2009).
- [16]. A. Koniger, C. Hammerl, M. Zeitler, B. Rauschenbach, **Formation of metastable iron carbide phases after high-fluence carbon ion implantation into iron at low temperatures**, *Physical review B*, 55 (13) (1997), pp. 8143-8147.
- [17]. H. Kim, J. Inoue, M. Okada, K. Nagata, **Prediction of A_{c3} and Martensite Start Temperatures by a Data-driven Model Selection Approach**, *ISIJ International*, 57 (12) (2017), pp. 2229-2236.
- [18]. C. Celada-Casero, C. Kwakernaak, J. Sietsma, M.J. Santofimia, **The influence of the austenite grain size on the microstructural development during quenching and partitioning processing of a low-carbon steel**, *Materials and Design*, 178 (2019), pp. 107847.
- [19]. M.J. Santofimia, L. Zhao, J. Sietsma, **Volume Change Associated to Carbon Partitioning from Martensite to Austenite**, *Materials Science Forum*, 706-709 (2012), pp. 2290-2295.
- [20]. Y. Toji, H. Matsuda, M. Herbig, P.P. Choi, D. Raabe, **Atomic-scale analysis of carbon partitioning between martensite and austenite by atom probe tomography and correlative transmission electron microscopy**, *Acta Materialia*, 65 (2014), pp. 215-228.
- [21]. R. Kannan, Y. Wang, L. Li, **Identification of Inverse Bainite in Fe-0.84C-1Cr-1Mn Hypereutectoid Low Alloy Steel**, *Metallurgical and Materials Transactions A*, 48A (2017), pp. 948-952.
- [22]. F. Rizzo, A.R. Martins, J.G. Speer, D.K. Matlock, A. Clarke, B.C. De Cooman, **Quenching and partitioning of Ni-added high strength steels**, in *Materials Science Forum*, (2007), pp. 4476-4481.
- [23]. R. Wei, M. Enomoto, R. Hadian, H.S. Zurob, G.R. Purdy, **Growth of austenite from as-quenched martensite during intercritical annealing in an Fe-0.1C-3Mn-1.5Si alloy**, *Acta Materialia*, 61(2) (2013), pp. 697-707.
- [24]. F. HajyAkbari, J. Sietsma, G. Miyamoto, T. Furuhashi, M.J. Santofimia, **Interaction of carbon partitioning, carbide precipitation and bainite formation during the Q&P process in a low C steel**, *Acta Materialia*, 104 (2016), pp. 72-83.
- [25]. F. HajyAkbari, J. Sietsma, G. Miyamoto, N. Kamikawa, R.H. Petrov, T. Furuhashi and M.J. Santofimia, **Analysis of the mechanical behaviour of a 0.3C-1.6Si-3.5Mn (wt. %) quenching and partitioning steel**, *Materials Science and Engineering: A*, 677 (2016), pp. 505-514.
- [26]. G. Krauss and A.R. Marder, **The morphology of martensite in iron alloys**, *Metallurgical Transactions*, 2 (1971), pp. 2343-2357.

- [27]. A. Koniger, C. Hammerl, M. Zeitler, B. Rauschenbach, **Formation of metastable iron carbide phases after high-fluence carbon ion implantation into iron at low temperatures**, Physical review B, 55 (13) (1997), pp. 8143-8147.
- [28]. S.J. Kim, C.G. Lee, T.H. Lee, C.S. Oh, **Effect of Cu, Cr and Ni on mechanical properties of 0.15 wt.% C TRIP-aided cold rolled steels**, Scripta Materialia, 48 (2003), pp. 539-544.
- [29]. N. Zhu, Q. Wu, Y. He, X. Lu, L. Li, P. Hu, **Effect of Ni on the Stability of Retained Austenite and Mechanical Properties for TRIP Steels Containing Vanadium**, Steel research international, 85(2) (2014), pp. 143-154.
- [30]. C. Capdevila, F.G. Caballero, C.G.D. Andrés, **Determination of M_s Temperature in Steels: A Bayesian Neural Network Model**, ISIJ International, 42(8) (2002), pp. 894-902.
- [31]. J. Hidalgo, C. Celada-Casero, M.J. Santofimia, **Fracture mechanisms and microstructure in a medium Mn quenching and partitioning steel exhibiting macro-segregation**, Materials Science and Engineering: A, 754 (2019), pp. 766-777.
- [32]. T. Sourmail, H.K.D.H. Bhadeshia, **Modelling simultaneous precipitation reactions in austenitic stainless steels**, Calphad, 27 (2003), pp. 169-175.
- [33]. A. Borgenstam, L. Hoglund, J. Agren, A. Engstrom, **DICTRA, a tool for simulation of diffusional transformations in alloys**, J. Phase Equilibria, 21 (2000), pp. 269.
- [34]. C.A. Apple, R.N. Caron, G. Krauss, **Packet microstructure in Fe-0.2 pct C martensite**, Metallurgical Transactions A, 5 (1974), pp. 593-599.
- [35]. T. Swarr, G. Krauss, **The effect of structure on the deformation of as-quenched and tempered martensite in an Fe-0.2 pct C alloy**, Metallurgical Transactions A, 7A (1976), pp. 41-48.
- [36]. A.R. Marder, **The morphology and strength of iron-carbon martensite**, Ph.D. Thesis, Lehigh University (1968).
- [37]. R. Ding, D. Tang, A. Zhao, **A novel design to enhance the amount of retained austenite and mechanical properties in low-alloyed steel**. Scripta Materialia, 88 (2014), pp. 21-24.
- [38]. Z.D. Li, G. Miyamoto, Z.G. Yang, T. Furuhashi, **Kinetics of reverse transformation from pearlite to austenite in an Fe0.6C alloy and the effects of alloying elements**, Metallurgical and Materials Transactions A, 42A (2011), pp. 1586-1596.
- [39]. J. Wang, P.J. van der Wolk, S. van der Zwaag, **Determination of martensite start temperature in engineering steels part 1. Empirical relations describing the effect of steel chemistry**, Materials Transactions, 41 (7) (2000), pp. 761-768.

4

3D Atom Probe Tomography and Phase-Field Modelling Investigation of Interface Migration and Elemental Partitioning during Quenching and High-Temperature Partitioning Process

The microstructural development during Q&P heat treatments is strongly linked to the process of carbon partitioning from martensite to austenite. Simultaneous to carbon partitioning, the partitioning of substitutional alloying elements was observed in the literature. However, the conditions at which this phenomenon occurs and its significance in the microstructure development are not well understood. This work investigates the partitioning kinetics of carbon and manganese in a Fe-0.19C-6Mn (wt.%) steel by combining multi-phase field modelling and 3D atom probe tomography experiments. The redistribution of carbon and manganese between martensite and austenite is studied at partitioning temperatures of 400 °C, 500 °C and 600 °C for times up to 3600 s. Observations from 2D simulations show that multiple austenite grains compete for the carbon from the same martensite grain lying in between, thus resulting in the development of asymmetric carbon concentration profiles at the α/γ interfaces of the same austenite grain. This leads to continuous carbon redistribution among the austenite grains through the martensite grains. 1D simulations show that apart from concentration gradients the austenite and martensite grain sizes, along with surrounding microstructure, also play a crucial role in the extent of α/γ interface movement. It is observed that the smaller the austenite grain size, the faster the equilibration of alloying elements at the α/γ interface is, which results in less α/γ interface migration when compared to bigger grains. Experimental and simulation results show that interface migration and manganese partitioning are simultaneous phenomena during partitioning at 600 °C for 300 s. The α/γ interface migration due to the austenite reversion assists in enriching the newly formed austenite grains with manganese, which can be a strategy to stabilise higher volume fractions of austenite in the final Q&P microstructure.

**This chapter is based on: S. Ayenampudi, C. Celada-Casero, J. Sietsma, and M. J. Santofimia, 3D atom probe tomography and phase-field modelling investigation of interface migration and elemental partitioning during quenching and partitioning process. To be submitted for publication.*

4.1. Introduction

The outcomes from Chapter 3 indicate that the addition of nickel and/or the formation of reverted austenite during the partitioning stage are both potential strategies to stabilise higher fractions of retained austenite in the final microstructure. Although nickel is a very strong austenite stabilizing element, the addition of nickel to an alloy makes it relatively expensive, which actually derails the purpose of the third generation of AHSS grades. Understanding the reasons behind why the reverted austenite is more stable than the pre-existing austenite could help in designing a Q&P steel with minimised addition of substitutional alloying elements and develop effective Q&P processes.

The stabilisation of austenite at room temperature is the main goal of the Q&P process, and it is primarily achieved through the partitioning of carbon from martensite to austenite. Speer *et al.* [1] proposed a thermodynamic model called Constrained Carbon Equilibrium (CCE), based on two assumptions, to define the end of an ideal carbon partitioning process at a given temperature: I) equal chemical potential of carbon in both martensite and austenite and; II) martensite/austenite (α/γ) interface is immobile. The typical partitioning temperatures at which this model is valid is limited to approximately 400 °C, where the diffusivity of substitutional alloying elements is slow, relative to carbon. Therefore, partitioning of substitutional alloying elements is neglected in the CCE model. However, recent investigations by 3D-Atom Probe Tomography (APT) show that partitioning at 400 °C and 450 °C can also lead to nanoscale manganese enrichment in austenite grains, next to the martensite/austenite interfaces, over a range of less than 5 nm [2-7]. With such observations the curiosity to understand the behaviour of manganese and the possibility of α/γ interface migration during the partitioning stage has led to further research.

Taking the advantage of advanced characterisation techniques, efforts have been put to experimentally observe interfacial migration and partitioning of substitutional alloying elements across the different interfaces in medium Mn steels [8-11]. Recent experimental evidence from in-situ transmission electron microscopy (TEM) analysis [12] in-situ high energy X-ray diffraction [13-14] and in-situ neutron diffraction [15], show an increase in austenite fraction during the partitioning stage of the Q&P process. This indicates that the α/γ interface movement (growth of austenite) occurs during the partitioning stage under some conditions. Along with the α/γ interface movement, some of the studies observed manganese enrichment in the austenite films. In their investigation, Ding *et al.* [16] reported austenite reversion during the partitioning stage at 660 °C for 1 h in a 0.20C-7.76Mn-1.99Al (wt.%) steel, as well as enrichment of manganese only in the reverted austenite. However, no conclusive interpretation about the mechanism behind α/γ interface movement or manganese enrichment in austenite was made.

Apart from experimental observations, theoretical studies also reported partitioning of substitutional alloying elements and martensite/austenite (α/γ) interface movement, during the partitioning stage of the Q&P process [17-20]. Nanoscale interfacial partitioning of substitutional alloying elements across (bainitic)-ferrite/austenite interfaces in TRIP steels were also reported [21-23]. Very recently, Dai *et al.*

[24], experimentally and theoretically studied the α/γ interface movement dependency on partitioning temperature, by assuming para-equilibrium and local-equilibrium conditions, in an FeCMnSi steel. A common observation from all these theoretical studies is that interfacial partitioning of substitutional elements could play a significant role in the kinetics of interface migration. However, the inter-related mechanism between partitioning and α/γ interface migration during the Q&P process is not yet concrete. Elucidating this mechanism helps the effective design of Q&P thermal cycles and aids in taking advantage of the stabilising effect of substitutional alloying elements on austenite.

The focus of the present chapter is to understand the behaviour of carbon and manganese and their role in the α/γ interface migration, in a Fe-0.19C-6.0Mn (wt. %) steel, during the partitioning stage of the Q&P process. The effect of grain morphologies and grain sizes on the evolution of carbon and manganese profiles during the partitioning stage is also investigated. Multi-phase field simulations and 3D-APT experiments are performed to describe the partitioning kinetics of alloying elements (carbon and manganese) at partitioning temperatures between 400 °C and 600 °C for times up to 3600 s.

4.2. Experimental Methods

4.2.1. Material and Microstructure Development

In this chapter, the Q&P heat treated QP600-300 sample of the alloy *Mn*, from Chapter 3, is further investigated. The reason for selecting this specimen for further investigation is that the partitioning mechanism of manganese and the α/γ interfacial migration mechanism can be solely studied due to the absence of major competitive reactions during the partitioning stage. This helps us to understand the partitioning mechanism. The chemical composition of the alloy is Fe-0.19C-6.0Mn (wt. %). The Q&P heat treatment of this steel involved a complete austenitisation by heating to 830 °C and isothermal holding for 120 s. By quenching to a temperature of 150 °C, the formation of 0.75 volume fraction of martensite was induced. Specimens were then subjected to a partitioning stage, where partitioning temperatures (T_p) of 400 °C, 500 °C, and 600 °C were applied for a duration (t_p) of 3600 s, 900 s, and 300 s, respectively. The microstructural development of the investigated steel during these Q&P thermal cycles were extensively discussed in Chapter 3 and are summarised here. During partitioning at 400 °C and 500 °C, carbide precipitation in martensite and pearlite formation competed for the carbon available for partitioning from martensite to austenite. During partitioning at 600 °C, austenite formation was observed: around 0.04 ± 0.01 martensite is transformed into austenite (austenite reverse transformation) after 300 s of isothermal holding. In this case, the final Q&P microstructure consisted of 0.71, 0.12 and 0.17 volume fractions of primary martensite (M1), retained austenite (RA) and fresh martensite (M2), respectively. The above experimental data related to microstructure development is used as a reference for the phase-field simulations.

4.2.2.3D Atom Probe Tomography

3D Atom Probe Tomography (APT) is used for the atomic-scale quantitative investigation of the elemental partitioning in the final Q&P microstructure of the specimen partitioned at 600 °C for 300 s. This condition is selected to perform 3D APT experiments as no signs of competitive reactions that involve carbon were observed during the partitioning stage. This could be an optimum condition for validation of the predictions by phase-field modelling on manganese partitioning. The 3D APT specimen was prepared by the focussed-ion beam (FIB) milling and lift-out technique [25] in a FEI Helios Nanolab 650. APT analysis was carried out using a laser-assisted atom probe (CAMECA-LEAP 5000). The specimen was analysed at 60 K by applying laser pulses of 355 nm wavelength with 250 kHz pulse energy and an energy of 45 pJ. Data reconstruction and analysis was performed using the IVAS® software.

4.3. Model

4.3.1. Description of Phase-Field Model

The multi-phase field approach proposed by Steinbach *et al.* [26] and extended by Eiken *et al.* [27] is employed. In the multi-phase field method, each grain i is identified by its phase-field parameter ϕ_i which varies with time (t) and space (\vec{r}). If the phase field parameter of grain i , $\phi_i(\vec{r}, t)$, is zero, the grain is not present at (\vec{r}, t) , if $\phi_i(\vec{r}, t) = 1$ it is present. At each point in the microstructure the sum of the phase-field parameters of all grains equals one. To each grain a specific lattice structure is attributed, BCC for ferrite (α) and martensite (α') and FCC for austenite (γ). The transition of the phase-field parameter between 0 and 1 occurs within a certain width between two grains which is defined as a diffuse interface. Within the diffuse interface, between BCC and FCC grains, both phases co-exist in a certain ratio, determined by the local values of the phase-field parameters of the two grains. Inside the interface, the region in which ferrite is dominant compared to austenite will be termed as ‘ferrite-dominant region’ and the interface region in which austenite is dominant will be termed as a ‘austenite-dominant region’. Hence, diffusion of elements occurring inside interface can still be considered as partial partitioning. The motion of interfaces during phase transformations can be described by the change of the phase field parameter with time as:

$$\frac{d\phi_i}{dt} = \sum_{i \neq j} M_{ij} \left\{ \sigma_{ij} \left[\phi_j \nabla^2 \phi_i - \phi_i \nabla^2 \phi_j + \frac{\pi^2}{2\eta_{ij}^2} (\phi_i - \phi_j) \right] + \frac{\pi}{\eta_{ij}} \sqrt{\phi_i \phi_j} \Delta G_{ij} \right\} \quad (4.1)$$

where M_{ij} is the interface mobility, σ_{ij} is the interfacial energy, η_{ij} is the interface thickness and ΔG_{ij} is the driving force for transformation which is a function of temperature (T) and local chemical composition (c_i) for a system of n alloying elements, i.e. $\Delta G_{ij}(c_1(\vec{r}, t) \dots c_n(\vec{r}, t), T)$. Since the driving force, ΔG_{ij} , is dependent on the local concentration of elements, Equation 4.1 is coupled with diffusion equations given by Eiken *et al.* [28]

$$\frac{\partial x^k}{\partial t} = \nabla \sum_{i=1}^{\theta} \sum_{l=1}^{\varepsilon} \varphi_i D_i^{kl} \nabla x_i^l ; D_i^{kl} = \sum_{m=1}^{\varepsilon} M_i^{ch,km} \frac{\partial f_i(\bar{x}_i)}{\partial x_i^m x_i^l} \quad (4.2)$$

where the atomic mobility matrix, $M_i^{ch,km}$, and the free energy density $f_i(\bar{x}_i)$ of the grain i are combined with its diffusivity, D_i^{kl} , and k, l are the solute and solvent elements in the alloy, respectively.

In the case of phase-field modelling, the interface mobility is finite, meaning that a certain balance is established between diffusion of alloying elements and interface motion. Hence, interface migration takes place when the local compositions gives rise to a local driving force. If the neighbouring grains are of the same phase (γ or α), the interface mobilities and interfacial energies are considered as $M_{\gamma\gamma}$ or $M_{\alpha\alpha}$ and $\sigma_{\gamma\gamma}$ or $\sigma_{\alpha\alpha}$, respectively. In such a case, the driving force, ΔG_{ij} , for interface movement is given by the product of the respective interfacial energies and the curvature term (within square brackets of Equation 4.1).

4.3.2. Simulation Conditions and Microstructure Development

The MICRESS[®] software [29] was used to perform phase-field simulations. Two-dimensional (2D) and one-dimensional (1D) multi-phase field models are used to investigate the partitioning behaviour of carbon and manganese between martensite (α^l) and austenite (γ) and the α^l/γ interface movement at respective temperatures and times. Different from Mecozzi *et al.* [30], who studied the Q&P process through phase-field modelling in a Fe-C binary system, this work involves a ternary alloy system containing iron, carbon and manganese.

Since it is not possible to simulate the martensitic transformation in phase-field modelling, acicular ferrite is considered as martensite (α^l), as it has a close resemblance with the martensitic morphology. During the simulations, diffusivity of carbon and manganese [31-33], in austenite and acicular ferrite are derived by coupling with ThermoCalc[®] [34]. This allows us to consider the influence of the concentration of alloying elements on their diffusivity.

2D simulations were performed to study the influence of the spatial distribution, the grain size, and morphology of the phases on the partitioning kinetics of carbon and manganese. 1D simulations, which are computationally less expensive, were applied to investigate local changes at the α^l/γ interface with a higher resolution (smaller grid size) than 2D simulations. Since the initial quench temperature is similar in all the Q&P experiments and no phase transformations were observed during the re-heating stage, the same microstructure is considered for simulations at the partitioning temperatures of 400 °C, 500 °C and 600 °C.

The domain size in 2D simulations is set to be 40x40 μm^2 with a grid size of 50 nm. Periodic boundary conditions were set for all simulations. The interface thickness (200 nm) is set to be 4 times the grid size. It is important to note that the interface in phase-field modelling is a mixture of the respective phases present in a certain ratio. So, carbon and manganese inside the interface have a combination of

thermodynamic and diffusional properties of ferrite and austenite. This is relevant for the understanding of observations in the following sections. Due to the grid size (50 nm) used in the 2D simulations, interface movement is only detected when it is beyond 50 nm.

In the reference material, the Q&P process started with full austenitisation, followed by the formation of 0.75 volume fraction of martensite during the first quench. To allow a similar microstructural development in simulations, initially, a fully austenitic 2D microstructure with 60 grains is developed as shown in Figure 4.1a. The grain colours shown in Figure 4.1a represent different crystallographic orientations. The crystal orientation of each grain is the angle between the local coordinate system of the grain and the global coordinate system of the simulation domain. This simulated fully austenitic microstructure is quenched at a rate of 30 °C/s, during which a 0.75 volume fraction of ferrite is formed, similarly as described in the work of Mecozzi *et al.* [30]. In the simulated microstructure (Figure 4.1b) austenite grains, ranging between 100 nm and 5 μm , located between martensite laths, can be observed which is a close representation of typical experimentally observed Q&P microstructures [35].

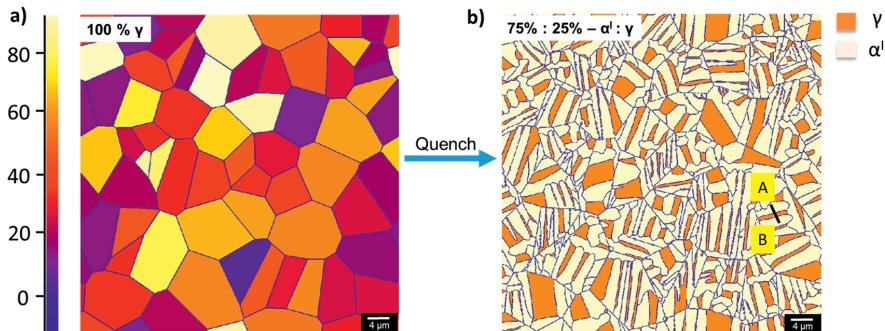


Figure 4.1. a) Initial 2D austenite microstructure (γ). The grain colours represent the different crystallographic orientations, and b) Simulation microstructure developed after the initial quench, with 0.75 martensite (α') and 0.25 austenite (γ) volume fractions. The line A-B indicates the region selected for a detailed analysis.

The resulting microstructure, shown in Figure 4.1b, is taken as an input microstructure for the partitioning stage, at partitioning time $t_p = 0$ s. To represent the condition that occurs at the beginning of the experimental partitioning stage, the elemental concentration in the ferrite and austenite is manually set equal to the nominal composition. The carbon supersaturated ferrite at the beginning of partitioning stage has same composition as the experimentally observed martensite. Hence, from now on, the BCC phase in the simulations will be addressed as martensite (α').

The simulated martensite/austenite microstructure is then subjected to an isothermal holding at the partitioning temperatures (T_p) of 400 °C, 500 °C and 600 °C for partitioning times (t_p) up to 3600 s. Although competitive reactions such as precipitation of carbides and pearlite formation (around 0.02 volume fraction) were experimentally identified and discussed in Chapter 3, these reactions are not

considered during the partitioning stage of the current phase-field simulations. This fact also helps us to investigate the influence of the competitive reactions on the extent of austenite stabilisation.

The mobility of the martensite/austenite (α/γ) interface during initial quench and partitioning stage is an adjustable parameter to be fitted based on experimental observations. The interface mobilities during the partitioning stage (Table 4.1) are considered to be temperature dependent according to an Arrhenius relation:

$$M_j = M_j^0 \cdot \exp\left(-\frac{Q_{Mj}}{RT}\right) \quad (4.3)$$

where M_j is the mobility of the interface j , $Q_{(Mj)}$ is the activation energy of the interface j , R is the universal gas constant ($8.314 \text{ J mol}^{-1} \text{ K}^{-1}$), and T is the temperature in Kelvin. In this case, the activation energies of the interfaces α/α' , α'/γ and γ/γ during the partitioning stage were set to be 140 kJ/mol [36-38]. The pre-exponential factor of the mobility, M_j^0 (Table 4.1), is set to reproduce the experimental observations of austenite growth at the partitioning temperature of $600 \text{ }^\circ\text{C}$ and then extrapolated to lower temperatures. The interfacial energy [39] and activation energy of the different interfaces in the microstructure are kept constant at all partitioning temperatures.

Table 4.1. Data of fitted pre-exponential factors between α/α' , α'/γ and γ/γ phases based on experiments.

Phase	α'/α'	α'/γ	γ/γ	Ref.
Pre-exponential factor, M_j^0 ($\text{m}^4\text{J}^{-1}\text{s}^{-1}$)	1.65×10^{-12}	1.05×10^{-8}	1.65×10^{-12}	-
Activation energy, Q_M (kJ mol^{-1})	140	140	140	[36-38]
Interfacial energy (J m^{-2})	0.1	0.5	0.1	[39]

At a later stage, 1D simulations are also performed, which allow us to increase the resolution by reducing the grid size down to 2 nm to observe the partitioning of manganese. A 1D simulation system was designed by keeping a constant size ratio of austenite to martensite films in comparison to the 2D simulation profile (segment A-B in Figure 4.1b). The interface thickness is considered to be 4 times the grid size, i.e. 8 nm . The interface mobility values and the diffusivity data are kept the same as for 2D simulations. From the literature, it was observed that the average size of the martensite films is around 180 nm [40-42]. Hence, martensite and austenite lath sizes are defined to be 180 nm and 52 nm , respectively. Due to mirror boundary conditions, only half thickness of the lath width is considered. Therefore, the total length of the 1D simulation system, including the interface, is set to be 124 nm .

4.4. Results

4.4.1. 3D Atom Probe Tomography (APT) measurement

3D-APT experiments were performed on the specimen partitioned at $600 \text{ }^\circ\text{C}$ for 300 s . Figure 4.2a shows the corresponding 3D atom map of iron and a manganese iso-concentration surface of $11.7 \text{ at. } \%$. Figure 4.2b displays the concentration profiles of manganese and carbon along the arrow indicated in the iron

atom map. Equilibrium concentrations of carbon and manganese in both phases at 600°C, calculated using ThermoCalc, are also represented in Figure 4.2b.

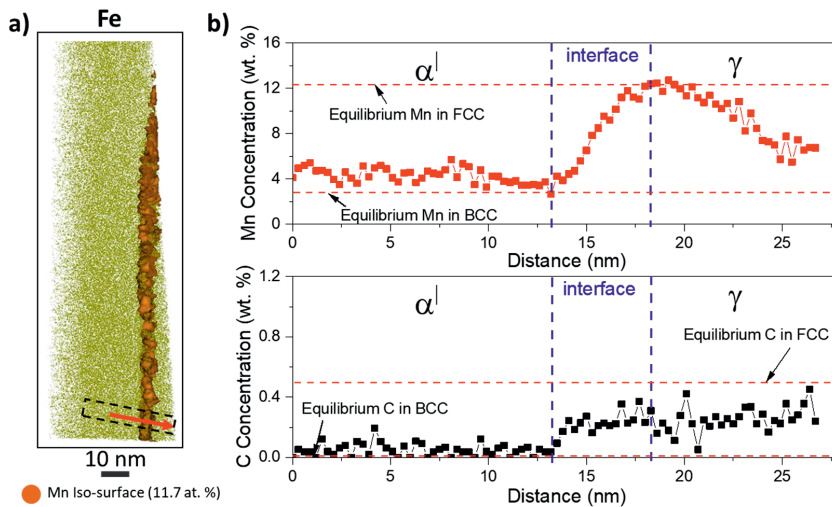


Figure 4.2. a) Three-dimensional (3-D) atom map of iron of the Q&P processed medium manganese steel specimen partitioned at 600 °C for 300 s, b) manganese and carbon concentration profiles along the red arrow indicated in the iron atom maps (a).

From Figure 4.2b it is observed that the carbon and manganese enriched regions have an average and maximum carbon content, excluding interface region, of around 0.32 wt. % and 0.44 wt. %, respectively. This is certainly higher than the nominal carbon content of the alloy (0.19 wt.% C), and in close agreement with the carbon concentration in austenite measured by XRD (0.44 ± 0.01 wt.%) on the QP600-300 sample. Moreover, this measurement shows regions that are enriched with maximum and minimum concentrations of 12.2 wt.% and 2.8 wt.% manganese, respectively. Observations across such interfaces from the earlier studies [3-5] indicate that the carbon- and manganese-enriched zones are retained austenite. Usually, the minimum and maximum content of manganese are observed in the martensite and austenite phases close to the α/γ interface, respectively. Based on this interpretation, the interface is identified to have a thickness of around 5 nm (region in between the blue dashed lines in Figure 4.2b) from the current 3D-APT measurements. However, the 5 nm interface (accommodating almost 17 atoms along the width of the interface) seems to be thicker than in reality (which could be around 2 nm). This variation could be due to the local magnification effect in Atom Probe Tomography [43]. From the measured region in the iron atom map (red arrow in Figure 4.2a) the region on the left side of the interface is identified as martensite which is around 13 nm and the region on the right-side of the interface is identified as austenite grain which is around 8.5 nm. A depletion of manganese concentration for around 13 nm in the martensite grain and an enrichment of manganese concentration for around 7.5 nm in the austenite grain is observed. The austenite region close to the α/γ interface is enriched up to the equilibrium manganese concentration.

4.4.2. 2D Phase-Field Simulations

In order to understand the mechanism behind the partitioning of substitutional alloying elements and the α'/γ (martensite/austenite) interface migration, multi-phase-field simulations are performed. This section presents the simulated distribution of carbon and manganese across austenite and martensite grains after partitioning at temperatures of 400 °C, 500 °C and 600 °C for times up to 3600 s. In order to study the partitioning kinetics of carbon and manganese, the element distribution maps obtained after different partitioning temperatures are analysed. In addition to the maps, the segment A-B (Figure 4.1b) is selected to analyse the distribution of carbon and manganese at different partitioning times. This selection represents an austenite grain of the order of nanometres surrounded by martensitic laths within the same prior austenite grain. Hence, the segment A-B, which comprises of 350 nm austenite grain surrounded by 800 nm martensite grains on either side, seems to be an appropriate region for further analysis.

The diffusivity of manganese in austenite is derived by coupling with ThermoCalc database, that is used for the current simulations. Based on this, the diffusion distance of manganese in austenite at the partitioning temperatures of 400 °C, 500 °C, and 600 °C, with time Figure 4.3, is calculated using:

$$x_{i,j} = \sqrt{6 \cdot D_j^i \cdot t} \quad (4.4)$$

where D_j^i and $x_{i,j}$ is the diffusivity and diffusion distance of an alloying element i (manganese) in phase j (austenite), respectively, and t is the time. Partitioning distance of manganese after maximum partitioning times at respective partitioning temperatures, applied in the current work, are indicated by dashed green lines in Figure 4.3.

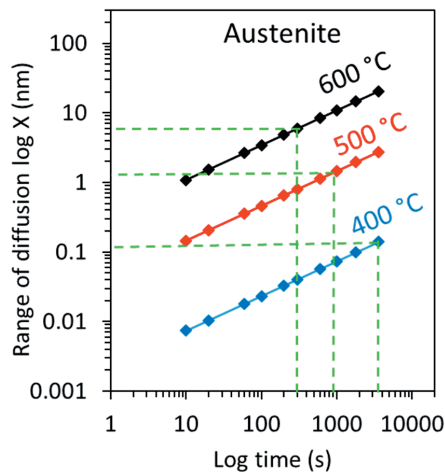


Figure 4.3. Diffusion distance of manganese in austenite, calculated based on ThermoCalc diffusivity database (TCFE9) [33] at 400 °C, 500 °C and 600 °C.

Partitioning at 400 °C

Figure 4.4a shows the carbon distribution maps after partitioning at 400 °C for 180 s, 300 s and 3600 s. After 180 s, carbon partitioning is evidenced by the higher carbon contents in austenite, next to the α^l/γ interfaces compared to those in the inner part of the austenite grains. In general, the smaller (and thinner) the austenite grain is, the higher its carbon concentration. As the partitioning time increases, the carbon homogenises across the austenite grains. After 3600 s, uniform orange-red colours inside the austenite grains indicate that carbon homogenisation is close to completion. Nevertheless, a few large austenite grains (in the order of 4 μm - 5 μm) are not completely homogenised with carbon even after 3600 s of isothermal holding. No interface movement is observed during partitioning at 400 °C.

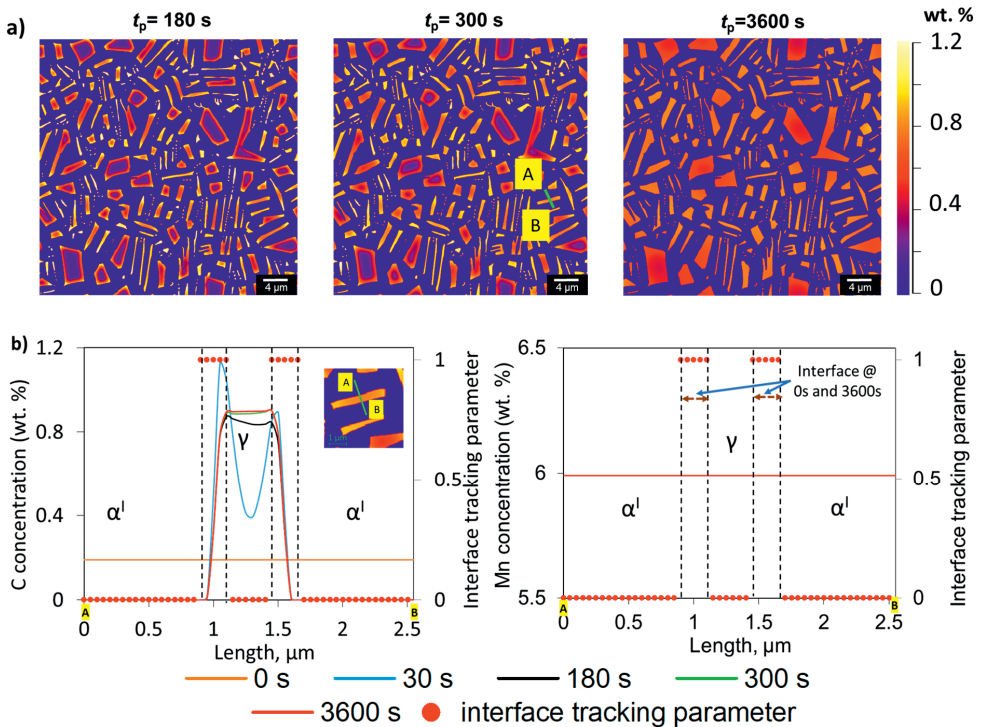


Figure 4.4. a) Carbon concentration maps after 180 s, 300 s and 3600 s, showing the line segment AB cutting a smaller austenite grain b) carbon and manganese concentration along the line AB, cutting the smaller austenite grain, at partitioning temperature of 400 °C. The black dashed lines mark the interface region, which did not change with time in the current simulation.

Figure 4.4b presents the carbon and manganese concentration profiles along the segment A-B, together with an interface tracking parameter, represented by dots. The interface tracking parameter allows monitoring the precise position of the interface during partitioning, *i.e.* a value of 1 indicates interface, while a value of 0 indicates the region of a phase, either martensite or austenite. At the beginning of the partitioning time ($t_p = 0$ s), the carbon and manganese concentrations in both austenite and martensite are constant. Due to the different chemical potential of carbon in martensite and austenite, carbon

partitions from martensite into austenite. After 30 s of isothermal holding, martensite is depleted in carbon and a sharp increase in carbon content inside the interface close to austenite grain is observed. This indicates that, initially, carbon partitioning occurs in the austenite-dominated region of the interface and, with time, carbon is partitioned into the austenite grain. With the increase in holding time, the carbon diffusion progresses and the peak inside the interface is reduced due to carbon homogenisation inside the austenite grain.

After 180 s of isothermal holding, the austenite region close to the point B appears to be enriched with less than close to point A. This can be explained by the presence of another austenite grain close to the martensite grain B (Figure 4.4a), which may partially compete for the carbon from the same martensite grain lying in between. After 300 s of isothermal holding, the carbon distribution across the austenite grain is homogenous and the carbon content in austenite and martensite remains almost unchanged between partitioning times of 300 s to 3600 s.

In contrast to carbon, manganese does not show partitioning, even in the nanometric austenite films. As is observed from Figure 4.4b, no signs of interface movement or manganese depletion in martensite or enrichment in austenite are observed after 3600 s. Also, no manganese concentration gradient is observed inside the interface region. This could be because the range of diffusion of manganese in FCC lattice, after 3600 s at 400 °C (0.1 – 0.2 nm, Figure 4.3) is smaller than the grid size of the current simulations (50 nm). Although earlier experimental studies [11-13] reported a 2 - 3 nm range of diffusion of manganese during partitioning at 400 °C for times up to 300 s, no conclusive interpretation of the underlying mechanism was made.

Partitioning at 500 °C

Figure 4.5a shows the carbon distribution maps after partitioning at 500 °C for 180 s, 300 s and 900 s. Similarly to partitioning at 400 °C, no redistribution of manganese is observed in the microstructure and, therefore manganese distribution maps are not shown. Also, no interface movement is observed during partitioning at 500 °C. The homogenisation of carbon across the austenite grains occurs faster at 500 °C than at 400 °C, as can be inferred from the rather uniform colour of the austenite grains after 180 s of partitioning. As the partitioning time increases, large austenite grains increase their carbon content, while that of some small grains is reduced due to continuous carbon redistribution in the microstructure. Small austenite grains (for *e.g.* as indicated by a white arrow in Figure 4.5a) can reach carbon contents as high as 1.2 wt. % C within the first 180 s of partitioning. However, after 3600 s, the overall carbon concentration in austenite is about 0.70 wt. %.

Figure 4.5b shows the concentration profiles of carbon and manganese along the segment A-B for partitioning times up to 900 s. The inset in the concentration profile of carbon shows carbon distribution inside martensite during partitioning at 500 °C. As expected, carbon partitioning is faster at 500 °C than at 400 °C. Just after 2 s of isothermal holding at 500 °C, a similar carbon profile as that after 30 s at

Chapter 4

400 °C has developed in the austenite grain. After 60 s, austenite seems to reach a homogeneous carbon concentration. However, until 900 s of partitioning time, the carbon concentration in austenite is continuously decreasing. This shows that there is a continuous redistribution of carbon among the neighbouring austenite through martensite grains (indicated in the inset of Figure 4.5b). After partitioning at 500 °C for 900 s, no signs of depletion of manganese in martensite or enrichment in austenite are observed. Figure 4.3 shows that the diffusion range of manganese in austenite is only around 1 nm. Hence, also at a temperature of 500 °C, the partitioning of manganese is not observable under the employed simulation conditions.

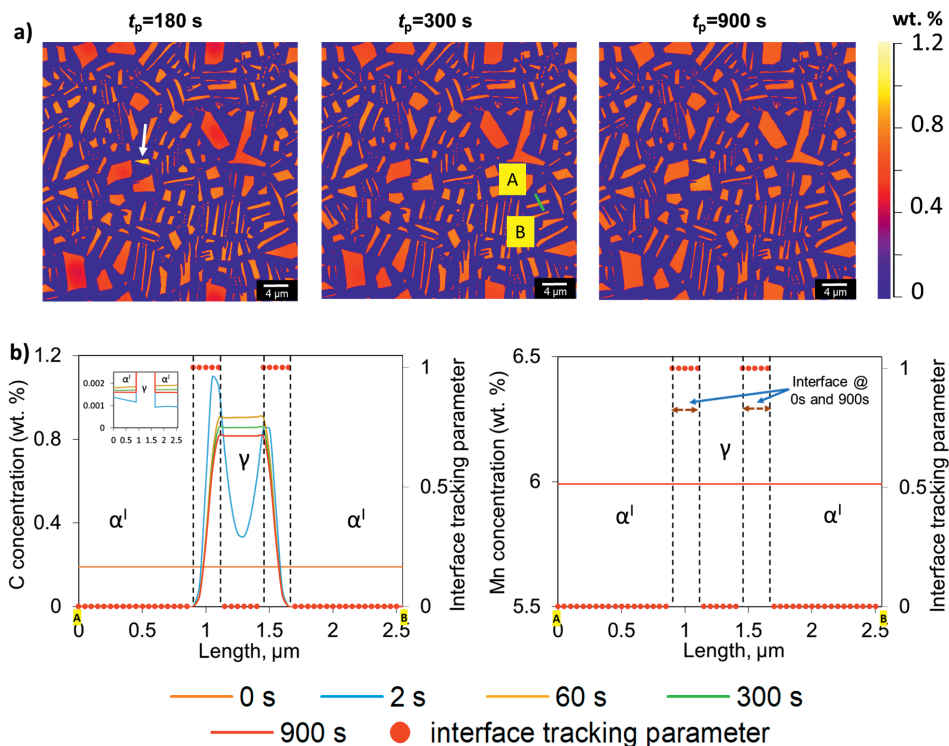


Figure 4.5. a) Carbon concentration maps after 180 s, 300 s and 900 s, showing the line segment AB cutting a smaller austenite grain b) carbon and manganese concentration along the line AB, cutting the smaller austenite grain, at partitioning temperature of 500 °C. The black dashed lines mark the interface region, which did not change with time in the current simulation.

Partitioning at 600 °C

As explained in Section 4.3, the α/γ interface mobility parameter is adjusted to lead to the experimentally observed 0.04 volume fraction of reverted austenite at the end of 300 s of partitioning time at 600 °C.

Figure 4.6 shows, in the form of colour maps, the microstructure evolution and carbon and manganese concentration after partitioning at 600 °C for 60 s, 180 s and 300 s. A gradient in manganese concentration in the α/γ interfaces is observed and this gradient increases with time. Certain austenitic

grains in the microstructure are also observed to grow with increasing partitioning time. A manganese concentration gradient inside the α'/γ interface region is observed irrespective of the α'/γ interface movement. Figure 4.7 shows a magnification of the region of interest, across the segment A-B, after partitioning times of 1 s and 300 s, which reveals the growth of the austenite grain. At the end of 300 s of isothermal holding, the movement of the α'/γ interface on either side of austenite resulted in a 150 nm growth of this austenite grain.

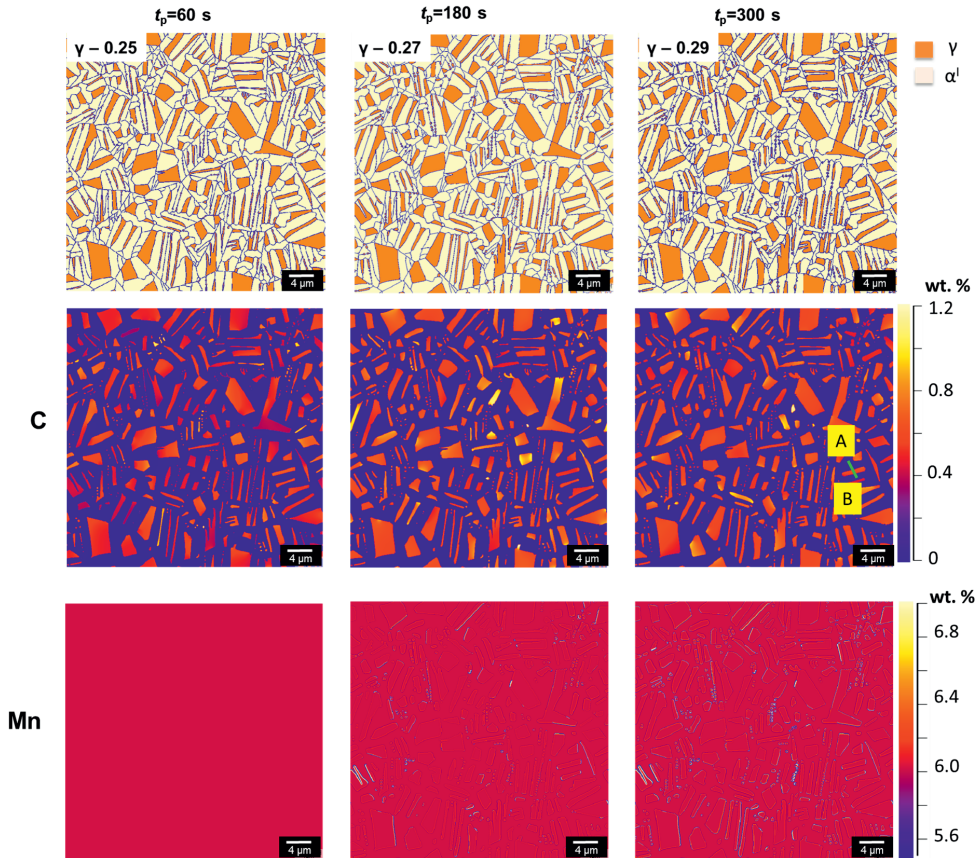


Figure 4.6. Colour maps showing the microstructural evolution (top), the carbon concentration (middle) and the manganese concentration (bottom) after partitioning at 600 °C for 60 s, 180 s and 300 s.

Figure 4.8 shows the concentration profiles of carbon and manganese along the segment A-B for partitioning times up to 300 s. After 0.2 s, the centre of the austenite grain is enriched with a carbon content similar to that after 2 s at 500 °C, indicating the more rapid diffusion of carbon at 600 °C. With the increase in time, due to continuous carbon redistribution in the microstructure, a fluctuation in the carbon profiles is observed. After 60 s of isothermal holding, austenite is enriched with 0.94 wt.% C and at the same time a gradient in manganese concentration is observed inside the interface. At partitioning time of 140 s the carbon concentration in austenite is decreased to 0.64 wt.% C. This is because of the redistribution of carbon between austenite and martensite as a result of interface movement detected

after 140 s. After 230 s, when interface movement is again detected, a similar behaviour of carbon is observed. From Figure 4.9 it is observed that manganese concentration profiles are developed with increase in isothermal holding time but only inside the α/γ interface with a maximum of ± 0.5 wt.% gradient.

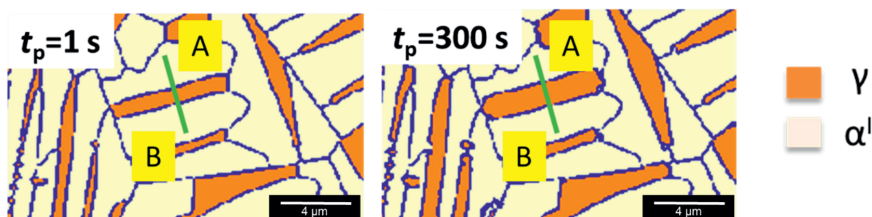


Figure 4.7. Simulation microstructure at partitioning temperature of 600 °C after partitioning for 1 s and 300 s.

After 140 s of isothermal holding, only the α/γ interface close to point B migrates. The reason for the austenite growth only on one side of the grain might be attributed to the uneven driving force developed due to local concentration. The current simulations do not consider the crystallographic orientation relationships and the interface mobility is fixed for all interfaces, the driving force for interface movement is generated when the free energy difference due to local concentrations of alloying elements is sufficiently large. Therefore, the current simulations show that the spatial distribution of surrounding grains and local elemental concentration near the α/γ interfaces influence the interface movement.

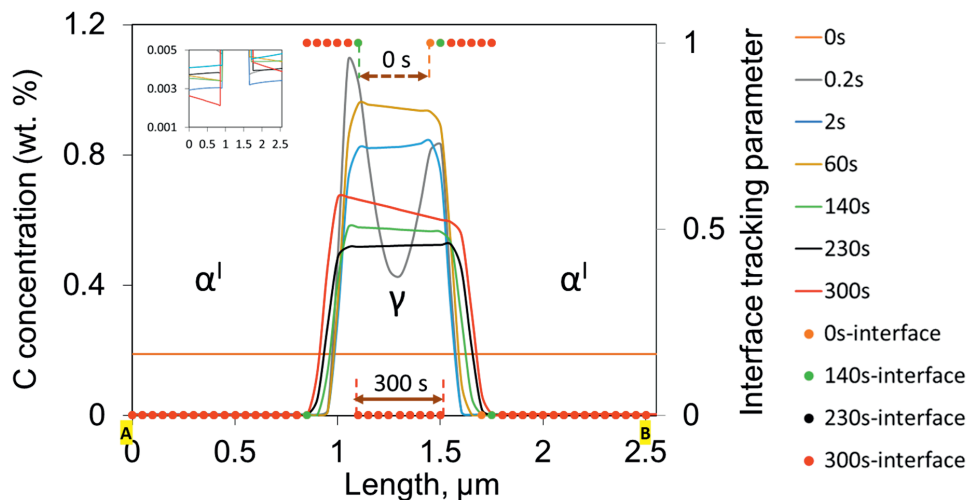


Figure 4.8. Carbon concentration profile along the line AB (Figure 4.7), cutting the smaller austenite grain, at partitioning temperature of 600 °C. The black dashed lines mark the interface region.

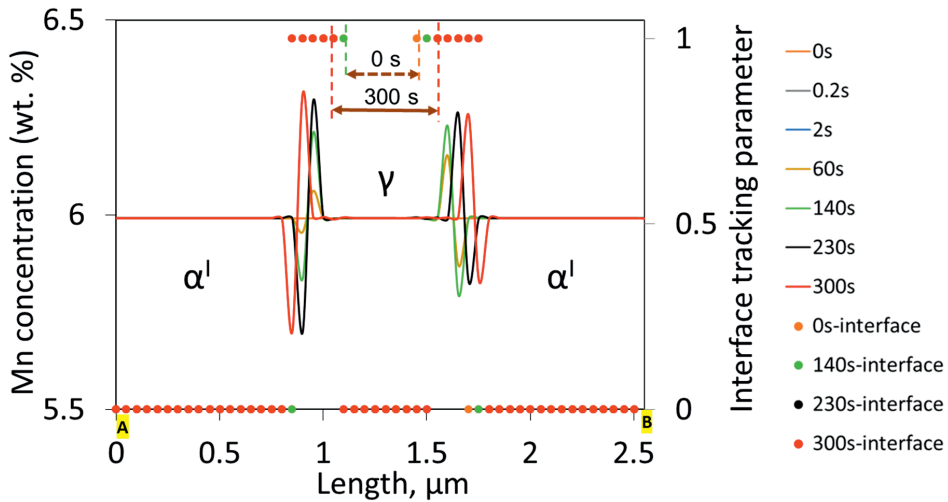


Figure 4.9. Manganese concentration profile along the line AB (Figure 4.7), cutting the smaller austenite grain, at partitioning temperature of 600 °C. The black dashed lines mark the interface region.

4.4.3. 1D Phase-Field Simulations

Due to the large grid size employed in 2D simulations (50 nm), compared to the much smaller diffusion distance of manganese under the investigated partitioning conditions, it is not possible to study the partitioning of manganese from martensite into austenite using the 2D microstructure designed for that purpose (Figure 4.1b). Hence, 1D simulations with a 2 nm grid size were performed at the partitioning temperatures of 400 °C, 500 °C and 600 °C. The interface thickness is considered to be 4 times the grid size, *i.e.* 8 nm. The interface mobility values and the diffusivity data are kept the same as for 2D simulations. The martensite and austenite lath sizes are defined to be 180 nm and 52 nm, respectively. Due to mirror boundary conditions, only half the thickness of the lath width is considered. So, the total length of the 1D simulation system, including the interface, is set to be 124 nm. Since α'/γ interface movement and manganese partitioning into austenite are observed only at 600 °C, the respective simulation results are shown here.

Figure 4.10 and 4.11 show the concentration profiles of carbon and manganese for partitioning times up to 300 s at a temperature of 600 °C, respectively. The elemental concentration profiles in martensite and austenite phases are measured along the width of the 1D-simulation system. The equilibrium concentrations of manganese in austenite and ferrite are included in Figure 4.11. Since the diffusivity of carbon is very high at 600 °C, the carbon content in the austenite grain has already homogenised after 0.2 s. With the increase in partitioning time, α'/γ interface migration towards martensite (α') is observed, and at the same time carbon is redistributed between austenite and martensite grains. After 2 s of isothermal holding, enrichment and depletion of manganese is observed inside the α'/γ interface close to austenite and martensite grains, respectively (Figure 4.11). With further increase in isothermal holding time, depletion of manganese in martensite is detected. After 200 s of partitioning time, the α'/γ interface

movement towards martensite is observed, leading to the growth of the austenite grain. At the end of 300 s of partitioning time, the depletion and enrichment length of manganese in martensite and austenite is around 20 nm and 6 nm, respectively. Interestingly, within the 300 s of partitioning time, manganese enrichment is primarily observed in the newly formed austenite.

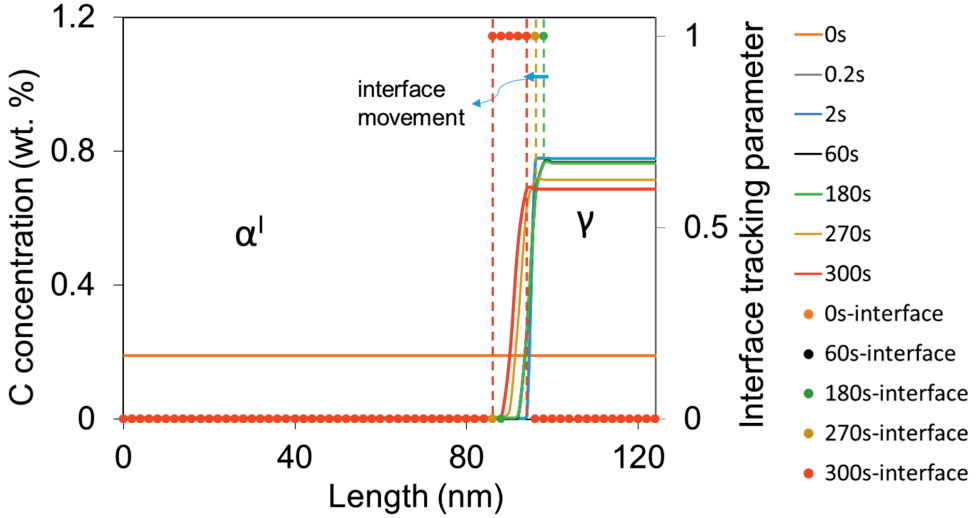


Figure 4.10. Carbon concentration profiles along the martensite and austenite grains, from the 1D simulations, at the partitioning temperature of 600 °C for times up to 300 s.

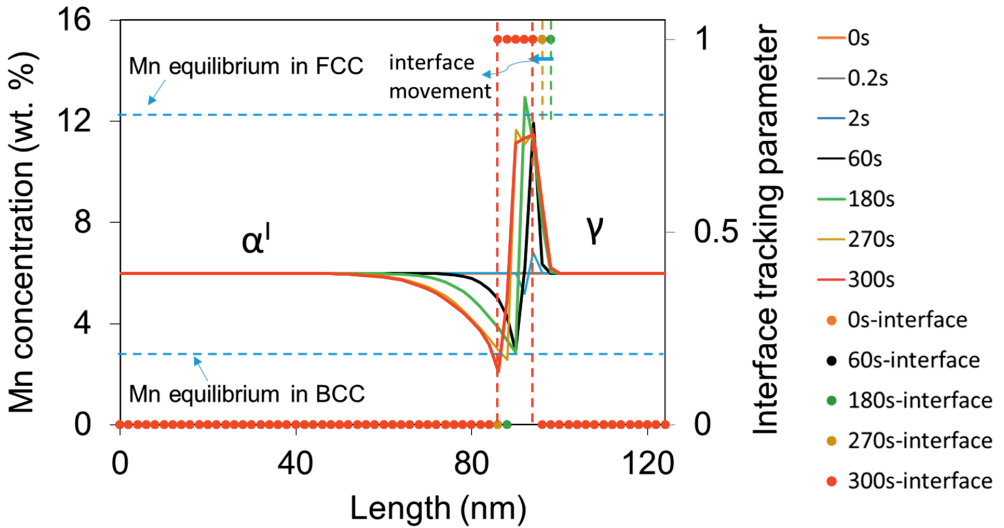


Figure 4.11. Manganese concentration profiles along the martensite and austenite grains, from the 1D simulations, at the partitioning temperature of 600 °C for times up to 300 s.

4.5. Discussion

In order to understand the mechanism of austenite growth during the partitioning stage, both experimental and simulation results are analysed.

4.5.1. Austenite Reversion and Manganese Partitioning at 600 °C

During the partitioning stage, interface movement is observed when there is a local free-energy difference between phases as a result of a difference in chemical potential of alloying elements between austenite and martensite in combination with the interface mobility. In 2D simulations at 600 °C for partitioning times up to 300 s, carbon partitioning occurs continuously with the increase of partitioning time, and manganese concentration gradients are developed only inside the α/γ interface (Figure 4.8 and 4.9). The interface region here is a mixture of martensite and austenite. Hence, it can be interpreted that the manganese depletion observed in the martensite-dominated region of the α/γ interface and the manganese enrichment in the austenite-dominated region of the α/γ interface represents partial partitioning of manganese into the austenite.

From the 2D phase field simulations at 600 °C, Figure 4.9, initially carbon partitioning from martensite to austenite occurs very fast. Due to higher diffusivity of carbon, compared to that of manganese, with the increase in partitioning time the chemical potential of carbon equilibrates at the interface while no significant diffusion of manganese has taken place. The resulting free-energy difference, due to the chemical-potential difference of manganese, leads to austenite growth through the α/γ interface movement, which is significant if the interface mobility is sufficiently high. This is followed by homogenisation of carbon in the austenite. After 60 s of partitioning time manganese partitions from martensite to austenite in order to equilibrate its chemical potential, in this case it is only inside the interface. After 140 s a noticeable growth of austenite is observed. As a result further carbon partitioning occurs from martensite to austenite. With the increase in austenite grain size, carbon redistribution occurs inside the austenite grain resulting in the decrease in overall carbon concentration in the austenite grain. Due to higher diffusivity of carbon, the chemical potential of carbon equilibrates quickly. After 230 s of partitioning time further noticeable interface movement towards martensite is observed resulting in a further decrease in the carbon concentration in the austenite grain. After 300 s partitioning time, an overall growth of 150 nm is observed in the selected austenite grain. The above phenomenon continues to occur with further increase in partitioning time, eventually leading to full equilibrium.

Interestingly, at 300 s partitioning time an increase and a decrease in carbon concentration in austenite and martensite is observed, respectively (inset of Figure 4.9). Although the concrete reason behind such increase in carbon concentration in austenite is not understood, this is possible either when the martensite grain grows into austenite, which results in carbon redistribution, or when a new local equilibrium is established at the interface due to manganese concentration gradient developed inside the interface that requires further carbon enrichment of the austenite. In addition, it can also be an effect of adjacent austenite grains.

In 1D phase field simulations, due to relatively small size of austenite and martensite films, the equilibration of chemical potential of carbon and homogenisation of carbon occurs in very short time. Hence, no gradients of carbon are observed as in the case of 2D simulations. In 1D simulations (Figure

4.10 and 4.11), a homogeneous carbon concentration is achieved in both phases after 0.2 s and is maintained until 180 s. The concentrations are observed to be higher than the equilibrium carbon concentration of either phase. At the same time depletion of manganese in martensite and enrichment of manganese in austenite-dominated interface is observed. It can be observed that after 180 s of partitioning time, manganese concentrations in the martensite-dominated and austenite-dominated interface regions are close to equilibrium. In the case of 1D simulation, due to the smaller austenite and martensite grains, manganese is able to equilibrate at the interface faster than in the case of 2D simulations. However, the driving force, in combination with the interface mobility, appears not to be high enough to result in an interface movement that exceeds the grid size. At 270 s austenite growth is observed when the concentration of both carbon and manganese in austenite is above the equilibrium concentration. Since the elemental concentrations in austenite are above the equilibrium concentration values, in order to achieve equilibrium concentrations in austenite, growth of austenite is necessary. This is accomplished through a driving force for interface movement towards martensite. This leads to a decrease in carbon and manganese concentration in austenite.

In the case of 2D simulations, since the manganese concentration is far from the equilibrium value, a higher driving force for interface movement is present, while in the case of 1D simulations the driving force for interface movement is relatively low as the manganese concentration is close to the equilibrium value. Due to the smaller grain size in 1D simulations, which lead to faster equilibration of carbon and manganese, and the presence of lower driving force in 1D simulations, after 300 s of partitioning time, the interface in 1D simulations moved only over 4 nm, while in the case of 2D simulations an overall interface movement of 150 nm is observed. Based on the above discussion it is understood that the size of the austenite and martensite grains play a crucial role in the α/γ interface movement.

Mechanisms of reverted austenite formation

The concentration profile of manganese derived from the APT experiment, Figure 4.2b, shows a 7.5 nm range of manganese enrichment in the austenite. Data derived from the ThermoCalc database show that the diffusion range of manganese in austenite after 300 s of isothermal holding at 600 °C is around 6 nm. Although there is a close agreement between the experimental and theoretical observations, the mechanisms related to austenite reversion and manganese enrichment in austenite during the partitioning stage are not very well understood. Based on the observations from simulations, the carbon and manganese partitioning behaviour and the interface migration mechanism during the partitioning stage of the Q&P process is illustrated in Figure 4.12. The blue and red dotted lines show the equilibrium concentrations of carbon in austenite and martensite, and that of manganese in austenite and martensite, respectively. The blue and red solid lines show carbon and manganese concentration profiles, respectively. I_0 , I_i , and I_f indicate the initial, intermediate and final position of interface during the partitioning stage, respectively.

Step 1: During the partitioning stage, carbon partitions from carbon super-saturated martensite to austenite, resulting in carbon concentrations higher than the equilibrium concentrations in both the martensite and the austenite close to the α'/γ interface. This develops a driving force for the α'/γ interface movement towards martensite. During this time, manganese remains practically immobile due to its low diffusivity. This step occurs at very short partitioning times (in the order of several seconds) as the diffusivity of carbon is high.

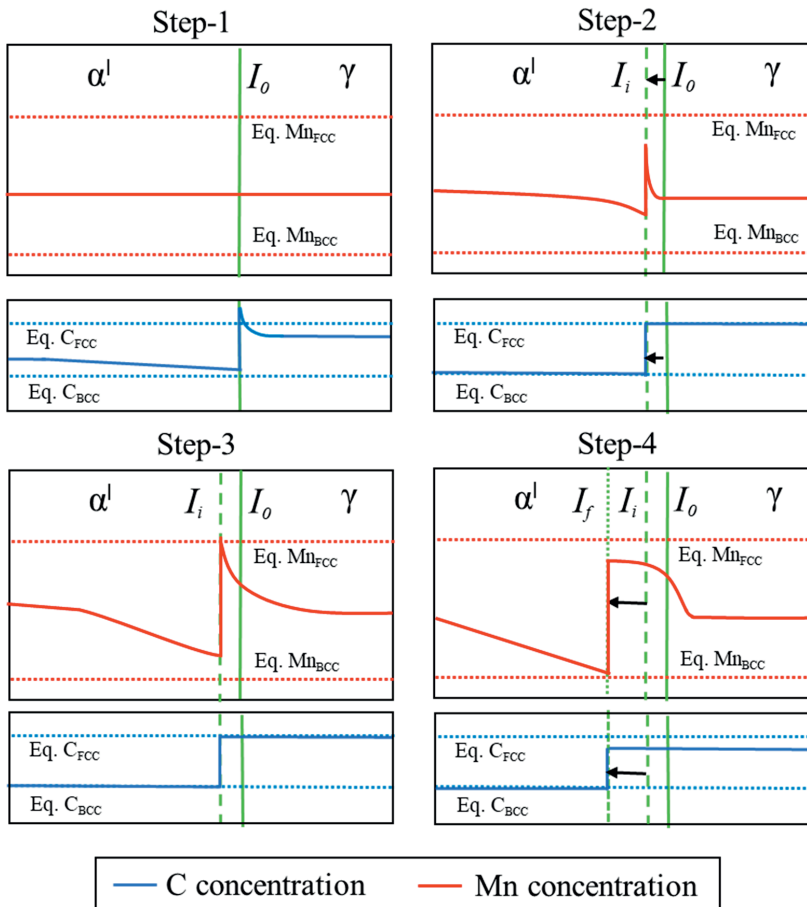


Figure 4.12. Illustration of carbon and manganese partitioning, and interface migration mechanism during the partitioning stage of the Q&P process. In this figure α' – martensite, γ – austenite, I_0 – initial interface position, I_i I_f – interface position after migration.

Step 2: With the interface velocity being the product of the driving force and the interface mobility, the α'/γ interface moves towards martensite, leading to austenite growth. Due to its high diffusivity, carbon equilibrates in both phases quite fast. With increasing partitioning time, manganese concentration in the austenite grain next to the interface at its new position (I_i) increases as a result of manganese partitioning from martensite to austenite in the process of equilibration of its chemical potential across the interface.

Step 3: With increasing isothermal holding time, further manganese partitioning from martensite to austenite occurs in order to equilibrate its chemical potential across both phases. Due to the low diffusivity of manganese in austenite, relative to that in the martensite, manganese accumulates in the austenite grain, next to the α/γ interface. With the increasing manganese concentration next to the interface, a driving force for α/γ interface movement is generated, when the manganese concentration reaches values higher than the equilibrium value. This is possible because also the manganese concentration in the martensite is higher than the equilibrium. This situation is similar to that observed in the 1D simulations.

Step 4: As a result of the driving force, the α/γ interface moves, resulting in further austenite growth. This austenite growth leads to the reduction of carbon concentration in austenite and a reduction of manganese concentration in the austenite next to the α/γ interface. Observations from 1D simulations show that a significant manganese concentration present in the austenite-dominated region of the α/γ interface, prior to the interface movement, remains at the same position after the interface movement, as shown in the step 4 of Figure 4.12, which resulted in enrichment of newly formed austenite with higher concentration than the nominal composition. Hence, it can be interpreted that during the interface migration not all the manganese moves along with the interface. This could be due to migration of the interface being effectively faster than the manganese diffusion.

Based on the above discussion, the interface movement as derived from the APT measurement is marked on the manganese concentration profile of the specimen partitioned at 600 °C for 300 s in Figure 4.13. The solid (I_0) and dashed (I_f) blue lines indicate the position of the α/γ interface at partitioning time, $t_p = 0$ s and $t_p = 300$ s, respectively. Since manganese partitioning and austenite growth are understood to be simultaneous phenomena, the 7.5 nm range over which manganese enrichment is observed in the austenite can be interpreted as the range over which α/γ interface movement is observed after 300 s. As indicated schematically in Figure 4.12, Step 4, the initial position of the interface, I_0 , is envisioned to be close to the position where the manganese concentration exceeds the original 6 wt.%. From this position the interface has moved to the final position, I_f , where the manganese concentration reaches its minimum at the distance 13 nm, see Figure 4.12, Step 4. Towards smaller distance, so to the left in the Figure 4.13, the manganese concentration increases, indicating the presence of martensite in that region. The transition is less sharp in the ATP observations than in the schematics of Figure 4.12, most likely due to instrumental conditions. The actual final interface position can be expected to be between 13 and 18 nm. The close agreement between the range of manganese enrichment in austenite observed from experiments (7.5 nm) and the diffusion distance of manganese in austenite calculated from the ThermoCalc database (6 nm), Figure 4.3, after 300 s of isothermal holding time shows that the above discussed mechanism of austenite reverse transformation and manganese partitioning is plausible.

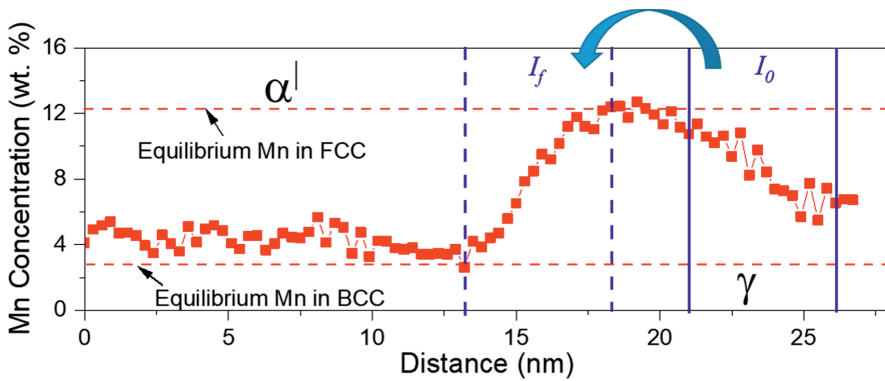


Figure 4.13. Figure shows manganese concentration profile derived from the APT measurement (same as the manganese profile shown in Figure 4.2b). The dashed and solid blue lines indicate the position of the α/γ interface at partitioning time, $t_p = 0$ s (I_0), and at $t_p = 300$ s (I_f), respectively.

4.5.2. Microstructural Mechanisms to Stabilise Austenite in a Wide Range of Partitioning Temperatures

Suppression of competitive reactions: The average carbon content in austenite at the end of the partitioning stage is analysed based on the experimental and simulation results. The experimental carbon content in austenite at the end of the partitioning stage is calculated based on the martensite start temperature (M_s) detected during the final quench by dilatometry and using [44]:

$$M_s = 545 \text{ }^\circ\text{C} - 601.2 \text{ }^\circ\text{C} \cdot \left(1 - \exp\left(\frac{-0.868}{\text{wt. \%}} \cdot x_C\right)\right) - 34.4 \frac{^\circ\text{C}}{\text{wt. \%}} \cdot x_{Mn} \quad (4.5)$$

where x_C and x_{Mn} are the concentrations of carbon and manganese in austenite (wt. %).

Table 4.3 shows the carbon content of austenite at the end of isothermal holding at 400 °C, 500 °C and 600 °C, determined from the 2D phase-field simulations and experiments. At the end of partitioning at 400 °C and 500 °C, the 2D phase-field simulations indicate a higher carbon concentration in austenite when compared to that of experiments. This is because the simulations do not consider additional reactions that might take place during the partitioning stage. For instance, microstructural observations from Chapter 3 show significant carbide precipitation in martensite at 400 °C and pearlite formation during partitioning at 500 °C. Carbide and pearlite formation consume part of the carbon available for partitioning and volume fraction of austenite, leading to a lower concentration of carbon in austenite than that predicted by the simulations. After partitioning at 600 °C, it is observed that austenite reversion results in a decreased amount of carbon in the austenite grain due to redistribution. In the absence of competitive reactions (as in phase-field modelling), austenite is enriched with a higher concentration of carbon by the end of partitioning stage than if competitive reactions do occur. This makes austenite more stable during the final quench, reducing M_s close to room temperature.

Table 4.3. Average carbon content (in wt. %) of austenite at the end of partitioning stage determined from phase field modelling and experiments (Equation 4.5).

Partitioning conditions	Carbon concentration in austenite (wt. %)					
	400 °C		500 °C		600 °C	
	PFM	Experiment	PFM	Experiment	PFM	Experiment
60 s	-	-	-	-	0.95	0.55
180 s	-	-	0.88	0.53	-	-
300 s	0.88	0.33	-	-	0.64	0.46
900 s	-	-	0.82	0.47	-	-
3600 s	0.90	0.41	-	-	-	-

To summarise, in the investigated alloy, the effective stabilisation of austenite during the Q&P process is possible by applying higher partitioning temperatures at which local partitioning of substitutional elements and interface migration (austenite reversion) are feasible. However, as observed from Chapter 2, it is not possible to completely avoid competitive reactions during the partitioning stage, the current observations from phase-field modelling help to quantify to which extent the occurrence of such reactions can negatively influence the stabilisation of austenite.

4.5.3. Impact of Grain Size on Carbon Partitioning

An interesting observation from the concentration profiles at partitioning temperature of 400 °C (Figure 4.8) is the presence of an asymmetric carbon concentration profile across segment A-B. When a martensitic grain is surrounded by austenite grains the local equilibrium near α/γ interfaces will be different. This leads to different elemental concentrations near each interface. The same phenomenon is observed at 500 °C and 600 °C, but at shorter time intervals.

Figure 4.14a, 4.14b, and 4.14c show the carbon concentration at the centre of 195 different austenite grains, varying between 300 nm and 5 μm in diameter, after different partitioning conditions: 3600 s at 400 °C, 900 s at 500 °C and 300 s at 600 °C. The black solid line represents the trend of carbon concentration with the austenite grain size. A strong scatter in the carbon concentration of austenite grains in the microstructure is observed by the end of partitioning stage at 400 °C and 600 °C when compared to 500 °C. At the partitioning temperature of 400 °C, it is observed that the austenite grains of similar size (300 nm - 3 μm) are enriched with different carbon concentrations. This effect originates from the size and morphology of the surrounding martensite grains. Austenite grains enriched with higher carbon concentrations are observed to be surrounded by larger martensite grains, which make a higher amount of carbon available to partition than from smaller martensite grains. Austenite grains that display a lower carbon concentration seem to be surrounded by smaller martensite grains.

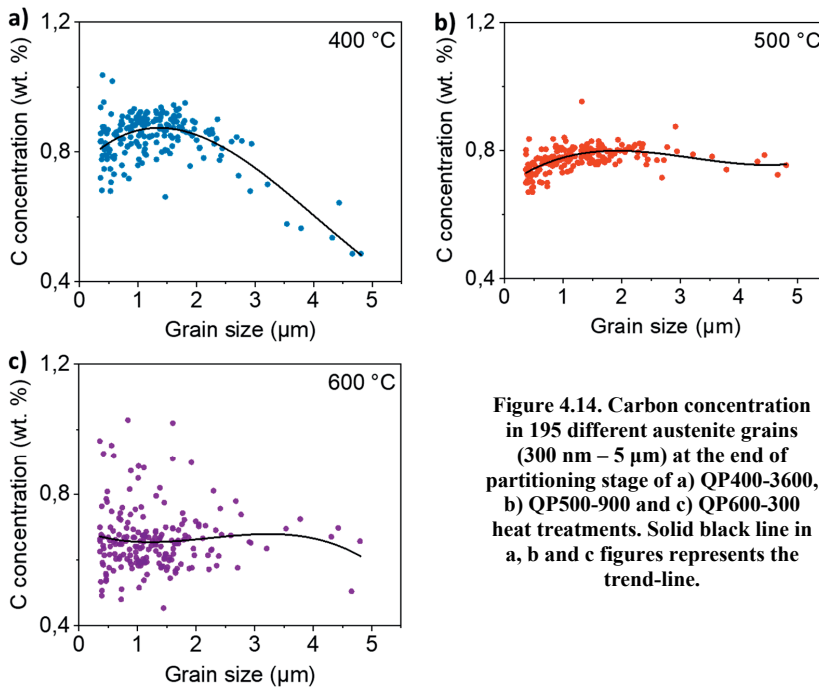


Figure 4.14. Carbon concentration in 195 different austenite grains (300 nm – 5 μm) at the end of partitioning stage of a) QP400-3600, b) QP500-900 and c) QP600-300 heat treatments. Solid black line in a, b and c figures represents the trend-line.

During the partitioning stage at 500 °C, due to the faster diffusion kinetics of carbon at 500 °C than at 400 °C, austenite grains enrich in carbon in the initial few seconds of isothermal holding, which is followed by a continuous carbon redistribution. Hence, irrespective of their size, most of the austenite grains attain a relatively homogeneous carbon concentration at the end of partitioning stage. After 300 s of partitioning at 600 °C, the carbon distribution in austenite grains is scattered between 0.43 and 1.02 wt.% carbon which could be due to redistribution of carbon as a result of continuous growth of austenite grains in the microstructure. Moreover, the average carbon concentration (around 0.7 wt. %) is lower than in the case of 400 °C and 500 °C. The reason for lower average carbon concentration when compared to that at 400 °C and 500 °C is the decrease of the equilibrium carbon concentration of austenite with increasing temperature. The above observations indicate that not only the partitioning conditions but also the morphology of the austenite grains and the surrounding martensite grains, after the initial quench, significantly influence the carbon distribution in the microstructure during the partitioning stage.

4.6. Conclusions

In this chapter, the partitioning kinetics of carbon and manganese during isothermal holding in a Q&P processed Fe-0.2C-6.0Mn (wt. %) steel (alloy *Mn* from Chapter 3) is investigated using multi-phase field modelling (MICRESS) and 3D Atom Probe Tomography experiments. Partitioning temperatures of 400 °C, 500 °C and 600 °C for times up to 3600 s are studied. The conclusions obtained are:

- Observations from 2D simulations at 400 °C and 500 °C show that multiple austenite grains compete for the carbon from the same martensite grain lying in between. Hence, asymmetric carbon concentration profiles develop at the α/γ interfaces of single austenite grain. This leads to continuous carbon redistribution among the austenite grains through the martensite grains.
- During partitioning at 600 °C, due to asymmetric carbon concentration profiles developed at α/γ interfaces, a local equilibrium is established resulting in movement of α/γ interfaces of a single austenite grain at different partitioning times. Hence, not only partitioning conditions but also the size and spatial distribution of grains, after the initial quench, influence the carbon distribution on the microstructure during the partitioning stage.
- 1D simulations at 600 °C show that, apart from elemental concentration gradients from the equilibrium concentrations, austenite and martensite grain sizes along with surrounding microstructure play a crucial role in the extent of α/γ interface movement. The smaller the austenite grain size, the faster the equilibration of alloying elements at the α/γ interface is, which lead to development of lower driving force, resulting in less α/γ interface migration when compared to bigger grains.
- Observations from the APT experiment and the simulations show that interface migration and manganese partitioning are simultaneous phenomena during partitioning at 600 °C for 300 s. The reverted austenite is enriched with a manganese concentration higher than the nominal concentration due to migration of the α/γ interface being effectively faster than the manganese diffusion. This can be a strategy to stabilise higher volume fraction of retained austenite in the final microstructure.

The results from this chapter show that the effective stabilisation of austenite in the final Q&P microstructure is possible by applying higher partitioning temperatures at which local partitioning of substitutional elements and interface migration (austenite reversion) are feasible.

References

- [1]. J.G. Speer, D.K. Matlock, B.C. De Cooman, J.G. Schroth, **Carbon partitioning into austenite after martensite transformation**. Acta Materialia, 51(9) (2003), pp. 2611-2622.
- [2]. N. Zhong, X. Wang, Y. Rong, L. Wang, **Interface migration between martensite and austenite during quenching and partitioning (Q&P) process**, Journal of Materials Science and Technology, 22 (2006), pp. 751-754.
- [3]. J.G. Speer, R.E. Hackenberg, B.C. De Cooman, D.K. Matlock, **Influence of interface migration during annealing of martensite/austenite mixtures**, Philosophical Magazine Letters, 87 (2007), pp. 379.

- [4]. M.J. Santofimia, L. Zhao, J. Sietsma, **Model for the interaction between interface migration and carbon diffusion during annealing of martensite–austenite microstructures in steels**, Scripta Materialia, 59 (2008), pp. 159-162.
- [5]. Y. Takahama, M.J. Santofimia, M.G. Meozzi, L. Zhao, J. Sietsma, **Phase field simulation of the carbon redistribution during the quenching and partitioning process in a low-carbon steel**, Acta Materialia, 60 (2012), pp. 2916-2926.
- [6]. D. De Knijf, M.J. Santofimia, H. Shi, V. Bliznuk, C. Föjer, R. Petrov, W. Xu, **In situ austenite–martensite interface mobility study during annealing**, Acta Materialia, 90 (2015), pp. 161-168.
- [7]. S.Y.P. Allain, G. Geandier, J.C. Hell, M. Soler, F. Danoix, M. Gouné, **Effects of Q&P processing conditions on austenite carbon enrichment studied by in situ high-energy X-ray diffraction experiments**, Metals, 7 (2017), pp. 232-244.
- [8]. S.Y.P. Allain, G. Geandier, J.C. Hell, M. Soler, F. Danoix, M. Gouné, **In-situ investigation of quenching and partitioning by High Energy X-Ray Diffraction experiments**, Scripta Materialia, 131 (2017), pp. 15-18.
- [9]. T.D. Bigg, D.V. Edmonds, E.S. Eardley, **Real-time structural analysis of quenching and partitioning (Q&P) in an experimental martensitic steel**, Journal of Alloys and Compounds, 577 (2013), pp. S695-S698.
- [10]. E.J. Seo, L. Cho, Y. Estrin, B.C. De Cooman, **Microstructure-mechanical properties relationships for quenching and partitioning (Q&P) processed steel**, Acta Materialia, 113 (2016), pp. 124-139.
- [11]. E.J. Seo, L. Cho, B.C. De Cooman, **Kinetics of the partitioning carbon and substitutional alloying elements during quenching and partitioning (Q&P) processing of medium Mn steel**, Acta Materialia, 107, (2016), pp. 354-365.
- [12]. Y. Toji, H. Matsuda, M. Herbig, P.P. Choi, D. Raabe, **Atomic-scale analysis of carbon partitioning between martensite and austenite by atom probe tomography and correlative transmission electron microscopy**, Acta Materialia, 65 (2014), pp. 215-228.
- [13]. M.J. Santofimia, L. Zhao, I. Povstugar, P.P. Choi, D. Raabe, J. Sietsma, **Carbon redistribution in a quenched and partitioned steel analysed by atom probe tomography**, in Proc 3rd int symp steel sci (ISSS 2012), N.H. Furuhashi T, Ushioda K, Editor. 2012: Kyoto: The Iron and Steel Institute of Japan. pp. 155.
- [14]. X. Zhu, W. Li, H. Zhao, L. Wang, X. Jin, **Hydrogen trapping sites and hydrogen-induced cracking in high strength quenching & partitioning (Q&P) treated steel**, International journal of Hydrogen Energy, 39 (2014), pp. 13031-13040.
- [15]. M. Gouné, S. Aoued, F. Danoix, G. Geandier, A.Q. Poulon, J.C. Hell, M. Soler, S.Y.P. Allain, **Alloying-element interactions with martensite/austenite interface during quenching and partitioning of a model Fe-C-Mn-Si alloy**, Scripta Materialia, 162 (2019), pp. 181-184.
- [16]. R. Ding, Z. Dai, M. Huang, Z. Yang, C. Zhang, H. Chen, **Effect of pre-existed austenite on austenite reversion and mechanical behaviour of an Fe-0.2C-8Mn-2Al medium Mn steel**. Acta Materialia, 147 (2018), pp. 59-69.
- [17]. N. Zhong, X. Wang, Y. Rong, L. Wang, **Interface migration between martensite and austenite during quenching and partitioning (Q&P) process**, Journal of Materials Science and Technology, 22 (2006), pp. 751-754.

- [18]. J.G. Speer, R.E. Hackenberg, B.C. De Cooman, D.K. Matlock, **Influence of interface migration during annealing of martensite/austenite mixtures**, *Philosophical Magazine Letters*, 87 (2007), pp. 379.
- [19]. M.J. Santofimia, L. Zhao, J. Sietsma, **Model for the interaction between interface migration and carbon diffusion during annealing of martensite–austenite microstructures in steels**, *Scripta Materialia*, 59 (2008), pp. 159-162.
- [20]. Y. Takahama, M.J. Santofimia, M.G. Meozzi, L. Zhao, J. Sietsma, **Phase field simulation of the carbon redistribution during the quenching and partitioning process in a low-carbon steel**, *Acta Materialia*, 60 (2012), pp. 2916-2926.
- [21]. H. Chen, S. van der Zwaag, **Predicting the effect of Mo, Ni, and Si on the bainitic stasis**, *Metallurgical and Materials Transaction A*, 45 (2014), pp. 3429-3437.
- [22]. H. Chen, S. van der Zwaag, **The effect of interfacial element partitioning on ferrite and bainite formation**, *The Member Journal of The Minerals, Metals & Materials Society*, 68 (2016), pp. 1320-1328.
- [23]. H.W. Luo, C.H. Qiu, H. Dong, J. Shi, **Experimental and numerical analysis of influence of carbide on austenitisation kinetics in 5Mn TRIP steel**, *Materials Science and Technology*, 30 (2014), pp. 1367-1377.
- [24]. Z. Dai, R. Ding, Z. Yang, C. Zhang, H. Chen, **Elucidating the effect of Mn partitioning on interface migration and carbon partitioning during Quenching and Partitioning of the Fe-C-Mn-Si steels: Modeling and experiments**, *Acta Materialia*, 144 (2018), pp. 666-678.
- [25]. K. Thompson, J. Sebastian, S. Gerstl, **Observations of Si field evaporation**, *Ultramicroscopy*, 107 (2-3) (2007), pp. 124-130.
- [26]. I. Steinbach, F. Pezzolla, B. Nestler, M. Seesselberg, R. Prieler G.J. Schmitz, J.L.L. Rezende, **A phase field concept for multiphase systems**. *Physica D: Nonlinear Phenomena*, 94(3) (1996), pp. 135-147.
- [27]. J. Eiken, B. Bottger, I. Steinbach, **Multiphase-field approach for multicomponent alloys with extrapolation scheme for numerical application**. *Physical Review E*, 73(62) (2006), pp. 066122.
- [28]. J. Eiken, **A Phase-field Model for Technical Alloy Solidification**, Ph.D. thesis, RWTH Aachen University (2010).
- [29]. www.MICRESS.de.
- [30]. M.G. Meozzi, J. Eiken, J. Sietsma, S. Van der Zwaag, **Phase field modelling of microstructural evolution during the quenching and partitioning treatment in low-alloy steels**, *Computational Materials Science* 112 (2016), pp. 245-256.
- [31]. J. Ågren, **A revised expression for the diffusivity of carbon in binary Fe-C austenite**, *Scripta Metallurgica*, 20(11) (1986), pp. 1507-1510.
- [32]. B. Jansson, **Carbon and Nitrogen diffusion in bcc Cr-Fe-Ni**, *Zeitschrift fuer Metallkunde*, 85, 1994, pp. 498-501.
- [33]. Landholt-Bornstein, **Diffusion in Solid Metals and Alloys**, 26, Editor: H. Mehrer, springer (1990).

- [34]. A. Borgenstam, L. Hoglund, J. Agren, A. Engstrom, **DICTRA, a tool for simulation of diffusional transformations in alloys**, *Journal of Phase Equilibria*, 21 (2000), pp. 269.
- [35]. C. Celada-Casero, C. Kwakernaak, J. Sietsma, M.J. Santofimia, **The influence of the austenite grain size on the microstructural development during quenching and partitioning processing of a low-carbon steel**, *Materials and Design*, 178 (2019) pp. 107847.
- [36]. G.P. Krielaart, S. Van der Zwaag, **Kinetics of $\gamma \rightarrow \alpha$ phase transformation in Fe-Mn alloys containing low manganese**, *Materials Science and Technology*, 14 (10) (1998), pp. 10-18.
- [37]. M.G. Meozzi, J. Sietsma, S. Van der Zwaag, **Analysis of $\gamma \rightarrow \alpha$ transformation in a Nb microalloyed C-Mn steel by phase field modelling**, *Acta Materialia*, 54 (2006), pp. 1431-1440.
- [38]. W.F. Lange, M. Enomoto, H. I. Aaronson, **The kinetics of ferrite nucleation at austenite grain boundaries in Fe-C alloys**, *Materials Transaction A*, 19 (1988), pp. 427-440.
- [39]. M.G. Meozzi, **Phase field modelling of the austenite to ferrite transformation in steels**, Ph.D. thesis, Delft University of Technology (2007).
- [40]. C. Atkinson, T. Akbay, R.C. Reed, **Theory for reaustenitisation from ferrite/cementite mixtures in Fe-C-X steels**, *Acta Metallurgica et Materialia*, 43 (5) (1995), pp. 2013-2031.
- [41]. C.A. Apple, R.N. Caron, G. Krauss, **Packet microstructure in Fe-0.2 pct C martensite**, *Metallurgical Transactions A*, 5 (1974), pp. 593-599.
- [42]. T. Swarr, G. Krauss, **The effect of structure on the deformation of as-quenched and tempered martensite in an Fe-0.2 pct C alloy**, *Metallurgical Transactions A*, 7A (1976), pp. 41-48.
- [43]. T. Philippe, M. Gruber, F. Vurpillot, D. Blavette, **Clustering and local magnification effects in atom probe tomography: a statistical approach**, *Microscopy and Microanalysis*, 16 (2010), pp. 643-648.
- [44]. D. Barbier, **Extension of the Martensite Transformation Temperature relation to Larger Alloying Elements and Contents**, *Advanced Engineering Materials*, 16(1) (2013), pp. 122-127.

5

In-situ Magnetometry and Dilatometry Investigation of Austenite Evolution during Quenching and High-Temperature Partitioning Process in a Medium-Mn Steel

In quenching and partitioning (Q&P) steels, the precise control of retained austenite and martensite is of paramount interest to attain a good balance between ductility and strength. Ex-situ and in-situ magnetisation techniques have been proven to be effective and precise for the quantification of the volume fraction of austenite in steels at room temperature and during the application of heat treatments, respectively. In this chapter, in-situ magnetisation measurements in a vibrating sample magnetometer (VSM) are performed to study the evolution of the austenite fraction during Q&P cycles in a 0.19C-6.0Mn-2.1Ni (in wt. %) steel. Magnetisation investigations are furthermore compared with dilatometer and X-ray diffraction measurements. Partitioning temperatures of 400 °C, 500 °C and 600 °C for times up to 1800 s are studied. The in-situ magnetic measurements allow us to decouple the evolution of austenite from the other competitive reactions occurring during the partitioning stage. From this study, it is drawn that the in-situ magnetometry can be a quicker and more effective (bulk) technique than dilatometry for the precise tracking of the evolution of the austenite volume fraction during a heat treatment. Nevertheless, some considerations need to be taken into account: 1) the size limitation of the VSM specimens to cubes of 2 mm in side leads to a large surface-area-to-volume ratio that favours an early initiation of martensite transformation during cooling, and 2) the application of a constant magnetic field during the thermal processing might influence the phase transformation temperatures, which would make the microstructure evolution somewhat different from that undergone during dilatometry experiments.

**This chapter is based on: S. Ayenampudi, C. Celada-Casero, N. Geerlofs, J. Sietsma, and M. J. Santofimia: In-situ Magnetometry and Dilatometry Investigation of Austenite Evolution during Quenching and Partitioning Process in a Medium-Mn Steel. To be submitted for publication.*

5.1. Introduction

Stabilizing austenite in the final microstructure is of paramount interest in Q&P steels, as retained austenite primarily contributes to the ductility of the material. Investigations from Chapter 2 and 3 show that the volume fraction of austenite present in the material after the initial quench strongly influences the competitive reactions occurring during the partitioning stage of the Q&P process. In this view, the effective and precise tracking of the austenite volume fraction during the Q&P process is very important to optimise the thermal cycles.

Earlier research utilised ex-situ and in-situ measuring techniques or a combination of both to track the evolution of austenite volume fraction during a thermal process [2-6]. Ex-situ measuring techniques like X-Ray diffractometry (XRD), magnetometry, and electron backscattered diffraction (EBSD) have been used for the quantitative determination of phase volume fractions in the final Q&P microstructures [2-3]. In addition to dilatometry [4-6], various in-situ measuring techniques, such as in-situ neutron diffraction [7], in-situ TEM [8], and in-situ high energy X-Ray diffraction [9-11], have been employed to track the microstructure evolution during the partitioning stage of the Q&P process. However, factors such as stresses developed within the sample during sample preparation (EBSD), sensitivity to texture and limited measuring depth (X-ray diffraction), limit the accuracy of the measured phase fractions. Moreover, some of the in-situ techniques mentioned above have limitations in terms of the time-consuming complex data analysis and expensive procedures [12].

Magnetic techniques have been proven to be effective for accurate determination of the austenitic phase fractions in bulk materials. Both ex-situ and in-situ magnetic techniques are widely used to study phase fractions at room temperature via saturation magnetisation measurements [12-16] and to investigate evolution of phase fractions in low-carbon steels during a thermal process [17-25], respectively. Since saturation magnetisation depends only on the volume fraction of the ferromagnetic phases present in the specimen, their chemical composition and the temperature, it is considered a relatively accurate technique to measure the volume fraction of austenite at room temperature [12, 26-27]. The evolution of the austenite volume fraction at different temperatures by in-situ measurement can also be measured if the temperature-dependent magnetic saturation of the austenite-free sample of same alloy is known [28-35]. Very recently, Filho *et al.* [24] studied the austenite reverse transformation in a 17.6 wt.% Mn steel via in-situ magnetic technique and observed that austenite nucleation and growth is governed by strong elemental partitioning. The two-stage austenite reversion, detected based on the Curie temperature (T_c), is due to manganese concentration differences in the austenite grains. These measurements were observed to be in very close agreement with the analysis based on APT experiments and DICTRA simulations. In their study, Bojack *et al.* [28-29] used in-situ magnetic technique to study the evolution of austenite and martensite in a stainless steel during different thermal cycles. This study showed that in-situ magnetic measurements are helpful to study the evolution of austenite during heat treatments in multi-phase steels. Quenching and partitioning steels also involve a multi-phase

microstructure and precise tracking of austenite volume fraction during Q&P processing is challenging. Therefore, based on the above arguments, in-situ magnetisation is potentially an effective technique to study the Q&P process.

In this chapter, an in-situ magnetisation technique is used to analyse the microstructure evolution, and especially the evolution of austenite volume fraction, in a medium manganese steel during the Q&P process. Magnetisation experiments are supported by a combination of dilatometry and X-Ray diffraction (XRD) measurements.

5.2. Material, Heat Treatments and Experimental Methods

A 0.19C-6.0Mn-2.1Ni (wt.%) steel (alloy *MnNi* from the Chapter 3) is investigated. From ThermoCalc (database TCFE9), the A_{e1} and A_{e3} temperatures of the current alloy are calculated to be around 400 °C and 675 °C, respectively. The initial microstructure, shown in Figure 5.1, displays a mixture of bainite and martensite.

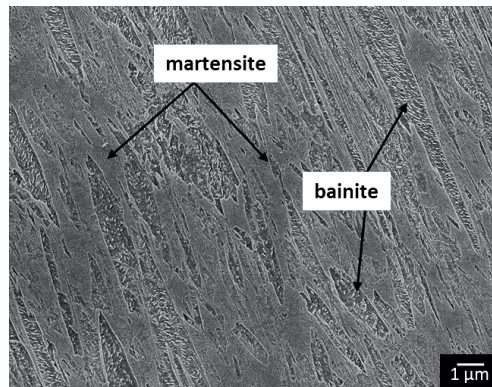


Figure 5.1. Scanning Electron Microscopy micrograph of the material before Q&P heat treatment.

A schematic diagram of the Q&P thermal cycles applied to the studied alloy is shown in Figure 5.2. The microstructural evolution during the thermal cycles is analysed using two techniques: in-situ magnetisation experiments in a vibrating sample magnetometer (VSM) and dilatometry. The sample is initially heated to 790 °C to achieve a fully austenitic microstructure. After 120 s of isothermal holding the steel is cooled down to a temperature where the microstructure consists of 0.75/0.25 volume fractions of martensite/austenite. Then, the sample is heated to a partitioning temperature of 400 °C, 500 °C or 600 °C and isothermally held for up to 1800 s. Based on the observations in Chapter 3 on the same alloy, in order to avoid competitive reactions, such as pearlite and carbide precipitation in austenite during the partitioning stage, shorter holding times were selected at higher partitioning temperatures. Finally, the steel is cooled down to room temperature. Initially, all heat treatments were performed in the VSM and the information regarding the heating and cooling rates was extracted. The same heating and cooling parameters were later considered for the heat treatments applied in the dilatometer in order to ensure

that dilatometry measurements are consistent and comparable with the VSM measurements. This will be extensively discussed in the following sections.

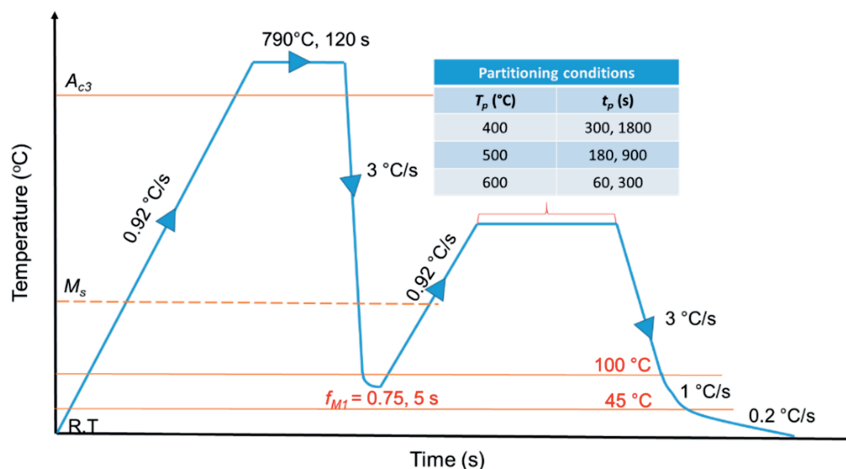


Figure 5.2. Schematic representation of Q&P thermal cycles applied in the present work.

5.2.1. Magnetic Measurements

A 7307 vibrating sample magnetometer (VSM) equipped with a furnace was used to perform magnetisation measurements. Cubic specimens with an edge dimension of 2.0 mm were used. A standard NIST (National Institute of Standards and Technology) nickel specimen was used for calibration. Ex-situ magnetic measurements were performed by varying the applied magnetic field between -1.6 T and 1.6 T in steps of 0.1 T. Ex-situ measurements were performed to analyse the volume fraction of austenite present at room temperature, in the initial, as-quenched and Q&P heat-treated samples. In-situ magnetisation experiments were carried out under a constant magnetic field of 1.6 T to analyse the evolution of volume fraction of austenite during the thermal cycles.

Figure 5.3a shows a schematic diagram representing the working principle of the VSM. In Figure 5.3a, the blue and red arrows indicate the direction of sample vibration and the direction of magnetic field, respectively. The sample is placed between two electromagnetic coils. When the sample is vibrated sinusoidally in time, perpendicular to the magnetic field, a voltage is induced in the pick-up coils. The magnetisation of the sample can be determined based on the induced voltage.

Figure 5.3b shows the sample set-up inside the magnetometer furnace. To avoid oxidation at higher temperatures an inert atmosphere is created inside the furnace chamber with helium gas. Low pressure in the order of 10^{-4} mbar is induced between the furnace walls to avoid heat loss to the surroundings during the heat treatments. As shown in Figure 5.3b, two thermocouples are installed in the set-up: the first thermocouple (TC-I) is placed 3 mm below the sample, to measure the sample temperature, and the second thermocouple (TC-II) on the furnace wall to measure the furnace temperature. The sample is placed inside an alumina sample holder which has a high thermal conductivity. The temperature loss

(conduction mode of heat transfer) across the thickness of the sample holder is calculated to be around 0.2 °C and 2 °C at room-temperature (25 °C) and at highest operating temperature (1000 °C), respectively. Since the heat loss through the alumina sample holder is very minimal, the sample temperature is considered to be the same as that recorded by TC-I. In this chapter, only the temperature detected by TC-I is reported.

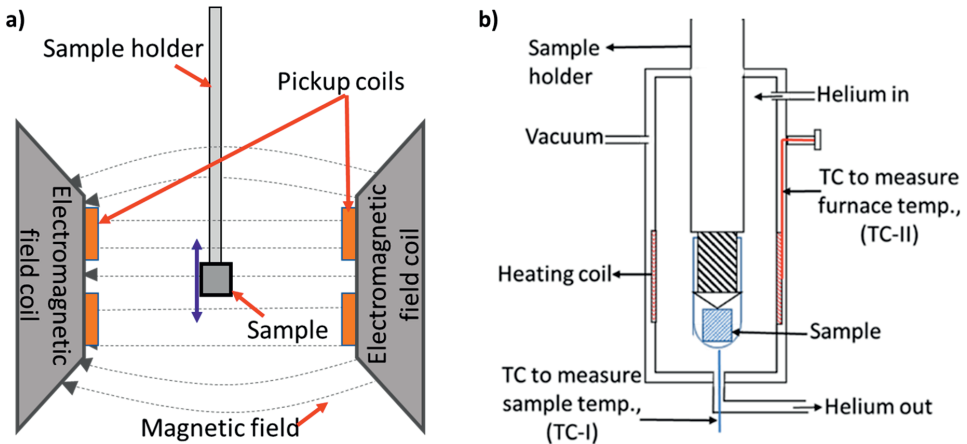


Figure 5.3. (a) Schematic representation of the working principle of the VSM (vibrating sample magnetometer). The blue and red arrow indicates the direction of sample vibration and the direction of magnetic field, respectively. (b) Sample set-up inside the furnace of the VSM. TC indicates thermocouple.

The heating and cooling parameters used for the in-situ magnetisation experiments are shown in Figure 5.2. An average heating rate of 0.92 °C/s was applied. During cooling, a constant helium flow rate of 50 l/min was used, resulting in the cooling rates shown in Figure 5.2. This is because as the furnace approaches room temperature during cooling, the difference between the surrounding temperature and the furnace temperature decreases. Therefore it takes much longer time to reach room temperature using in-situ magnetisation technique. Once the sample reaches an approximate temperature of 40 °C, the sample is taken out of the in-situ setup and air-cooled to room temperature. Later, ex-situ room temperature magnetic measurements were performed, on the same specimen, in order to determine the volume fraction of retained austenite at room temperature after respective heat treatment. Since the effect of temperature on sample expansion or contraction is only in the order of 100 microns, it is considered to be negligible in this study.

The volume fraction of austenite, f_{γ} , of the austenite-containing sample was determined from the magnetisation saturation, $M_{sat}(c)$, by relating it to the magnetisation of an austenite-free (ferromagnetic) reference sample of the same composition, $M_{sat}(ref)$, using [12]:

$$f_{\gamma} = 1 - \frac{M_{sat}(c)}{M_{sat}(ref)} \quad (5.1)$$

Chapter 5

An austenite-free reference sample of the same composition is required in order to determine the temperature-dependent magnetisation of a fully ferromagnetic sample. The temperature-dependent magnetisation of the austenite-free sample, $M_{ref}(T)$, was described by the relation of Arrott and Heinrich [30] up to A_{c1} temperature:

$$M_{ref}(T) = M_{sat0} \cdot \frac{(1-s)^\beta}{1-\beta s + A s^2 - C s^7} \quad (5.2)$$

where M_{sat0} is the saturation magnetisation at 0 K, β , A and C are material dependent constants, and $s = T/T_c$. T_c is the Curie temperature and can be obtained from the minimum of the first derivative of the magnetisation as a function of temperature [17]. Equation 5.2 is used to calculate the temperature-dependent saturation magnetisation $M_{ref}(T)$, which is necessary for calculating the austenite fraction at any temperature below T_c . ThermoCalc calculations shown in Figure 5.4 predict a maximum volume fraction of 0.03 of carbides precipitated in the current material under equilibrium. Due to their low volume fraction, the influence of carbides on the magnetisation is neglected.

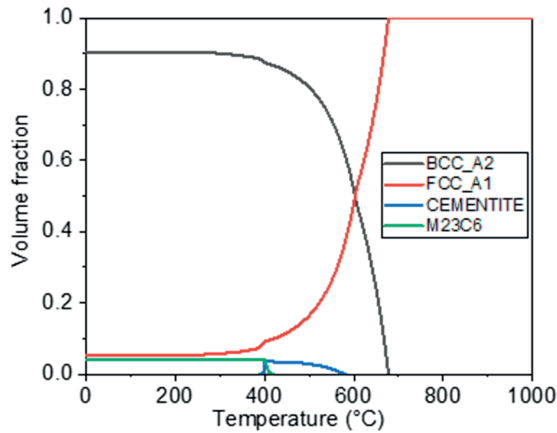


Figure 5.4. Equilibrium phase volume fractions diagram of the Fe-0.19C-5.0Mn-2.1Ni (wt.%) alloy, calculated using ThermoCalc (TCFE9), showing the evolution of equilibrium volume fraction of different phases with temperature. Here, M in $M_{23}C_6$ carbides refers to Fe, Mn.

5.2.2. Dilatometry

Cuboid specimens of $10 \times 4 \times 4 \text{ mm}^3$ were used for the Q&P heat treatments in a Bähr 805 DIL A/D dilatometer. A type-S thermocouple spot-welded on the surface of the specimen was used to monitor and control the temperature. A pressure in the order of 10^{-4} mbar was used during heating and during isothermal segments, while helium was used as the coolant. In order to maintain consistency with the magnetic measurements, similar thermal cycles (Figure 5.2), as applied in the magnetometer, are replicated in the dilatometer. In the dilatometry experiments, the sample temperature is directly measured from the thermocouple that is welded on the sample surface, unlike in the magnetometer, in which the sample temperature is measured from the thermocouple that is placed 3 mm below the sample.

5.2.3. Microstructural Characterisation

A JEOL JSM-6500F field emission gun scanning electron microscope (FEG-SEM) operating at 15 kV was used for microstructural investigation of the heat treated samples. Specimens were prepared for FEG-SEM observations following standard grinding, polishing and etching with Nital 2 %.

A Bruker type D8-Advance diffractometer was used to calculate the volume fraction (f_{RA}) of retained austenite in the dilatometry samples at room temperature. The diffraction angles covered during the measurements are in the range of $40^\circ < 2\theta < 130^\circ$, with Co $K\alpha$ radiation, where the $(110)\alpha$, $(200)\alpha$, $(211)\alpha$, $(220)\alpha$ and the $(111)\gamma$, $(200)\gamma$, $(220)\gamma$, $(311)\gamma$ peaks are covered within this 2θ range. A 0.042° 2θ step size with a counting per step of 3 s was used. Following the direct comparison method of austenite and martensite peaks suggested by Jatczak [35], the retained austenite volume fractions and the corresponding uncertainties were calculated. To determine the carbon concentration of retained austenite from its lattice parameter, the equations proposed by Dyson and Holmes [36] and van Dijk *et al.* [37] are combined and adjusted to befit the steel composition in the current work, resulting in:

$$a_\gamma = 3.556 \text{ \AA} + (0.0453 \frac{\text{\AA}}{\text{wt.\%}}) \cdot x_C + (0.00095 \frac{\text{\AA}}{\text{wt.\%}}) \cdot x_{Mn} + (0.00157 \frac{\text{\AA}}{\text{wt.\%}}) \cdot x_{Si} + (0.0006 \frac{\text{\AA}}{\text{wt.\%}}) \cdot x_{Cr} - (0.0002 \frac{\text{\AA}}{\text{wt.\%}}) \cdot x_{Ni} \quad (5.3)$$

where x_i represents the concentration of the alloying element i in wt.%. The detection limit of the retained austenite fraction by X-ray diffraction is 0.01.

5.3. Results

5.3.1. Phase Transformation Temperatures

Reference Sample

An austenite-free reference sample was obtained by isothermally holding an Fe-0.19C-6.0Mn-2.1Ni sample at 950°C for 0.5 h followed by quenching to room temperature. Subsequently, in order to transform the remaining fraction of austenite, the sample was tempered for 0.5 h at 400°C and then quenched to -196°C using liquid nitrogen. X-ray diffraction measurements on this sample indicate that no retained austenite was present in the sample. To measure the magnetisation of the reference sample as a function of temperature in-situ measurements were performed. As shown in Figure 5.5a, the sample was heated to 900°C at 0.92°C/s and cooled to room temperature at 3°C/s . Figure 5.5b shows the experimental magnetisation versus temperature during heating of the reference sample and the fit with eq. (5.2). It can be seen that the magnetisation decreases with increasing temperature during heating, which is due to a decrease in magnetisation until zero as it approaches Curie temperature (T_c), and to austenite formation. Since austenite is paramagnetic the material gradually loses its ferromagnetism when austenite forms, starting at A_{c1} temperature [38]. The Curie temperature of the reference sample is measured to be $770 \pm 2^\circ\text{C}$, which is determined from the minimum of the dM/dT curve. Equation 5.2 is

fitted to the curve in Figure 5.5b, up to A_{c1} temperature of the reference sample, which is calculated to be around 640 ± 5 °C from dilatometry experiments, using the least-squares method in which the fitting parameters M_{sat0} , β and A were determined to be $201.4 \text{ A}\cdot\text{m}^2/\text{kg}$, 0.306 and 0.318, respectively. The parameter C is kept constant at 0.129 [30].

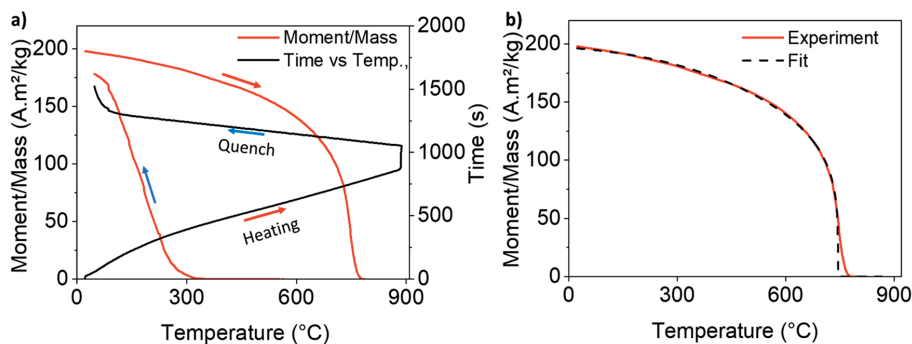


Figure 5.5. a) Thermal cycle applied on austenite-free reference sample and the magnetisation curve measured at 1.6 T, b) Magnetisation of austenite-free sample as a function of temperature together with the fit (dashed black line) for the reference magnetisation (red line).

As-quenched heat treatment

The as-quenched heat treatment was performed by heating the sample to 790 °C and then quenching it to room temperature after isothermally holding it for 120 s. The temperature-time profile during cooling follows an exponential trend, as shown in the final cooling stage of Figure 5.2. The magnetisation curve and dilatation curve of the as-quenched sample during heating and cooling of the austenitisation cycle are shown in Figure 5.6a. It can be seen that the magnetisation decreases with increasing temperature during heating, which results from the material approaching the Curie temperature and from the formation of paramagnetic austenite. The Curie temperature (T_C) is determined from the minimum of the dM/dT curve and is identified to be around 770 ± 2 °C, Figure 5.6b. It can be observed that the sample is completely austenitic at 790 °C where the magnetisation is zero. Figure 5.6c shows the evolution of the austenite fraction during heating in magnetometer and dilatometer. Since, the magnetisation curve fitting, based on Equation 5.2, is valid only until A_{c1} temperature of the sample, the evolution of austenite with temperature is also shown only until A_{c1} temperature which is 640 ± 5 °C. During cooling (Figure 5.6d), the material is paramagnetic until martensite starts to form, which is when the magnetisation sharply increases. The point where the magnetisation increases represents the martensite start temperature (M_s), which is found to be 292 ± 2 °C by magnetic measurements. Room temperature magnetic measurements determine the volume fraction of retained austenite in the as-quenched sample as 0.154 ± 0.003 . Using the temperature dependent magnetisation, extracted from the curve fitting in Figure 5.5b, the evolution of martensite volume fraction along with temperature is plotted in Figure 5.6d.

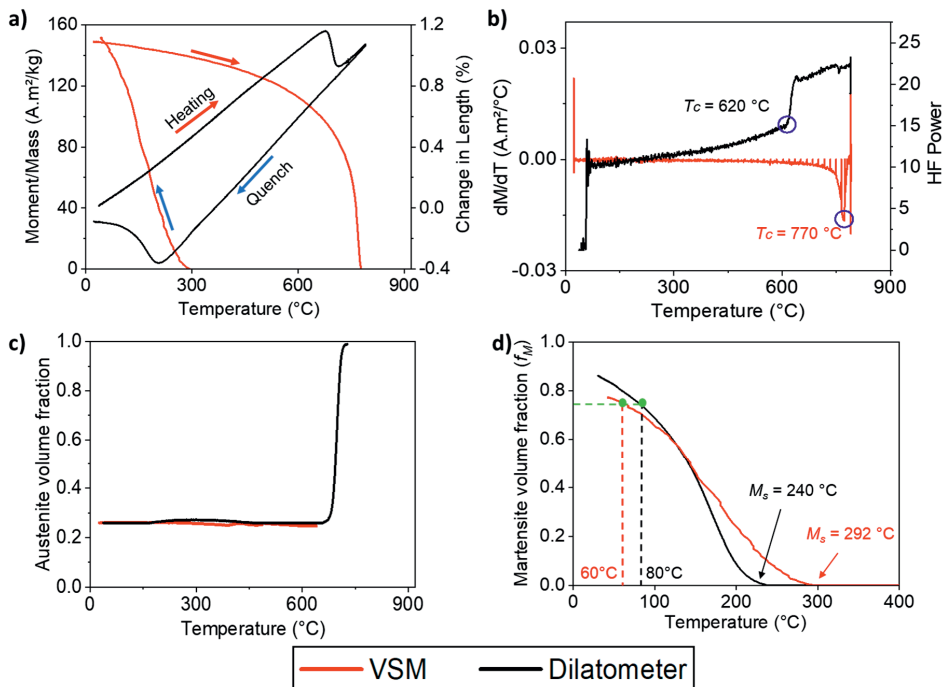


Figure 5.6. a) As-quench heat treatment applied on the initial material, b) dM/dT vs temperature (VSM) and HF (high frequency) power vs temperature (dilatometry) curves to identify Curie temperature (T_c). T_c is indicated by blue circles. c) evolution of austenite volume fraction with temperature during heating and c) evolution of martensite volume fraction with temperature during cooling. Red and black lines indicate the in-situ magnetisation data (VSM) and dilatometry data, respectively. Green dots indicate temperature corresponding to 0.75 volume fraction of martensite.

The A_{c1} and A_{c3} temperature of the initial material are determined from the dilatometry data of length (L) vs. temperature (T) using the dL/dT curve [39]. The Curie temperature of the steel is identified as the point where a sudden rise in the high frequency (HF) power is observed during heating [40]. The Curie temperature of the as-received sample measured by dilatometer is 620 ± 5 °C, Figure 5.6b, against the value of 770 ± 2 °C recorded from the magnetic measurements. The martensite start temperature (M_s) is identified as the temperature at which an increase in change in length of 0.01 volume fraction is observed during cooling, which is 240 ± 5 °C. A difference of 52 °C in martensite start temperature (M_s) exists between magnetic and dilatometry measurements. Table 5.1 shows the transformation temperatures observed from both VSM and dilatometry. Based on the X-ray diffraction measurements on dilatometry as-quenched sample, the volume fraction of retained austenite in the final microstructure is measured to be 0.15 ± 0.01 . A quenching followed by reheating heat treatment was performed to characterise the expansion behaviour of the quenched microstructure of the alloy. Using the same methodology as explained in Chapter 2, the evolution of martensite volume fraction along with temperature measured from dilatometer is plotted in Figure 5.6d. Based on the above information, for the planned Q&P heat-treatments, the initial quench temperatures that lead to formation of

austenite/martensite phase fractions of 0.25/0.75 are measured to be around 60 °C in magnetometer and 80 °C in dilatometer (indicated with a green dots in Figure 5.6d).

Table 5.1. Overview of Curie temperature and transformation temperatures of the initial material determined from magnetometer and dilatometer experiments.

Experiment	T_c	A_{c1}	A_{c3}	M_s
Magnetometer	770 ± 2 °C	-	-	292 ± 2 °C
Dilatometer	620 ± 5 °C	675 ± 5 °C	740 ± 5 °C	240 ± 5 °C

5.3.2. Quenching and Partitioning (Q&P) Heat Treatments

In this section, the results of the magnetisation and dilatometry measurements during quenching and partitioning for QP400-1800, QP500-900 and QP600-300 heat treatments will be addressed. Additional heat treatments, with intermediate partitioning times (QP400-900, QP500-300, QP600-60), were performed to assess the trend of retained austenite volume fraction with partitioning time.

In-situ Magnetisation Measurements

Figure 5.7 shows the evolution of magnetisation with time during QP400-1800, QP500-900 and QP600-300 heat treatments in the VSM. The solid black lines show the temperature vs time curves of respective heat treatments, whereas the dashed black lines show the evolution of magnetisation with time. The blue dot at the end of initial quench indicates the initial quench temperature (60 °C). During the reheating in the VSM, due to fluctuations in the input current, a slight jump in the heating rate is observed. However, as in the case of initial heating, the average heating rate during reheating stage is measured to be 0.92 °C/s.

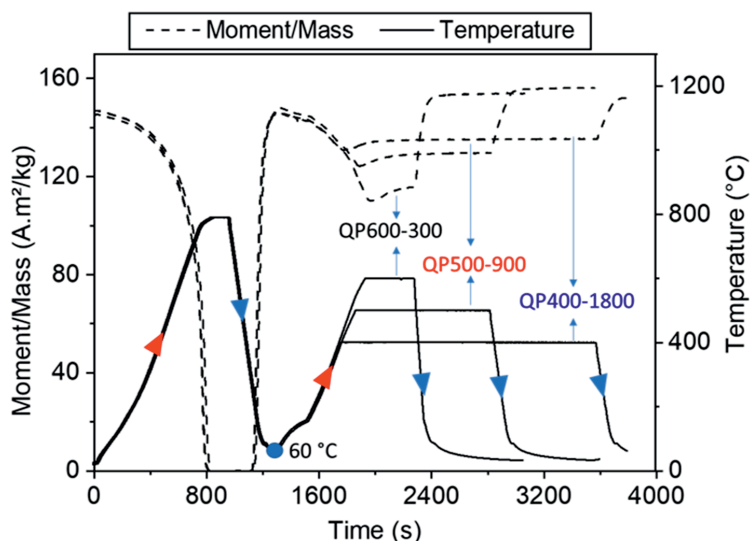


Figure 5.7. Representation of QP400-1800, QP500-900 and QP600-300 heat treatments carried out in VSM. Blue dot indicates the initial quench temperature.

Figures 5.8a, 5.8b and 5.8c show the volume fraction of austenite during the partitioning stage (black solid line) of QP400-1800, QP500-900, and QP600-300 heat treatments, respectively. The volume fraction of retained austenite in the final Q&P microstructure after respective heat treatments, measured by XRD, are indicated with red dots in the same images. The initial 30 s of the partitioning stage at all the three partitioning temperatures, where a slight expansion is observed, is neglected to eliminate the region over which a stable partitioning temperature is not achieved. A decrease in the volume fraction of austenite is observed at all three partitioning temperatures, indicating either martensite/austenite (α'/γ) interface movement towards austenite or austenite decomposition into pearlite or bainite. The rate of decrease in austenite volume fraction with partitioning time is observed to be lower with increasing partitioning temperature.

SEM micrographs of VSM specimens at the end of heat treatments QP400-1800, QP500-900 and QP600-300 are shown in Figure 5.9a, 5.9b and 5.9c, respectively. Carbide precipitation inside primary martensite is observed as a common feature in all conditions. The microstructure after partitioning at 400 °C for 1800 s appears like a typical Q&P microstructure with retained austenite films between primary martensite (M1) laths. After 900 s of partitioning at 500 °C, isolated pearlite colonies are observed in the final microstructure. Hence, the decrease in austenite volume fraction observed during partitioning at 500 °C can be related to pearlite formation. After partitioning at 600 °C, nanometric retained austenite films as well as spheroidised carbides inside primary martensite are also identified.

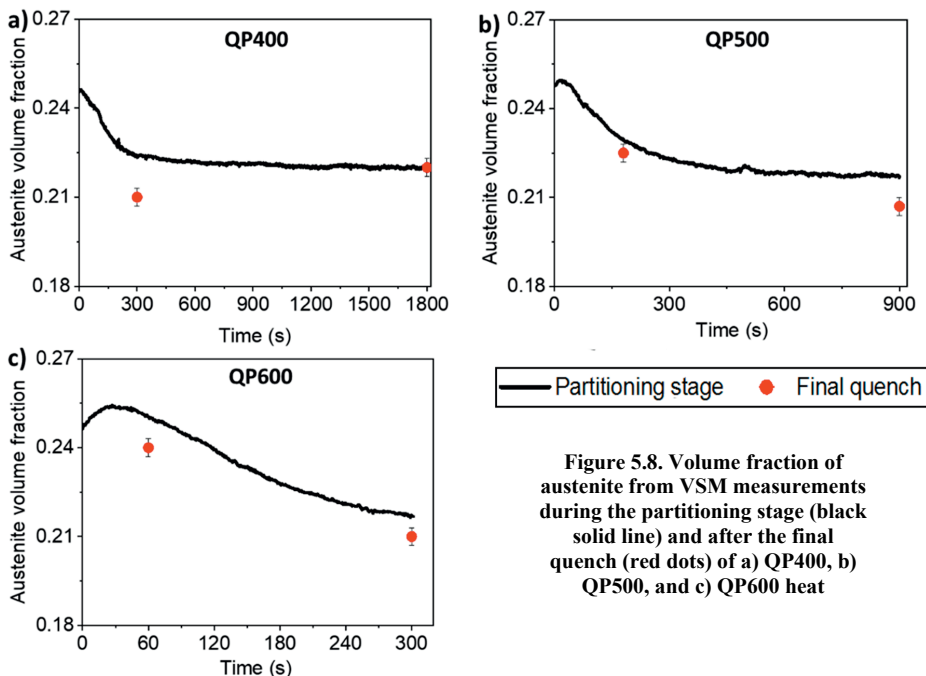


Figure 5.8. Volume fraction of austenite from VSM measurements during the partitioning stage (black solid line) and after the final quench (red dots) of a) QP400, b) QP500, and c) QP600 heat

From Figure 5.8a, 5.8b and 5.8c, a decrease in volume fraction of retained austenite in the final microstructure is observed with increasing partitioning time, except at partitioning temperature of

Chapter 5

400 °C. At all the partitioning temperatures, the volume fraction of austenite decreases with the increase of partitioning time and only a small volume fraction (≤ 0.02) of fresh martensite forms during the final quench. Hence, it can be interpreted that an additional reaction during the partitioning stage is consuming austenite.

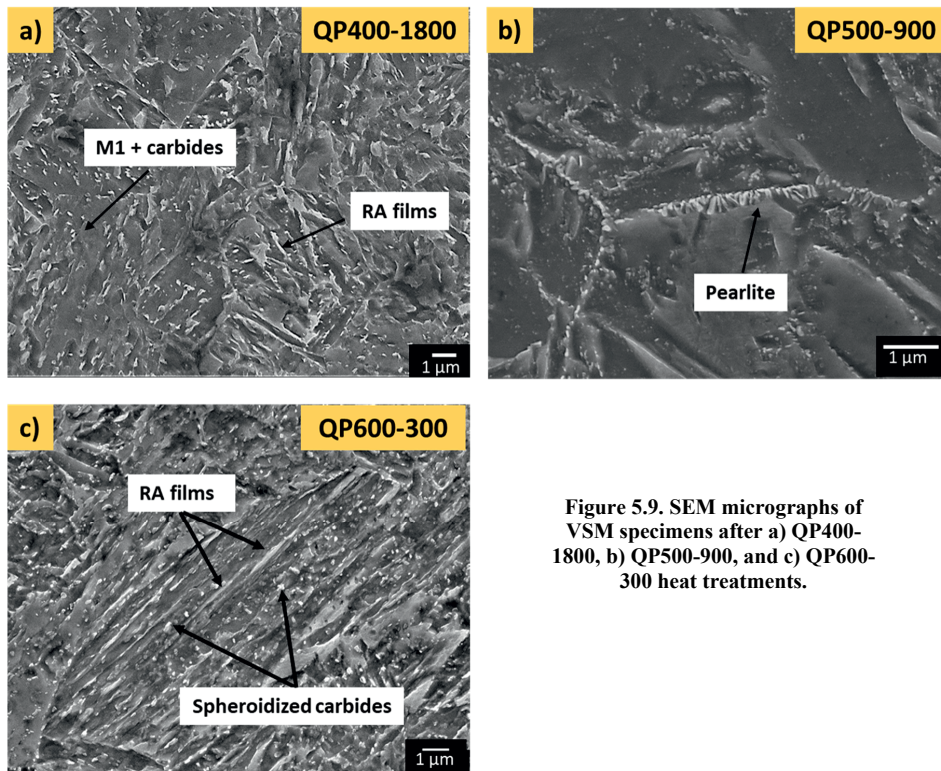


Figure 5.9. SEM micrographs of VSM specimens after a) QP400-1800, b) QP500-900, and c) QP600-300 heat treatments.

Dilatometry and X-ray diffraction

Figure 5.10 shows the change in length with temperature during QP400-1800, QP500-900 and QP600-300 heat treatments conducted in the dilatometer. Red and blue arrows indicated on the QP600-300 curve show the heating and cooling paths, respectively. Red and blue dashed lines indicate the austenitisation and the initial quench temperature, respectively.

Figures 5.11a, 5.11b and 5.11c show the change in length versus time plots (black curves) during partitioning stage of QP400-1800, QP500-900 and QP600-300 heat treatments and final volume fraction of retained austenite (red dots) after respective QP heat treatments. During partitioning at 400 °C, an initial dilatation is followed by a contraction. This indicates carbon partitioning from martensite to austenite [41] and carbide precipitation in primary martensite [42], respectively. At the partitioning temperature of 500 °C, a gradual contraction is observed and this behaviour is identified to be a consequence of precipitation of carbides in primary martensite. During partitioning at 600 °C, a strong

contraction is observed, which is related to austenite formation. The volume fraction of austenite formed by the end of the partitioning stage at 600 °C is determined following the procedure explained in Chapter 3, leading to a 0.06 ± 0.01 volume fraction after 300 s of isothermal holding.

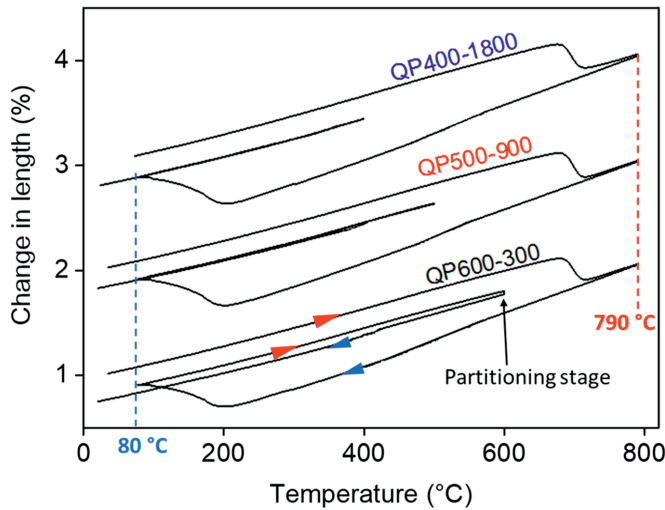


Figure 5.10. Representation of change in length vs temperature curves of QP400-1800, QP500-900 and QP600-300 heat treatments carried out in dilatometry.

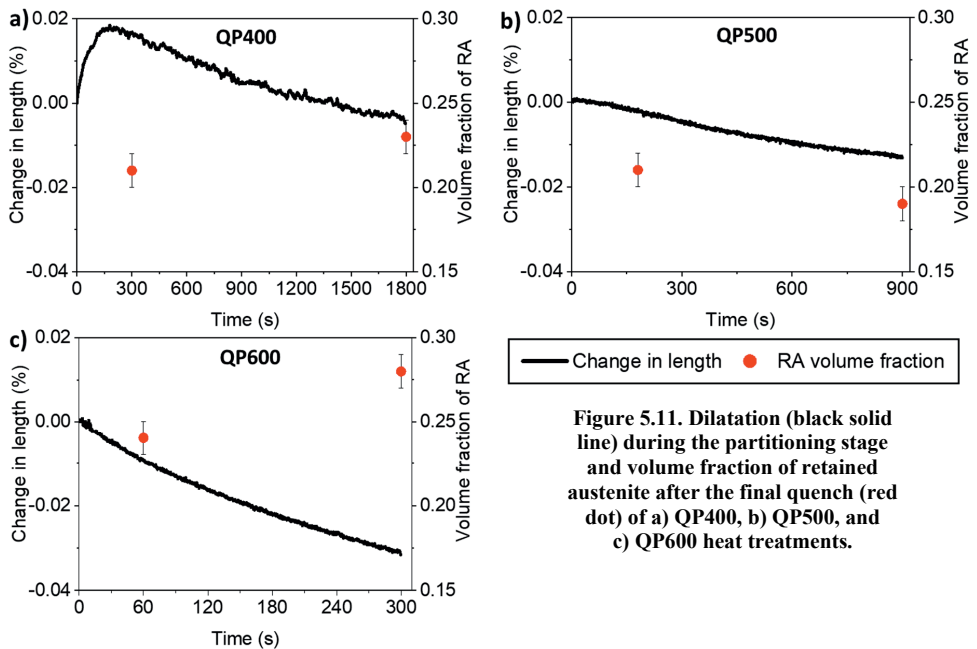


Figure 5.11. Dilatation (black solid line) during the partitioning stage and volume fraction of retained austenite after the final quench (red dot) of a) QP400, b) QP500, and c) QP600 heat treatments.

The volume fraction of retained austenite (RA) after the final quench given by the red dots in Figure 5.11, increases with isothermal holding time at partitioning temperatures of 400 °C and 600 °C. In contrast, an opposite trend is observed at the partitioning temperature of 500 °C. Since there are no

additional phase transformations observed during the partitioning stage at 500 °C, it can be interpreted that the decrease in the volume fraction of retained austenite with increasing partitioning time is due to occurrence of continuous carbide precipitation in primary martensite that consume the carbon available for partitioning from martensite to austenite. Hence, a fraction of austenite is not enriched with sufficient carbon which is transformed into fresh martensite during the final quench.

Figure 5.12a, 5.12b, and 5.12c show the SEM micrographs of dilatometer specimens after respective Q&P heat treatments. Retained austenite films, carbides precipitation in primary martensite and martensite/austenite islands are observed to be common features at all partitioning conditions. The final microstructure of QP600-300 heat-treated specimen also displays small islands of retained austenite between the primary martensite laths along with retained austenite films.

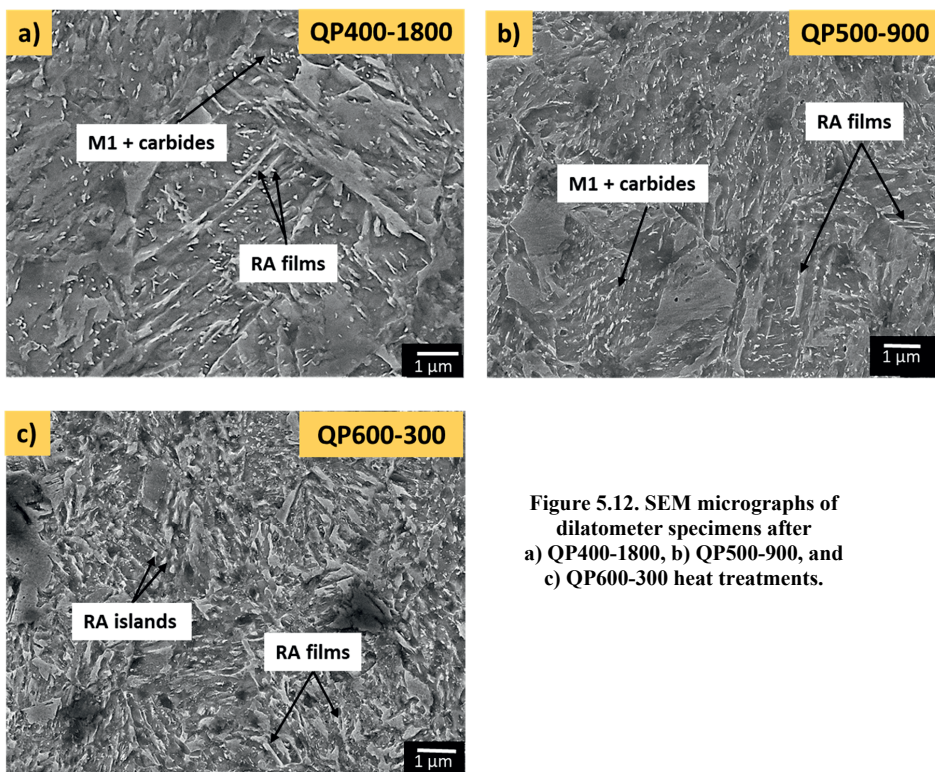


Figure 5.12. SEM micrographs of dilatometer specimens after a) QP400-1800, b) QP500-900, and c) QP600-300 heat treatments.

5.4. Discussion

The results from the in-situ magnetisation (VSM) measurements and from the dilatometry combined with X-Ray diffraction measurements give valuable information regarding phase transformations and microstructure evolution during the respective Q&P heat treatments. However, differences are observed between the two techniques (VSM and dilatometer) in terms of 1) Curie temperature, 2) martensite start

temperature (M_s), 3) microstructure evolution during the partitioning stage, and 4) final phase fractions. These differences are summarised in Table 5.1 and Table 5.2 and analysed in this section.

1. Curie Temperature

It is observed that the Curie temperature (T_c) determined from the VSM experiments is 150 °C higher than that from the dilatometry experiments. From the work of Liu *et al.* [43], calculations based on the Weiss molecular field theory indicate that the effect of 1.6 T magnetic field on the Curie temperature can be considered to be less than 1 °C, which is negligible with respect to the current differences observed. The concrete reason for the large difference is not known.

2. Martensite Start (M_s) Temperature

The M_s temperature of the sample measured from the VSM and the dilatometer is 292 ± 2 °C and 240 ± 5 °C, respectively, a difference of 52 °C. Considering the start temperature of martensite formation (240 °C) observed from dilatometry on the VSM curve (Figure 5.6d), almost 0.12 higher volume fraction of martensite is observed in the VSM sample when compared to the dilatometer sample. The factors contributing to this difference are:

a) In the earlier studies [44-45], it was reported that martensite transformation typically occurs at higher temperatures at the surface of the sample due to the lower driving force required for the martensitic transformation to occur at the surface when compared to the bulk. The surface-area-to-volume ratio of a VSM specimen is around 3 times larger than that of the dilatometry specimen, owing to the VSM specimen being much smaller. Considering that the surface effects will affect a depth equal to an average austenite grain size (d^p), which is in this case the first 25 μm from the surface towards the centre of the specimens, the total surface volume in which martensite forms can be quantified. Calculations show that the volume fraction of martensite transformed at the surface of the VSM specimen is around 7.5 % while that in dilatometer is only 2.5 %. Hence, the larger surface area-to-volume ratio of VSM specimen contributes to 5 % higher volume fraction when compared to that of the dilatometry specimen, in which martensitic transformation can occur. Moreover, due to the autocatalytic nature of the martensitic transformation the 7.5 % volume fraction at the surface could induce further transformation in the surroundings which in combination with the further increase in undercooling results in the continuous transformation as observed in VSM. Hence, the primary reason for the difference in M_s temperature is the larger surface-area-to-volume ratio of the VSM sample that leads to martensitic transformation at a higher temperature when compared to the dilatometer sample.

b) In addition, the presence of a magnetic field lowers the Gibbs free energy of the ferromagnetic martensite [34]. Therefore, a rise in M_s temperature is expected under the presence of a magnetic field. Satyanarayana *et al.* [47] experimentally showed that in a Fe-0.3C-2.8Ni-0.6Cr-0.6Mo (wt.%) alloy under the influence of 1.6 T the M_s temperature is increased by 5 °C, while Krivoglaz *et al.* [48] reported

a rise in M_s by 52 °C in the presence of a pulsating magnetic field of 35 T. Hence, only a small fraction of the rise in M_s by 52 °C can be ascribed to the influence of a magnetic field of 1.6 T.

Based on the above observations, it can be deduced that the higher M_s temperature observed from the VSM measurements is primarily due to the larger surface-area-to-volume ratio of the VSM specimen compared to the dilatometry specimen. The detection sensitivity of the dilatometer in the initial stage of phase transformations and the presence of a magnetic field are additional factors for the huge difference in the M_s temperature.

From Figure 5.6d, it is observed that, during the cooling, the kinetics of martensitic evolution in the VSM is slower than that in the dilatometer. Hence, a higher initial quench temperature is measured in the dilatometer (20 °C higher than that of VSM). This is because the higher undercooling in the case of dilatometer results in higher driving force for martensitic transformation, thereby resulting in a higher martensitic transformation rate. Moreover, the overlap in the volume fraction of martensite between VSM and dilatometry over a range of 30 °C (between 120 °C -150 °C) can be due to the higher undercooling resulting in faster martensitic transformation. Usually, in the presence of a magnetic field an additional magnetic driving force is induced and an increase in the rate of transformation is expected [34]. Since, in the current work, the applied magnetic field is only 1.6 T, the effect of magnetic field on rate of transformation is considered to be negligible.

3. Partitioning Stage

The reheating stage to the partitioning temperature is similar in the VSM and the dilatometer. Hence, at the beginning of the partitioning stage, the microstructure comprises a 0.250 ± 0.003 volume fraction of austenite in all samples. During the partitioning stage, differences were observed between the two techniques in terms of microstructural evolution and phase fractions. These differences are reported in the results section and summarised in Table 5.2.

The common observation at all the three partitioning temperatures is a decrease in austenite volume fraction at the beginning of the partitioning stage. At the beginning of the partitioning stage martensite reduces its carbon by three possible mechanisms:

- a) Carbon partitioning from martensite to austenite due to the chemical potential difference.
- b) Carbide precipitation in martensite.
- c) Interface movement towards austenite which could occur as a result of higher driving force for transformation present at the beginning of the isothermal holding stage.

Usually, in the dilatometry experiments, a phenomenon during the partitioning stage can be observed through a deviation (either increase or decrease) in the specimen's length. However, competitive phenomena during the partitioning stage are overlapping reactions, which can be dominant at different isothermal holding times. Hence, if multiple competitive phenomena occur during the partitioning stage,

it is difficult to isolate the effect of an individual phenomenon from the dilatometry experiments (Chapter 2). As can be observed from the SEM micrographs of both VSM and dilatometry specimens, carbide precipitation in martensite seems to be a dominant reaction. Therefore, it can be interpreted that the austenite decomposition/interface movement during the partitioning stage is occurring in both techniques but is not detected in the dilatometry experiments.

Table 5.2. Summary of phenomena observed during QP400-1800, QP500-900 and QP600-300 heat treatments performed in magnetometer and dilatometer techniques. Here, γ – austenite; α' – martensite; M1- primary martensite; RA – retained austenite; t_p – partitioning time.

	Partitioning stage		Final microstructure	
	Magnetometer	Dilatometer	Magnetometer	Dilatometer
QP400-1800	Rapid decomposition of γ followed by gradual decomposition of γ	Carbon partitioning from $\alpha' \rightarrow \gamma$ and carbide precipitation in M1.	<ul style="list-style-type: none"> • RA films + carbides. • Increase in RA with t_p. 	<ul style="list-style-type: none"> • RA films + carbides. • Decrease in RA with t_p.
QP500-900	γ decomposition due to pearlite formation.	Carbide precipitation in M1	<ul style="list-style-type: none"> • Pearlite • Decrease in RA with t_p. 	<ul style="list-style-type: none"> • RA films + carbides. • Decrease in RA with t_p.
QP600-300	Gradual decomposition of γ	Austenite reverse transformation	<ul style="list-style-type: none"> • RA films + carbides. • Decrease in RA with t_p. 	<ul style="list-style-type: none"> • Films and islands of RA • Increase in RA with t_p.

Based on the SEM micrograph, Figure 5.7a, it is understood that during the partitioning at 400 °C, no major competitive reactions like bainite, pearlite, or carbide precipitation in austenite are observed in either the VSM or the dilatometry specimen. Carbide precipitation in martensite is observed as a common feature in the final microstructure obtained from both the techniques.

At partitioning temperature of 500 °C, pearlite formation is observed from the VSM experiments and not from the dilatometry experiments. This is confirmed through the evolution of austenite during the partitioning stage (Figure 5.8b) and the SEM micrographs (Figure 5.9b). This difference can mainly be due to:

- a) The higher surface-area-to-volume ratio of the VSM sample, when compared to the dilatometry sample, could have favoured early pearlite formation in the VSM specimen.
- b) Based on DICTRA [52] calculations, the nose of the pearlite formation in a TTT diagram for the studied alloy is at a temperature around 440 °C. Observations from previous studies show that the presence of magnetic field can incur changes in the phase diagram [31-33]. Figure 5.13, adapted from the work of Zhang *et al.* [34], shows the Fe-C phase diagram and the shift in the equilibrium phase boundaries under the influence of a magnetic field of up to 12 T. Based on the theoretical calculations, for an Fe-0.19C wt.% steel (similar carbon content as the alloy studied in the current work) under 12 T,

a shift of A_{e3} and the eutectoid temperature by around 25 °C was observed. Extrapolating this for the magnetic field used in the current work, 1.6 T, would result in approximately 3 °C shift in the eutectoid temperature. This shift is calculated by not considering the influence of manganese and nickel which are present in the alloy studied in this work. Although the temperature shift due to 1.6 T seems to be only around 3 °C, it can be considered as an additional reason.

e) The presence of 1.6 T magnetic field can result in an accelerated and denser carbide precipitation [49-50]. SEM micrograph of the VSM specimen, Figure 5.9b, shows pearlite formation and significant carbide precipitation along the martensite/prior austenite grain boundaries. As discussed in Chapter 3, these interfaces are potential nucleation sites for carbide precipitation that initiate pearlite formation. Hence, this could be an additional reason for pearlite formation in the VSM specimen but not in the dilatometry specimen.

During partitioning at 600 °C continuous austenite reversion is not observed in the VSM but only in the dilatometer. A possible reason for this could be the shift of the ferrite + austenite ($\alpha + \gamma$) phase field to a higher temperature and broadening to a higher carbon concentration due to the presence of a magnetic field, as shown in Figure 5.13. The applied magnetic field of 1.6 T may have shifted the austenite forming temperature by around 3 °C or even more (due to the presence of substitutional alloying elements) to a higher temperature, which could have resulted in the delay of austenite reverse transformation in VSM during partitioning temperature at 600 °C. Moreover, the presence of 1.6 T magnetic field could have resulted in an accelerated and denser carbide precipitation, and spheroidisation of carbides [51] in VSM specimens, when compared to the dilatometer specimens, at the partitioning temperature of 600 °C.

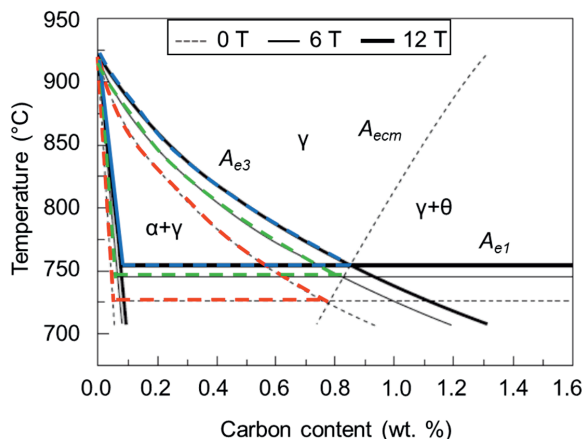


Figure 5.13. Effect of magnetic field on the Fe-C phase diagram based on theoretical calculations, adopted from [34] and slightly modified. The region inside the red, green and blue dashed lines shows the $\alpha+\gamma$ phase field under the influence of 0 T, 6 T and 12 T magnetic field intensities.

4. Retained Austenite in the Final Q&P Microstructures

The retained austenite volume fractions after QP400 and QP500 heat treatments that were determined from room temperature VSM measurements (Figure 5.9) and X-ray diffraction measurements (Figure 5.12) on dilatometry specimens show the same trend with the isothermal holding time. A maximum discrepancy of only ± 0.02 volume fraction of retained austenite is observed between the two techniques, which can be attributed to surface versus bulk detection. In the case of the X-ray diffraction technique, the penetration depth is limited to approximately 10 μm , while in the case of the VSM measurements, the retained austenite volume fraction in the entire bulk sample is measured. After the QP600 heat treatments in the VSM (Figure 5.9c) and dilatometer (Figure 5.12c), the retained austenite volume fractions show a decreasing and increasing trend (opposite trends) with partitioning time, respectively. This difference is due to the austenite reversion observed from dilatometry but not from VSM during partitioning at 600 °C.

In summary, the differences in phase transformation temperatures observed between the VSM and the dilatometry measurements during the applied Q&P thermal cycles can be attributed to the larger surface-area-to-volume ratio of the VSM samples that favours the earlier initiation of phase transformations. The presence of a 1.6 T magnetic field in the VSM, and the differences in sample set-up, can be considered as additional factors contributing to the differences. In-situ magnetic measurements allow to decouple the evolution of austenite from the other competitive reactions occurring during the partitioning stage and, thus, to exert control in the final Q&P microstructure more easily. Based on the current studies, it can be interpreted that the in-situ VSM technique can be a more effective (bulk measurement) and a time-saving technique for precise tracking of the evolution of austenite during a heat treatment.

5.5. Conclusions

A 0.19C-6.0Mn-2Ni (wt.%) steel (alloy *MnNi* from Chapter 3) is subjected to Q&P thermal cycles with partitioning temperatures of 400 °C, 500 °C, and 600 °C for times up to 1800 s. The evolution of the austenite volume fraction during the Q&P process is analysed using in-situ magnetisation (VSM), dilatometry and X-Ray diffraction techniques. Following are the main conclusions.

- The large surface-area-to-volume ratio of the VSM specimen compared to that of the dilatometry specimen favours an early initiation of phase transformations in the VSM specimen. This explains the early phase transformations observed from the VSM experiments.
- Apart from the dimensions of the specimen, the shift in pearlite nose temperature due to the presence of 1.6 T magnetic field and carbide precipitation along the martensite/prior austenite grain boundaries could have resulted in pearlite formation in the VSM specimen but not in the dilatometry specimen.

- Evolution of austenite volume fraction during the partitioning stage can be exclusively tracked despite multiple phenomena such as carbon partitioning and carbide precipitation occurring at the same time. This is evident from the decrease in austenite volume fraction during the initial stage of partitioning at 400 °C, and 600 °C which can be due to austenite decomposition.
- A maximum discrepancy of ± 0.02 volume fraction of retained austenite is observed between the VSM and the XRD specimens after QP400 and QP500 heat treatments. This difference is mainly due to the X-ray diffraction technique probing only a depth of a few micrometres, whereas magnetic measurements probe the entire specimen.

The results from this chapter provide insight into an in-situ magnetisation technique to accurately quantify the evolution of austenite volume fraction irrespective of the multiple reactions occurring simultaneously during the heat treatment, which helps in precisely controlling Q&P microstructures. This study opens up the scope for new studies to understand the influence of magnetic field on the phase transformations in multi-alloyed steel, the behaviour of substitutional alloying elements, and the precipitation of carbides.

References

- [1]. D.K. Matlock, J.G. Speer, **Third generation of AHSS: microstructure design concepts**, Microstructure and Texture in Steels, Springer London, (2009), pp. 185-205.
- [2]. F. Rizzo, A.R. Martins, J.G. Speer, D.K. Matlock, A. Clarke, B.C. De Cooman, **Quenching and partitioning of Ni-added high strength steels**, Materials Science Forum, (2007), pp. 4476-4481.
- [3]. D.T. Pierce, D.R. Coughlin, K.D. Clarke, E. De Moor, J. Poplawsky, D.L. Williamson, B. Mazumder, J.G. Speer, A. Hood, A.J. Clarke, **Microstructural evolution during quenching and partitioning of 0.2C-1.5Mn-1.3Si steels with Cr or Ni additions**, Acta Materialia, 151 (2018), pp. 454-469.
- [4]. X.P. Ma, L.J. Wang, C.M. Liu, S.V. Subramanian, **Role of Nb in low interstitial 13Cr super martensitic stainless steel**, Mater. Sci. Eng. A, 528 (22-23) (2011), pp. 6812-6218.
- [5]. R.W.K. Honeycombe, HKDH Bhadeshia, **Steels: Microstructure and Properties**, 3rd ed., Elsevier Ltd., Amsterdam, (2006), pp. 95-128.
- [6]. T.A. Kop, **A dilatometric study of the austenite/ferrite interface mobility**, Ph.D. Thesis, Delft University of Technology, Delft, The Netherlands (2000).
- [7]. T.D. Bigg, D.V. Edmonds, E.S. Eardley, **Real-time structural analysis of quenching and partitioning (Q&P) in an experimental martensitic steel**, Journal of Alloys and Compounds, 577 (2013), pp. S695-S698.
- [8]. D. De Knijf, M.J. Santofimia, H. Shi, V. Bliznuk, C. Föjer, R. Petrov, W. Xu, **In situ austenite-martensite interface mobility study during annealing**, Acta Materialia, 90 (2015), pp. 161-168.

- [9]. S.Y.P. Allain, G. Geandier, J.C. Hell, M. Soler, F. Danoix, M. Gouné, **Effects of Q&P processing conditions on austenite carbon enrichment studied by in situ high-energy X-ray diffraction experiments**, *Metals*, 7 (2017), pp. 232-244.
- [10]. S. Zhang, H. Terasaki, Y.I. Komizo, **In-situ observation of martensite transformation and retained austenite in supermartensitic steel**, Proceedings of the Twentieth (2010) International Offshore and Polar Engineering Conference. Beijing, China: The International Society of Offshore and Polar Engineers (ISOPE), 20-25 June 2010, pp. 308-311.
- [11]. S.Y.P. Allain, G. Geandier, J.C. Hell, M. Soler, F. Danoix, M. Gouné, **In-situ investigation of quenching and partitioning by High Energy X-Ray Diffraction experiments**, *Scripta Materialia*, 131 (2017), pp. 15-18.
- [12]. L. Zhao, N.H. van Dijk, E. Bruck, J. Sietsma, S. van der Zwaag, **Magnetic and X-ray diffraction measurements for the determination of retained austenite in TRIP steels**, *Materials Science & Engineering A313* (2001), pp. 145-152.
- [13]. K.H. Lo, J.K.L. Lai, C.H. Shek, D.J. Li, **Magnetic and transformation behavior of duplex stainless steels under non-isothermal conditions and temperature-fluctuation monitoring**, *Mater. Sci. Eng. A*, 452-453 (2007), pp. 149-160.
- [14]. A.M. Beese, D. Mohr, **Identification of the direction-dependency of the martensitic transformation in stainless steel using in situ magnetic permeability measurements**, *Exp. Mech.*, vol. 51 (5) (2011), pp. 667-676.
- [15]. G.F. da Silva, S.S.M. Tavares, J.M. Pardal, M.R. Silva, H.F.G. Abreu, **Influence of heat treatments on toughness and sensitization of Ti-alloyed supermartensitic stainless steel**, *J. Mater. Sci.*, 46 (24) (2011), pp. 7737-7744.
- [16]. K. Mumtaz, S. Takahashi, J. Echigoya, Y. Kamada, L.F. Zhang, H. Kikuchi, K. Ara and M. Sato, **Magnetic measurements of the reverse martensite to austenite transformation in a rolled austenitic stainless steel**, *J. Mater. Sci.*, 39 (6) (2004), pp. 1997-2010.
- [17]. S.S.M. Tavares, J.M. Pardal, J.A. de Souza, J.M. Neto and M.R. da Silva, **Magnetic phase quantification of the UNS S32750 superduplex stainless steel**, *J. Alloys Compd.*, 416 (1-2) (2006), pp. 179-182.
- [18]. S.S.M. Tavares, R.F. de Noronha, M. R. da Silva, J.M. Neto and S. Pairis, **475°C embrittlement in a duplex stainless steel UNS S31803**, *Mater. Res.*, 4 (4) (2001), pp. 237-240.
- [19]. N. Luzginova, L. Zhao, J. Sietsma, **Evolution and thermal stability of retained austenite in SAE 52100 bainitic steel**, *Mater. Sci. Eng. A*, 448, (1-2) (2007), pp. 104-110.
- [20]. S.S.M. Tavares, S.R. Mello, A.M. Gomes, J.M. Neto, M.R. da Silva and J. M. Pardal, **X-ray diffraction and magnetic characterization of the retained austenite in a chromium alloyed high carbon steel**, *J. Mater. Sci.*, 41 (15) (2006), pp. 4732-4736.
- [21]. M. Amirthalingam, M.J.M. Hermans, L. Zhao, I.M. Richardson, **Quantitative analysis of microstructural constituents in welded transformation-induced-plasticity steels**, *Metall. Mater. Trans. A*, 41A (2) (2010), pp. 431-439.
- [22]. D. San Martin, N.H. van Dijk, E. Jiménez-Melero, E. Kampert, U. Zeitler, S. van der Zwaag, **Real-time martensitic transformation kinetics in maraging steel under high magnetic fields**, *Mater. Sci. Eng. A*, 527 (20) (2010), pp. 5241-5245.

- [23]. A. Bojack, L. Zhao, P.F. Morris, J. Sietsma: **In-Situ Determination of Austenite and Martensite Formation in 13Cr6Ni2Mo Supermartensitic Stainless Steel**, *Materials Characterization*, 71 (2012), pp.77-86.
- [24]. I.R. Souza Filho, A. Kwiatkowski da Silva, M.J.R. Sandim, **Martensite to austenite reversion in a high-Mn steel: Partitioning-dependent two-stage kinetics revealed by atom probe tomography, in-situ magnetic measurements and simulation**, *Acta Materialia*, 166 (2019), pp.178.
- [25]. P. Dastur, A. Zarei-Hanzaki, R. Rahimi, V. Klemm, B. C. De Cooman, J. Mola, **Nanoscale partitioning of Mn between austenite and martensite revealed by Curie temperature variations**, *Philosophical Magazine letters*, 98 (2) (2018), pp. 55-63.
- [26]. D.C. Jiles, **Recent advances and future directions in magnetic materials**, *Acta Materialia*, 51 (2003), pp. 5907–5939.
- [27]. P.E. Merinov, A.G. Mazepa, **Quantitative analysis of deformation martensite in austenitic steels by a magnetic method**, *Ind Lab (Diagn Mater)*, 63 (3) (1997), pp. 24-28.
- [28]. A. Bojack, L. Zhao, P.F. Morris, J. Sietsma: **In Situ Thermo-Magnetic Investigation of the Austenitic Phase During Tempering of a 13Cr6Ni2Mo Supermartensitic Stainless Steel**, *Metallurgical and Materials Transactions A*, 45A (2014), pp. 5956-5967.
- [29]. A. Bojack, L. Zhao, P.F. Morris, J. Sietsma, **Austenite Formation from Martensite in a 13Cr6Ni2Mo Supermartensitic Stainless Steel**, *Metallurgical and Materials Transactions A*, 47A (2016), pp. 1996-2009.
- [30]. AS Arrott, B. Heinrich, **Application of magnetization measurements in iron to high temperature thermometry**, *J. Appl. Phys.*, 52 (3) (1981), pp. 2113-2115.
- [31]. M. Shimotomai, K. Maruta, K. Mine, M. Matsui, **Formation of aligned two phase microstructures by applying a magnetic field during the austenite to ferrite transformation in steels**, *Acta Materialia*, 51 (10) (2003), pp. 2921-2932.
- [32]. S.J. Wang, X. Zhao, Y.D. Zhang, L. Zuo, C. Esling, **Effect of a high magnetic field on the formation of Widmanstätten ferrite in Fe-0.52C**, *Materials Transactions*, 48 (2007) pp. 2816-2820.
- [33]. T. Garcin, S. Rivoirard, C. Elgoyhen, E. Beaugnon, **Experimental evidence and thermodynamics analysis of high magnetic field effects on the austenite to ferrite transformation temperature in Fe-C-Mn alloys**, *Acta Materialia*, 58 (2010), pp. 2026-2032.
- [34]. Y. Zhang, C. Esling, **Phase Transformations in Steels**, Chapter 16, 1 (2012), pp. 555-580.
- [35]. C.F. Jaczak, **Retained Austenite and Its Measurement by X-Ray Diffraction**, SAE International (1980).
- [36]. D.J. Dyson, B. Holmes, **Effect of alloying additions on the lattice parameter of austenite**. *J. Iron Steel Inst.*, 208, (1970), pp. 469-474.
- [37]. N. van Dijk, A. Butt, L. Zhao, J. Sietsma, S. Offerman, J. Wright, S. van der Zwaag, **Thermal stability of retained austenite in TRIP steels studied by synchrotron X-ray diffraction during cooling**, *Acta Materialia*, 53(20), (2005), pp. 5439-5447.
- [38]. R.M. Bozorth, **Ferromagnetism**, John Wiley & Sons, Inc., Hoboken, NJ, (2003), pp. 715-719.

- [39]. A.W. El-Morsy, A. I. Z. Farahat, **Effect of Cr and Thermomechanical Processing on the Microstructure and Mechanical Properties of Advanced High Strength Steel**, Journal of Engineering Materials and Technology, 140 (2) (2017), pp. 021005.
- [40]. M.Hunkel, H. Surm, M.Steinbacher, **Handbook of Thermal Analysis and Calorimetry**, Elsevier Science B.V, 6 (2018), pp. 103-129.
- [41]. M.J. Santofimia, L. Zhao, J. Sietsma, **Volume Change Associated to Carbon Partitioning from Martensite to Austenite**, Materials Science Forum, 706-709, (2012), pp. 2290-2295.
- [42]. Y. Toji, H. Matsuda, M. Herbig, P.P. Choi, D. Raabe, **Atomic-scale analysis of carbon partitioning between martensite and austenite by atom probe tomography and correlative transmission electron microscopy**, Acta Materialia, 65 (2014), pp. 215-228.
- [43]. X.J. Liu, Y.M. Fang, C.P. Wang, Y.Q. Ma, D.L. Peng, **Effect of external magnetic field on thermodynamic properties and phase transitions in Fe-based alloys**, Journal of Alloys and Compounds, 459 (1-2) (2008), pp. 169-173.
- [44]. A.P. Baur, C. Cayron, R.E. Logé. **Variant selection in surface martensite**, Journal of Applied Crystallography, 50 (2017), pp. 1646-1652.
- [45]. J. Pak, D.W. Suh, H.K.D.H. Bhadeshia, **Displacive phase transformation and surface effects associated with confocal laser scanning microscopy**, Metallurgical and Materials Transactions A, 43 (2012), pp. 4520-4524.
- [46]. A. Navarro Lopez, **Isothermal phase transformations below the martensitic start temperature in a low-carbon steel**, Ph.D. Thesis, Delft University of Technology, Delft, The Netherlands (2020).
- [47]. K.R. Satyanaryan, W. Elias, A.P. Miodownik, **The effect of a magnetic field on the martensite transformation in steels**, Acta Metallurgica, 16 (1968), pp. 877-887.
- [48]. M.A. Krivoglaz, V.D. Sadovsky, **Effect of strong magnetic fields on phase transitions**, Physics of Metals and Metallography, 18 (1964), pp. 502.
- [49]. T.P. Hou, K.M. Wu, **Alloy carbide precipitation in tempered 2.25 Cr-Mo steel under high magnetic field**. Acta Materialia, 61 (2013), pp. 2016–2024.
- [50]. T.P. Hou, Y. Li, J.J. Zhang, K.M. Wu, **Effect of magnetic field on the carbide precipitation during tempering of a molybdenum-containing steel**, Journal of Magnetism and Magnetic Materials, 324 (2012), pp. 857–861.
- [51]. Zihua Li, Tingping Hou, Guanghui Wu, Kaiming Wu and Hengfu Lin, **Thermodynamic Analysis for the Magnetic-Field-Induced Precipitation Behaviours in Steels**, Metals, 9 (8) (2019), pp.909.
- [52]. A. Borgenstam, L. Hoglund, J. Agren, A. Engstrom, **DICTRA, a tool for simulation of diffusional transformations in alloys**, Journal of Phase Equilibria, 21 (2000), pp. 269.

6

Key Conclusions and Recommendations

6.1. Key Conclusions

The main objective of this Ph.D. thesis is to study the microstructure evolution during the new high-temperature quenching and partitioning (Q&P) process. Five different low carbon medium manganese steels with varying silicon and nickel contents are analysed to understand the impact of substitutional alloying elements on microstructural evolution during the Q&P process and on the final microstructure. The current research has led to the fundamental understanding of the microstructural evolution during high-temperature Q&P processes, mechanisms related to interface movement and partitioning of substitutional alloying element (manganese) during the partitioning stage. The key conclusions from individual chapters of this Ph.D. thesis are summarised as follows.

- Besides acceleration of carbon partitioning, increasing partitioning temperature stimulates competitive reactions that reduce the stability of austenite at room temperature. Minor competitive phenomena, such as carbide precipitation inside martensite, reduce carbon available for partitioning, while the major competitive phenomena, such as carbide precipitation inside austenite and pearlite formation, reduce the carbon available for partitioning as well as the available austenite fraction. Such reactions derail the purpose of high temperature Q&P process, which is to retain higher volume fractions of austenite in the final microstructure through partitioning of substitutional alloying elements. Major competitive reactions, such as carbide precipitation in austenite and pearlite formation, are fast and simultaneous phenomena that are dominant in the early and later stages of the high temperature partitioning stage (higher than 450 °C). Although it is not possible to completely suppress the competitive reactions, the key for an effective Q&P process is to minimise such reactions which is possible by selecting shorter partitioning times at higher partitioning temperatures (Chapter 2).
- Irrespective of the partitioning temperature, a significant fraction of carbon is not partitioned into austenite but remains in primary martensite, either in solid solution or in form of carbides. This carbide precipitation during partitioning at lower temperatures (400 °C) can be hindered by the addition of silicon. However, the presence of silicon can accelerate the competitive reactions during partitioning at higher temperatures (above 400 °C - below A_{c1}). It is the combination of partitioning conditions and alloying elements that controls the occurrence of competitive phenomena during the partitioning stage (Chapter 3).
- Partitioning temperatures above and below the nose of pearlite in TTT diagrams are more beneficial to avoid competitive reactions than partitioning at temperatures close to the nose of the pearlite of the respective alloys. Accelerated kinetics of carbon partitioning with increasing partitioning temperatures along with the martensite/austenite interfaces, which are potential nucleation sites for the initiation of pearlite formation, accelerates pearlite formation during partitioning at temperatures close to the nose of pearlite. Pearlite formation can be delayed by the addition of nickel. Nickel also

promotes austenite reverse transformation, a major competitive phenomenon, during partitioning stage, which is beneficial for austenite stabilisation. During the final quench the reverted austenite is more stable than the pre-existing austenite (Chapter 3).

- The reason behind higher stability of reverted austenite at room temperature compared to the pre-existing austenite is manganese enrichment in the reverted austenite. Observations from experiments and simulations show that interface migration and manganese partitioning are simultaneous phenomena. During the α'/γ interface migration, not all manganese moves with the interface which could be due to migration of the interface being effectively faster than the manganese diffusion. Hence, the reverted austenite is enriched with higher manganese concentration. Therefore, highly advantageous partitioning conditions for an alloy to stabilise higher volume fractions of retained austenite are those at which local partitioning of substitutional elements and martensite/austenite interface migration are both feasible (Chapter 4).
- Observations from chapter 5 indicate that the free surface of the specimen favours the initiation of phase transformations. Due to large surface-area-to-volume ratio of the VSM specimen compared to that of the dilatometry specimen, early phase transformations are detected in the VSM specimen. The phase transformations in a bulk specimen can be effectively tracked using the in-situ magnetisation (VSM) technique, which can avoid underestimation of microstructural events during a thermal process (Chapter 5).

6.2. Recommendations for Future Work

From this thesis a wider understanding regarding the microstructural evolution and mechanisms involved in high-temperature Q&P process has been gained. However, it simultaneously opened up new challenges and new line of investigations. Following are recommendations for further research.

- In Chapter 4, phase-field modelling has been effectively used to study partitioning stage during Q&P process neglecting any competitive reactions. However, carbides consume a significant fraction of carbon during the partitioning stage (Chapter 2, 3 and 4). If the nature of the carbides precipitated during the partitioning stage can be characterised by high resolution transmission electron microscopy (HR-TEM) observations and the same can be introduced during the simulation of partitioning stage, quantitative estimation of carbon partitioned into austenite and carbon consumed by carbides will be possible without further rigorous experimental work.
- It is indicated that the free surface of the steel favours easy phase transformations (Chapter 5). The major application of Q&P steels is safety-related components in automobiles, like B-pillars. The paramount requirement for this is the production of metal sheets (thickness of 2 mm – 4 mm) with a uniform multi-phase microstructure along the thickness of the steel. Considering the rapid change in

the temperatures involved in the Q&P process, it could be industrially challenging to produce a uniform microstructure along the thickness of the steel. Hence, it is highly recommended to study microstructure evolution during Q&P process at different thickness levels of the steel.

- The cooling system of the in-situ magnetisation technique can be improved to get a homogeneous cooling rate during the experiments. This would further reduce the experimental time. This also avoids performing further room-temperature magnetisation experiments on the heat-treated specimens. As a continuation to the work in Chapter 5, the investigation of a similar alloy with silicon via in-situ magnetisation technique can help to study the impact of magnetisation on carbide precipitation. Since in-situ magnetisation technique is effective in tracking austenite volume fraction during the Q&P process, the impact of carbides on austenite decomposition or martensite/austenite interface migration during the partitioning stage can also be studied.
- Although the final Q&P microstructures of some studied alloys (especially alloys with nickel) retain a significant fraction of austenite, the thermal and mechanical stability of these heat-treated alloys should be studied. This further investigation will help to determine the effectiveness of high-temperature Q&P heat treatments on medium manganese steels when compared to the Q&P steels produced with typical partitioning temperatures.

Summary

An effective way for the automotive industry to tackle the growing concern of CO₂ emissions from automobiles is to reduce the overall weight of the vehicle, without compromising its performance and passenger safety. With the increasing demand of steels with enhanced properties in the last decade, the development of advanced high strength steels (AHSSs) has been focused on the design of complex microstructures leading to exceptional combinations of strength and ductility. One such steel is Quenching and Partitioning (Q&P) steel, which is typically composed of a high strength phase, martensite, and a softer phase, austenite, which contributes to the ductility of the material. The main strategy in developing Q&P steels involves partitioning of carbon, an interstitial alloying element, from supersaturated martensite (α^l , formed in an initial quenching step from the austenitisation temperature) into austenite (γ) during an isothermal holding (partitioning stage) to enhance the thermal and mechanical stability of austenite. If the partitioning step is subjected at higher temperatures, substitutional austenite-stabilising alloying elements, such as manganese, may partition to the austenite and significantly enhance the stability of austenite in the final microstructure. Keeping this in mind, experimental and modelling approaches are employed in this Ph.D. thesis to investigate the microstructural evolution and the mechanisms involved during the quenching and high-temperature partitioning process in five different medium manganese steels.

In a typical quenching and partitioning process, the isothermal holding temperatures (partitioning temperatures) are in the range of 350 to 450 °C, where carbon partitioning is significant and plays a key role in stabilising austenite. In order to stimulate the partitioning of substitutional alloying elements, such as manganese, from martensite to austenite, higher partitioning temperatures (500 °C – below A_{c1} of respective steel) are employed in this thesis. Chapter 2 gives insight into the microstructural evolution and competitive reactions occurring in a medium manganese steel during high-temperature partitioning in the Q&P process. With the increase in partitioning temperatures, the kinetics of carbon partitioning from martensite to austenite is enhanced due to which additional competitive phenomena are observed. In particular, partitioning of carbon at 400 °C leads to austenite stabilisation during the final quench, while carbon partitioning at 450 °C leads to carbide precipitation inside austenite grains. At even higher partitioning temperatures (500 – 600 °C), carbon partitioning stimulates pearlite formation. Competitive phenomena such as carbide precipitation in austenite and pearlite formation have a negative influence on the austenite stability and on the Q&P microstructural development, as they reduce the carbon available for partitioning during the partitioning stage and decrease the volume fraction of austenite. In the last part of this chapter, the extent in which microstructural processes hinder or inhibit the partitioning of alloying elements during the Q&P heat treatment is quantitatively assessed. Based on theoretical calculations, it is concluded that at the end of isothermal holding at partitioning temperatures of 400 °C to 600 °C, almost no carbon is available in the solid solution of primary martensite, indicating

Summary

that neighbouring austenite grains are highly enriched in carbon. This significant enrichment of carbon in austenite grains results in carbide precipitation and pearlite formation in austenite films and austenite grains, respectively. The observations show that the suppression of the competitive reactions at high partitioning temperatures is necessary to optimise the austenite stabilising effect of carbon and manganese in a Q&P steel.

In chapter 3, based on the observations from chapter 2, controlled partitioning conditions are applied on four low-carbon medium-manganese steels with varying nickel and silicon contents. The impact of the substitutional alloying elements, nickel and silicon, on the microstructure development is studied. It is observed that during partitioning at 400 °C, silicon hinders cementite precipitation in primary martensite thereby assisting carbon partitioning from martensite to austenite. However, the presence of silicon at partitioning temperatures of 500 and 600 °C hinders carbide precipitation in primary martensite resulting in significant carbon enrichment in austenite films and grains where, consequently, carbide precipitation and pearlite formation occurs. During partitioning at temperatures of 500 and 600 °C, the presence of nickel inhibits pearlite formation and promotes austenite reversion (transformation of primary martensite into austenite). Interestingly, the austenite reverted during the partitioning stage is more stable during the final quench than the pre-existing austenite. The addition of nickel and adjustments of the Q&P cycles to promote the formation of reverted austenite are therefore both potential strategies to stabilise higher fractions of retained austenite in the final microstructure.

In chapter 4, the mechanism behind the higher stability of reverted austenite, relative to pre-existing austenite is investigated by combining multi-phase field modelling and 3D atom probe tomography experiments. Results from experiments and simulations show that the reverted austenite is enriched with a higher concentration of manganese compared to the pre-existing austenite. It was also observed that the martensite/austenite (α'/γ) interface migration and manganese partitioning proceed simultaneously. However, the migration of the interface seems to be effectively faster than the manganese diffusion. Hence, the reverted austenite is enriched with manganese. Therefore, the most advantageous partitioning conditions for an alloy to stabilise higher volume fractions of austenite are those at which local partitioning of substitutional elements and martensite/austenite interface migration are feasible.

The investigations from Chapter 2 and 3 also show that the volume fraction of austenite present in the material after the initial quench strongly influences the competitive reactions occurring during the partitioning stage of the Q&P process. In this regard, the effective and precise tracking of the austenite volume fraction during the Q&P process is very important to optimise the thermal cycles. Chapter 5 explores the microstructural evolution during Q&P process in medium manganese steels using an in-situ magnetisation technique. This is complemented by dilatometry and X-ray diffraction measurements. It is observed that the large surface area-to-volume ratio of the VSM (vibrating sample magnetometry) specimen compared to that of the dilatometry specimen, favours early phase transformations in the VSM specimen. The outcome of this chapter shows that the in-situ magnetic measurements allow to decouple

the evolution of austenite from the other competitive reactions that take place during the partitioning stage. The in-situ magnetisation technique can therefore be an effective and time-efficient technique for the precise tracking of the evolution of austenite during a heat treatment, probing the bulk of the sample.

The outcomes of this Ph.D. research highlight the importance of suppressing competitive reactions during the partitioning stage of the Q&P process and developing methods to achieve this. The fundamental knowledge gained from this research about the mechanisms related to partitioning of substitutional alloying elements and the α/γ interface migration during the partitioning stage opens up the possibility of further exploiting the functionality of substitutional alloying elements to enhance the properties of the Q&P steels. The last chapter of the thesis discusses the findings of the research and presents suggestions for further research.

Samenvatting

Een effectieve manier voor de auto-industrie om de CO₂-uitstoot van auto's te reduceren, is het totale gewicht van het voertuig te verminderen zonder de prestaties ervan en de veiligheid van de passagiers in gevaar te brengen. Met de toenemende vraag naar staal met verbeterde eigenschappen is de ontwikkeling van geavanceerde hogesterkte-stalen (AHSS's) de afgelopen tien jaar gericht geweest op het ontwerp van complexe microstructuren die tot een uitzonderlijke combinatie van twee gewenste eigenschappen, sterkte en taaheid, leiden. Een voorbeeld van deze staalsoorten is Quenching & Partitioning staal (Q&P-staal) dat typisch is samengesteld uit een fase met hoge sterkte, martensiet, en een zachtere fase, austeniet, die bijdraagt aan de taaheid van het materiaal. De belangrijkste strategie bij de ontwikkeling van Q&P-staalsoorten behelst het herverdelen (partitionering) van koolstof, een interstitieel legeringselement, van oververzadigd martensiet (α' , gevormd in een initiële afschrikingsstap vanaf een austenitiserings temperatuur) naar austeniet (γ) tijdens het isotherme gloeien (partitioneringsfase) om de thermische en mechanische stabiliteit van austeniet te verbeteren. Aan de andere kant kunnen ook substitusionele legeringselementen, zoals mangaan, de stabiliteit van austeniet in de uiteindelijke microstructuur aanzienlijk verbeteren, omdat het sterke austeniet-stabiliserende elementen zijn. Daarom kan de verwerking van medium-mangaanstaal door middel van een Q&P thermische cyclus tot een nog betere combinatie van sterkte en ductiliteit leiden. Met dit in gedachten worden in dit proefschrift experimentele en modelleringsbenaderingen gebruikt om de microstructurele evolutie en de mechanismen die betrokken zijn bij het afschrikken en het partitioneringsproces bij hoge temperatuur in medium mangaanstaal te onderzoeken.

In een typisch afschrik- en partitioneringsproces liggen de isotherme gloeitemperaturen (partitioneringstemperaturen) in het bereik van 350°C tot 450°C, waarbij koolstofpartitionering significant is en een sleutelrol speelt bij het stabiliseren van austeniet. Om de scheiding van substitusionele legeringselementen, zoals mangaan, van martensiet naar austeniet te stimuleren, worden in dit proefschrift hogere scheidingstemperaturen (500°C – lager dan A_{c1} van het staal) gebruikt. Hoofdstuk 2 is erop gericht inzicht te geven in de microstructurele evolutie en competitieve reacties die optreden in een medium-mangaanstaal tijdens hogetemperatuurpartitionering in het Q&P proces. Met de toename van de partitioneringstemperaturen wordt de koolstofpartitionering van martensiet naar austeniet versneld, waarbij ook additionele competitieve verschijnselen worden waargenomen. De belangrijkste microstructurele processen als gevolg van koolstofpartitionering zijn dat de herverdeling van koolstof bij 400°C leidt tot austeniet-stabilisatie tijdens de laatste afschikking, terwijl koolstofpartitionering bij 450 ° C leidt tot carbideprecipitatie in austenietkorrels. Bij nog hogere partitioneringstemperaturen (500 – 600°C) stimuleert de koolstofherverdeling ook de vorming van perliet. Concurrerende verschijnselen, zoals carbideprecipitatie in austeniet en perlietvorming hebben een negatieve invloed op de austenietstabiliteit, omdat ze de koolstof die beschikbaar is voor

Samenvatting

partitionering tijdens de partitioneringsfase verminderen. In het laatste deel van dit hoofdstuk wordt een kwantitatieve beoordeling uitgevoerd om de mate te evalueren, waarin microstructurele processen de herverdeling van legeringselementen tijdens de Q&P-warmtebehandeling belemmeren of afremmen. Op basis van theoretische berekeningen wordt geconcludeerd dat aan het einde van isotherme tempering bij partitioneringstemperaturen van 400 ° C - 600°C bijna geen koolstof beschikbaar is in de vaste oplossing van primair martensiet, hetgeen aangeeft dat naburige austenietkorrels sterk verrijkt zijn in koolstof. Deze significante verrijking van koolstof in austenietkorrels resulteert in carbideprecipitatie en perlietvorming in respectievelijk austenietfilms en austenietkorrels. De waarnemingen tonen aan dat het tegengaan van de competitieve reacties bij hoge partitioneringstemperaturen noodzakelijk is om het austeniet-stabiliserende effect van koolstof en mangaan in een Q&P-staal te optimaliseren.

In hoofdstuk 3 worden, op basis van de waarnemingen uit hoofdstuk 2, gecontroleerde partitioneringscondities toegepast op vier koolstofarme medium-mangaanstaalsoorten met variërende nikkel- en siliciumgehalten. De impact van de substitutionele legeringselementen, nikkel en silicium, op de ontwikkeling van de microstructuur wordt in dit hoofdstuk beschreven. Er wordt waargenomen dat silicium tijdens partitionering bij 400°C de precipitatie van cementiet in primair martensiet belemmert, waardoor de koolstofherverdeling van martensiet naar austeniet wordt bevordert. De aanwezigheid van silicium bij partitioneringstemperaturen van 500°C en 600°C belemmert echter carbideprecipitatie in primair martensiet, hetgeen resulteert in een significante koolstofverrijking van austenietfilms en -korrels. Dit resulteert in carbideprecipitatie en perlietvorming in respectievelijk austenietfilms en austenietkorrels. Tijdens het partitioneren bij temperaturen van 500°C en 600 °C remt de aanwezigheid van nikkel de vorming van perliet en bevordert het de austeniet-reversie (transformatie van primair martensiet naar austeniet). Interessant is dat het austeniet dat tijdens deze fase wordt gevormd stabiel is tijdens de laatste afschrikstap dan het reeds bestaande austeniet. Het maakt duidelijk dat de toevoeging van nikkel en de aanpassingen van de Q&P-cycli om het ontstaan van opnieuw gevormd austeniet te bevorderen, beiden mogelijke strategieën zijn om hogere fracties austeniet in de uiteindelijke microstructuur te stabiliseren.

In hoofdstuk 4 het mechanisme achter de hogere stabiliteit van opnieuw gevormd austeniet bestudeerd en deze fase vergeleken met reeds bestaand austeniet, door Multi-Phase-field modellering en 3D Atom Probe Tomography experimenten te combineren. De resultaten van experimenten en simulaties laten zien dat het opnieuw gevormde austeniet is verrijkt met een hogere concentratie mangaan in vergelijking met het reeds bestaande austeniet. Er wordt ook waargenomen dat de martensiet/austeniet (α/γ) grensvlakmigratie en mangaanpartitionering gelijktijdig plaatsvinden. Maar de interfacemigratie lijkt echter effectief sneller te zijn dan de mangaandiffusie. Daarom is het opnieuw gevormde austeniet verrijkt tot een hogere mangaanconcentratie. Daarom zijn gunstige partitioneringsvoorwaarden voor een legering om hogere volumefracties restausteniet te stabiliseren, die waarbij lokale partitionering van substitutionele elementen en martensiet/austeniet-grensvlakmigratie mogelijk zijn.

Het onderzoek uit hoofdstuk 2 en 3 laat ook zien dat de volumefractie van austeniet die aanwezig is in het materiaal na het initiële afschrikken een sterke invloed heeft op de competitieve reacties die optreden tijdens de partitioneringsfase van het Q&P-proces. In dit opzicht is het nauwkeurig volgen van de austeniet-volumefractie tijdens het Q&P-proces erg belangrijk om de thermische cycli te optimaliseren. Hoofdstuk 5 beschrijft de microstructurele evolutie tijdens het Q&P-proces in medium-mangaanstaalsoorten met behulp van een in-situ magnetisatietechniek. Dit wordt aangevuld met dilatometrie en Röntgendiffractiemetingen. Er wordt waargenomen dat de grote oppervlakte-tot-volumeverhouding van het proefstuk voor de experimenten in de Vibrating Sample Magnetometer (VSM) in vergelijking met die van het proefstuk voor dilatometrie, vroegere faseformaties in het VSM-proefstuk veroorzaakt. De uitkomsten van dit hoofdstuk laten zien dat de in-situ magnetische metingen het mogelijk maken om de evolutie van austeniet los te koppelen van de andere competitieve reacties die optreden tijdens de partitioneringsfase. Het is duidelijk dat de in-situ magnetisatietechniek een effectieve en tijdsefficiënte techniek kan zijn voor het nauwkeurig volgen van de evolutie van austeniet tijdens een warmtebehandeling, waarbij deze techniek het gehele volume van het proefstuk onderzoekt

De resultaten van dit promotieonderzoek benadrukken het belang van onderdrukking van competitieve reacties tijdens de partitioneringsfase van het Q&P proces en het ontwikkelen van methodes om dit te bewerkstelligen. De fundamentele kennis die is opgedaan in dit onderzoek aan de mechanismen die verband houden met de herverdeling van substitutionele legeringselementen en de migratie van het α/γ -grensvlak tijdens de partitioneringsfase opent de mogelijkheid om de mogelijkheden van substitutionele legeringselementen verder te benutten om de eigenschappen van de Q&P-staalsoorten te verbeteren. Het laatste hoofdstuk van het proefschrift bespreekt de bevindingen van het onderzoek en geeft suggesties voor verder onderzoek.

Acknowledgements

First of all, I would like to thank Prof.dr. M.J. Santofimia and Prof.dr.ir. J. Sietsma for they have been amazing promoters. The trust, support and freedom they offered me during this journey have let me develop as a confident, independent researcher. I also would like to thank my daily supervisor and co-promoter, Dr. C. Alonso de Celada Casero, for her invaluable professional and personal support during this journey. This thesis would not have been the same without you. I thank all three, for all those wonderful scientific discussions, for being patient in explaining things to me, and especially for providing great support during the Covid times.

I express my gratitude to European Commission and Research Fund for Coal and Steel (RFCS) for funding this project, HighQP (proposal number: 709855). I would like to thank my project partners, Dr. M. Arribas and Dr. T. Gutierrez (Tecnalia, Spain), Dr. A. Arlazarov (Arcelor Mittal, France), Dr. D. Martin (Swerim, Sweden), and D. De Caro (CRF, Italy) for all those discussions during our meetings.

I thank the technical staff in the MSE laboratories, Richard (XRD), Kees (SEM), Sander van Asperen (metallography), for their support. My special thanks to Nico Geerlofs, who had been a great support in performing dilatometer and magnetometer experiments. Special thanks for building the in-situ magnetometer, which has contributed significantly to my thesis. I thank Dr. M. Herbig and Dr. S.B. Nair for performing APT experiments at Max-Planck-Institut für Eisenforschung, Dusseldorf, Germany. I also want to thank Prof. Jan van Turnhout for his help with translating the summary of my Ph.D. thesis into Dutch.

This Ph.D journey would not have been the same without the support of a few incredible people: Chrysa, Wei, Alfonso, Carola and Javier, Viviam, Konstantina, Javier, Zaloo, Evangelos, Tim and Marilia, and Constantinos. You will always be special people in my life. It has been an incredible experience working with colleagues/friends from different parts of the world. I also greatly acknowledge the scientific and fun conversations with Vitoria, Jithin, Naveena, Arthur, Vibhor, and Lee, especially during the lunchtimes, helped me learn many things.

The place I felt and still feel like home is Delft. It is because of my amazing house-mates Avinash (bhai), Dori, Meli, and Asla, whom I cannot thank enough for all their love and affection. Although I have been quite far from my family in India, I seldom felt it that way. It is because of Geetha, Kashyap, Bala, Varun, and Vishwa. Thank you for all the wonderful memories! You guys have been like a real family far from home. One thing that kept me active and motivated outside my Ph.D. is Cricket. It is my pleasure to be a part of Concordia sports club and especially the 2B team.

I would like to thank my friends in Germany: Swarup, Teju, Raghu, Rohith, and especially Avinash, for all those amazing late-night discussions. Special mention to Swarup and Rohith, without whom our start-up would be impossible. Every time in need, you were just a call away. My friends in India: Siva, Murali, Manoj, and Vinay, you guys have filled me with laughter whenever we met, physically or virtually. Thank you, Harsha, and Ravi who has been with me during this journey.

Last but not least, I would like to thank my grandparents, parents, brother, and sister-in-law. There will never be enough words to describe the support I received from you through thick and thin. Thank you for everything! A very special thanks to my uncle, Sreedhar, for being an inspiration in many aspects.

Delft, September 2021

Sudhindra

List of Publications

1. S. Ayenampudi, C. Celada-Casero, N. Geerlofs, J. Sietsma, and M.J. Santofimia: *In-situ Magnetometry and Dilatometry Investigation of Austenite Evolution during Quenching and Partitioning Process in a Medium-Mn Steel*. To be submitted for publication.
2. S. Ayenampudi, C. Celada-Casero, J. Sietsma, and M. J. Santofimia, *3D atom probe tomography and phase-field modelling investigation of interface migration and elemental partitioning during quenching and partitioning process*. To be submitted for publication.
3. M. Arribas, E. D. Molino, T. Gutiérrez, A. Arlazarov, D. Martin, D. De Caro, S. Ayenampudi and M.J. Santofimia: *Characterization of a Medium Mn-Ni Steel Q&P Treated by a High Partitioning Temperature Cycle*, submitted to Materials Science and Engineering: A.
4. M. Arribas, T. Gutiérrez, E. D. Molino, A. Arlazarov, I. De Diego-Calderón, D. Martin, D. De Caro, S. Ayenampudi and M. J. Santofimia: *Austenite Reverse Transformation in a Q&P Route of Mn and Ni Added Steels*, Metals 10 (2020) 862.
5. S. Ayenampudi, C. Celada-Casero, J. Sietsma, and M. J. Santofimia: *Microstructure evolution during high-temperature partitioning of a medium-Mn Quenching and Partitioning steel*, Materialia 8 (2019) 100492.
6. S. Ayenampudi, C. Celada-Casero, Z. Arechabaleta, M. Arribas, A. Arlazarov, J. Sietsma, and M.J. Santofimia: *Microstructural impact of Si and Ni during high temperature quenching and partitioning process in medium-Mn steels*, Metallurgical and Materials Transactions A 52 (2021), pp. 1321 – 1335.

List of Conferences

1. S. Ayenampudi, C. Celada-Casero, J. Sietsma, and M. J. Santofimia: *Effect of nickel on austenite stabilization in medium-Mn steels during quenching and partitioning* – MS&T'19, 28 Sept'19 – 3 Oct '19 – **Oral Presentation**.
2. S. Ayenampudi, C. Celada-Casero, J. Sietsma, and M. J. Santofimia: *Study of partitioning kinetics of alloying elements in a medium Mn steel during Q&P treatments using phase-field modeling* – Thermec'18, 8-13 July'18 – **Poster Presentation**.
3. S. Ayenampudi, C. Celada-Casero, J. Sietsma, and M. J. Santofimia: *Microstructural evolution during high-temperature partitioning of a medium-Mn Q&P steel* – EUROMAT'17, 17-22 Sept'17, Thessaloniki – **Oral Presentation**.

About the Author

Sudhindra AYENAMPUDI

Born on 21st July 1992, in Visakhapatnam, India

Professional Experience

01.2021 – 08.2021	Delft University of Technology Researcher Project: Understanding the microstructural essence of Damage Evolution in Rolling contact fatigue (UNDER)
10.2016 – 10.2020	Delft University of Technology Ph.D. Researcher Project: Microstructural Evolution in Medium Manganese Steels during Quenching and High-Temperature Partitioning Process
10.2015 – 12.2015	Industrial Internship (within Masters) TATA Steel Europe, IJmuiden, The Netherlands
01.2012 – 03.2012	Industrial Internship (within Bachelors) Visakhapatnam Steel Plant, India

Education

10.2016 – 10.2020	Ph.D. in Materials Science and Engineering Delft University of Technology (TU Delft), The Netherlands
10.2013 – 06.2016	Master of Science in Metallurgical Engineering RWTH Aachen University, Aachen, Germany
08.2009 – 05.2013	Bachelor in Mechanical Engineering JNTU Kakinada, India

Languages

Telugu	Native
English	Advanced. Full Professional Proficiency
Hindi	Advanced
German	Intermediate (Goethe-Zertifikat, B1, 2016)
Dutch	Intermediate (currently studying B1 level)



ISBN 978-94-6423-427-5

